

PLASMONIC NANOPARTICLES FOR APPLICATIONS IN LIGHT SCATTERING
SPECTROELECTROCHEMISTRY AND PHOTOELECTROCHEMICAL
WATER SPLITTING

by

YANXIAO MA

SHANLIN PAN, COMMITTEE CHAIR
CAROLYN J. CASSADY
SHANE C. STREET
GREGORY SZULCZEWSKI
SUBHADRA GUPTA

A DISSERTATION

Submitted in partial fulfillment of the requirements
for the degree of Doctor of Philosophy
in the Department of Chemistry and Biochemistry
in the Graduate School of
The University of Alabama

TUSCALOOSA, ALABAMA

2019

Copyright Yanxiao Ma 2019
ALL RIGHTS RESERVED

ABSTRACT

Plasmonic gold nanoparticles (NPs) have interesting properties in both surface plasmon resonance and electrocatalytic reactions. However, the mechanism of local redox events at electrocatalytic Au NPs remains uncertain. This dissertation presents the mechanism study of catalyzed redox reactions at plasmonic nanoparticles by a spectroelectrochemistry methodology. Furthermore, the applications of plasmonic Au NPs are presented for fuel cell based reactions and solar water splitting.

Firstly, planar and ultramicroelectrode (UME) of indium tin oxide (ITO) electrode is modified by Au nanoparticles (NPs) for dark-field scattering spectroelectrochemistry study of hydrazine oxidation. Photolithography, ion milling, plasma etching and sputtering system are utilized for ITO UME fabrication in the clean room. Dark-field scattering (DFS) study of single Au NPs shows light scattering signal decrease in the low overpotential region upon hydrazine oxidation because of the double layer charging and surface adsorbates. Strong light scattering can be obtained due to nitrogen bubble formation on the Au NP surface and bulk solution, which is accompanied by a decrease in oxidation current due to the deactivation of Au NPs. Au anodization is observed at high overpotential without hydrazine, such behavior is limited with the presence of > 50 mM hydrazine.

Secondly, Au coated semi-transparent ITO electrode is further modified by Pt for electrocatalytic and spectroelectrochemistry study of methanol and formic acid oxidation. Scanning electron microscopy (SEM) and high-resolution transmission electron microscopy (HRTEM) results confirm the Au-Pt core-shell structure. Enhanced catalytic activity is found for both methanol and formic acid oxidation with Au@Pt structure with respect to Au-ITO. The oxidation current density is

more than 200 times greater than that on Au-ITO with Au@Pt(30) sample for both methanol and formic acid. Au NPs are anodized at the potential window of methanol oxidation at lower Pt coverage. Au anodization diminishes and is terminated with increasing Pt thicknesses.

Finally, Au-incorporated hematite is screened by scanning photoelectrochemical microscopy (SPECM) to tailor and optimize its electronic properties for solar water oxidation under visible light irradiation. The pristine and Au-incorporated hematite materials are also characterized by SEM techniques. Au is found to exist in the form of embedded nanoparticles in the Au-hematite structures. Au-incorporated hematite exhibits enhancement in photocurrent for Au concentration up to 3% (atomic percent) and the performance drop is observed with 4 – 10% of Au. Subsequently, pristine and Au-incorporated hematite thin film photoanodes are fabricated by spin-coating method with optimal precursor concentrations of Au and $\text{Fe}(\text{NO}_3)_3$ to confirm the results of SPECM. The photoelectrochemical (PEC) response confirms that 3% Au inside hematite film is optimum for efficient water oxidation. Mott-Schottky analysis of the bulk samples confirms an improvement in charge carrier density for Au-incorporated hematite. The generation of oxygen from the substrates was quantitatively measured by surface generation tip collection mode of SECM.

DEDICATION

I would like to dedicate this dissertation to my beloved parents who have supported me throughout the Ph.D. program. Thank you for being the guardian and mentor of my life.

LIST OF ABBREVIATIONS AND SYMBOLS

A	Absorbance
AM	Air mass
b	Optical path length
C	Coulombs
°C	Degree Celsius
C	Capacitance
c	Concentration
CB	Conduction band
CE	Counter electrode
CL	Condenser lens
CV	Cyclic voltammetry
DC	Direct current
DFS	Dark-field scattering
DI	Deionized
e-	Electrons
E	Potential
ECL	Electrogenerated chemiluminescence
EDS	Energy dispersive X-ray spectroscopy

EG	Ethylene glycol
EIS	Electrochemical impedance spectra
EMCCD	Electron multiplying charge-coupled device
eV	Electron volt
FIB	Focused ion beam
FTO	Fluorine-doped tin oxide
g	Gram
h^+	Hole
HAADF	High-angle annular dark-field
HER	Hydrogen Evolution reaction
Hz	Hertz
I	Current
ITO	Indium-doped tin oxide
J	Joules
J-V	Current density vs. voltage
kV	Kilovolt
kW	Kilowatt
LSPR	Localized surface plasmon resonance
m	Meters
M	Molar
mA	Milliampere
MHz	Megahertz
min	Minute

mm	Millimeter
mM	Millimolar
mol	Moles
M-S	Mott-Schottky
mW cm ⁻²	Milliwatts per square centimeter
η	Overpotential
NHE	Normal hydrogen electrode
nm	Nanometer
NP	Nanoparticle
NR	Nanorod
OER	Oxygen evolution reaction
OL	Objective lens
OLED	Organic light emitting diode
Pa	Pascal
PBS	Phosphate buffer solution
PEC	Photoelectrochemical
pH	The acidity or basicity of a solution
pL	Picoliter
PMT	Photomultiplier tube
QRE	Quasi-reference electrode
R _{CT}	Charge transfer resistance
RE	Reference electrode
RHE	Reversible hydrogen electrode

R_s	Series resistance
s	Seconds
SECM	Scanning electrochemical microscope
SEM	Scanning electron microscopy
SERS	Surface-enhanced Raman spectroscopy
SPECM	Scanning photoelectrochemical microscope
SPR	Surface plasmon resonance
STEM	Scanning-transmission electron microscope
TEM	Transmission electron microscopy
TWh	Terawatt hours
UME	Ultramicroelectrode
UV-Vis	Ultraviolet-Visible
V	Volts
V/s	Volts per second
VB	Valence band
vs.	Versus
WE	Working electrode
XPS	X-ray photoelectron spectroscopy
XRD	X-ray diffraction
ϵ	Molar absorption coefficient
μm	Micrometer
Ω	Ohms
$\mu\text{A cm}^{-2}$	Microamperes per centimeter

ACKNOWLEDGEMENTS

I would like to express my utmost gratitude to my research advisor and committee chair, Dr. Shanlin Pan, for his encouragement and support throughout my studies at The University of Alabama. I would also like to thank my dissertation committee members Dr. Carolyn J. Cassady, Dr. Shane C. Street, Dr. Gregory Szulczewski and Dr. Subhadra Gupta for their support and important feedback on my research.

I am grateful to Dr. Alton Highsmith for clean room operation training. I would like to thank Johnny Goodwin, Rob Holler and Rich Martens from Central Analytical Facility for their assistance on SEM and TEM. Thanks to David Key and other technicians from the machine shop for helping with the electrochemical cell fabrication.

I take this opportunity to express my sincere appreciation to current and previous group members, Dr. Caleb Hill, Dr. Daniel Clayton, Dr. Jue Wang, Dr. Zhichao Shan, Jia Liu, Dr. Yiliyasi Wusimanjiang, Dr. Pravin Shinde, Dr. Nelly Kaneza, Lyndi Strange, Jeetika Yadav and Xiao Li for their suggestions and assistance in research and dissertation writing.

To all my friends who have motivated and inspired me to strive towards my goals, a very special thanks to all of you who have lent your helping hands during my time in The University of Alabama. Lastly, I would like to acknowledge the funding source from the Department of Chemistry and Biochemistry, College of Arts and Sciences, Graduate School, the National Science Foundation award CHE 1508192 and OIA 1539035 and the Alabama EPSCoR graduate research scholars program.

CONTENTS

ABSTRACT	ii
DEDICATION	iv
LIST OF ABBREVIATIONS AND SYMBOLS	v
ACKNOWLEDGEMENTS	ix
LIST OF TABLES	xiv
LIST OF FIGURES	xv
CHAPTER 1 INTRODUCTION	1
1.1 Unique Physical and Chemical Properties of Metallic Nanoparticles	1
1.2 Metallic NPs with Both Localized Surface Plasmon Resonance and Electrocatalytic Capability	3
1.3 Spectroscopy Enhancement of Plasmonic NPs for Understanding Redox Activities of Catalyzed Reactions	6
1.4 Basis of Solar Energy Harvesting and Conversion	7
1.5 Plasmonic Nanostructures in Photoelectrochemical Water Splitting	10
1.6 Challenges of Quantitative Analysis of Single NPs	12
1.7 Research Goals, Strategies and Major Results of This Dissertation and Brief Outline of the Content	13
1.8 References	15
CHAPTER 2 EXPERIMENTAL METHODS	24
2.1 Introduction	24
2.2 Materials Preparation Techniques	24
2.2.1 Electrodeposition	24

2.2.2 Photolithography	26
2.2.3 Ion Milling.....	27
2.2.4 O ₂ Plasma Etching.....	28
2.2.5 Picoliter Dispensing.....	29
2.3 Material Characterization Techniques	30
2.3.1 Cyclic Voltammetry	30
2.3.2 Amperometry.....	31
2.3.3 Dark-Field Scattering Microscopy	31
2.3.4 Scanning Electron Microscopy.....	33
2.3.5 Transmission Electron Microscopy	36
2.3.6 UV-Vis Absorption Spectroscopy	38
2.3.7 Scanning Photoelectrochemical Microscopy.....	39
2.3.8 Photoelectrochemical Characterization	41
2.3.9 Mott-Schottky Analysis.....	43
2.3.10 Electrochemical Impedance Spectroscopy	44
2.4 References.....	45
CHAPTER 3 DARK-FIELD SCATTERING SPECTROELECTROCHEMISTRY	
ANALYSIS OF HYDRAZINE OXIDATION AT GOLD NANOPARTICLES-MODIFIED	
TRANSPARENT ELECTRODES	
3.1 Abstract	48
3.2 Introduction	49
3.3 Experimental.....	52
3.3.1 Reagents and Materials.....	52
3.3.2 ITO UME Fabrication	53
3.3.3 Au NPs Modification.....	54
3.3.4 Light Scattering Spectroelectrochemistry Study of Hydrazine Oxidation	54

3.3.5 Electrocatalytic Hydrazine Oxidation and DFS	55
3.4 Results and Discussion.....	56
3.4.1 Cyclic Voltammetry of Bare Au NPs in PBS and Hydrazine Oxidation at Planar Au NPs-ITO Electrodes.....	56
3.4.2 Light Scattering Spectroelectrochemistry Response of Hydrazine Oxidation	59
3.4.3 DFS-EC Spectroelectrochemistry Method to Resolve Hydrazine Oxidation at Single Au NPs on Planar ITO Electrodes.....	65
3.4.4 Formation of Single Au NPs on ITO UME for DFS Spectroelectrochemistry Study of Hydrazine Oxidation	70
3.4.5 Scattering Simulations Using Mie Theory and COMSOL Multiphysics for Understanding the Effect of Local Refractive Index and Shell Thickness on Plasmon Scattering by Single Au NPs	76
3.5 Conclusions	81
3.6 References.....	82
CHAPTER 4 SPECTROELECTROCHEMISTRY STUDY OF Au@Pt CORE-SHELL NANOPARTICLE ELECTRODES FOR CONTROLLED METHANOL AND FORMIC ACID OXIDATION	86
4.1 Abstract	86
4.2 Introduction	87
4.3 Experimental	88
4.3.1 Reagents and Materials.....	88
4.3.2 Synthesis of Au@Pt NPs	89
4.3.3 Characterization of Au@Pt NPs.....	89
4.3.4 In-Situ Dark-Field Scattering Measurements	90
4.4 Results and Discussion.....	90
4.4.1 Electrochemical and Morphological Study of Au@Pt NPs	91
4.4.2 CV and Light Scattering Spectroelectrochemistry Analysis for Methanol Oxidation .	94
4.4.3 CV and Light Scattering Spectroelectrochemistry Analysis for Formic Acid Oxidation	99

4.5 Conclusions	100
4.6 References.....	101
CHAPTER 5 PHOTOELECTROCHEMICAL PERFORMANCE OF Au-INCORPORATED HEMATITE FOR SOLAR WATER SPLITTING: SECM AND BULK STUDY	104
5.1 Abstract	104
5.2 Introduction	105
5.3 Experimental	109
5.3.1 Reagents and Materials.....	109
5.3.2 SPECM Screening of the 10×10 Photocatalyst Array Spots.....	109
5.3.3 Fabrication of Bulk Au-incorporated Hematite Thin Film Photoelectrode.....	111
5.3.4 Characterization of Materials and Electrodes.....	111
5.3.5 Substrate Generation Tip Collection SECM Measurements	113
5.4 Results and Discussion.....	114
5.4.1 SECM for Searching Optimal Au Concentration of Hematite Photoanode	114
5.4.2 Absorption Spectra and Morphology of Au-incorporated Hematite Films	115
5.4.3 XPS Characterization of Au-incorporated Hematite Film	118
5.4.4 PEC Characterization of Au-incorporated Hematite Film Photoanodes	121
5.4.5 Understanding the Carrier Density, Flat Band Potential, and Impedance of Au- incorporated Hematite Photoanodes.....	123
5.4.6 Substrate Generation Tip Collection Mode SECM Quantification of Hematite Thin Film Photoanodes	127
5.5 Conclusions	128
5.6 References.....	129
CHAPTER 6 CONCLUSIONS AND PERSPECTIVES	135

LIST OF TABLES

5.1 Recent literature on Au decorated hematite photoanode for solar water splitting.....	107
5.2 Quantification of Fe, O, Sn and Au elements in pristine and 3%Au-incorporated hematite samples	120
5.3 Summary of flat band potential and charges carrier densities obtained from Mott-Schottky plot for pristine and Au-incorporated hematite thin films	125
5.4 Summary of experimental fit parameters from fitting Nyquist plots using the equivalent circuit shown by the inset of Figure 5.12.....	126

LIST OF FIGURES

1.1 Number of journal articles and reviews published in recent ten years with keywords “nanoparticles” and “nanoparticles” + “electrocatalysis”	3
1.2 Schematic diagram of localized surface plasmon	4
1.3 Light scattering properties varies with different compositions, sizes and shapes of metal NPs	4
1.4 Schematic diagram of (a) Photovoltaic charging system and (b) Photocatalytic charging system	8
1.5 Schematic diagram of a photoelectrolysis cell.....	9
1.6 Schematic describing semiconductor catalyzed water splitting reaction.....	10
1.7 Schematic diagram of NP collision experiment.....	13
2.1 Electrodeposition of Au NPs on ITO substrate by CV method (top panel) and multistep potential method (bottom panel).....	26
2.2 Schematic of photolithography steps using a positive photoresist	27
2.3 Nb-doped hematite sample array prepared by picoliter dispensing technique	29
2.4 Cyclic voltammogram of Au NPs electrode in PBS at a scan rate of 0.1 V/s	31
2.5 Schematic diagram of a dark-field microscope	32
2.6 DFS image of Au NPs on ITO glass substrate.....	33
2.7 Illustration of signals generated by the electron beam–specimen interaction in SEM.....	34
2.8 Schematic diagram of a scanning electron microscope	35
2.9 SEM image (left), corresponding EDS mapping (middle) and EDS elemental analysis (right) of Au NPs on ITO substrate.....	35
2.10 Simplified schematic cross-sections configuration of a TEM instrument	37
2.11 TEM images of Au@Pt NPs in low (left) and high (right) magnifications	37

2.12 Schematic diagram of UV-Vis spectrometer	39
2.13 UV-Vis spectrum of ~100 nm Au NPs on ITO substrate	39
2.14 Schematic diagram of the SPECM system	41
2.15 Schematic representation of a cell setup for PEC measurements	42
2.16 I-V curve of pristine and 3% Au-incorporated hematite photoanode in 0.1 M NaOH under 1 sun illumination	42
2.17 Mott-Schottky plot of thin film hematite photoanode	44
2.18 Nyquist plots of hematite thin film under dark and 1 sun irradiation condition.....	45
3.1 Schematic diagram of ITO UME fabrication.....	53
3.2 UV-Vis absorption spectra of Au NPs modified bare ITO with different coverage	57
3.3 (A) SEM image and particle size distribution of Au NPs modified planar ITO electrode with average particle diameter of 117 (+/-18) nm and particle coverage of $1.4 \times 10^9/\text{cm}^2$; (B) Cyclic voltammograms (CVs) of 1.0 M hydrazine oxidation at a planar bare ITO, 2.0 mm (in diam.) Au disc, 117 nm Au NPs modified ITO, and a 10 μm (in. diam.) Au microelectrode.....	57
3.4 Schematic of experimental setup with a halogen lamp or a HeNe laser (632.8 nm) for probing the light scattering intensity and spectrum changes of Au NPs upon hydrazine oxidation and Au anodization	59
3.5 CVs (top) of a Au NPs-modified ITO electrode in 50 mM PBS with highest anodization potential gradually increased from -0.05 to 1.5 V vs. Ag/AgCl at a scan rate of 0.5 V/s while laser scattering responses (bottom) at 632.8 nm.....	61
3.6 CVs (left) and laser scattering responses (right) of a Au NPs-modified ITO electrode in 50 mM PBS containing hydrazine concentration from 1 μM to 100 mM at a scan rate of 0.5 V/s. The arrows indicate scanning directions.....	62
3.7 Time evolution of laser scattering intensity and current during linearly cycling the electrode potential from -0.4 V to 0.75 V and then back to -0.4 V (vs. Ag QRE) for four cycles at scan rate of 0.5 (A), 0.25 (B), 0.1 (C), and 0.05 (D) V/s. Light scattering intensity of panel A and B are plotted with a different scale from panel C and D.....	63
3.8 (A) Absorption spectrum of 117 (+/-18) nm Au NPs modified ITO and light scattering spectrum of the same sample; (B) Time evolution light scattering intensity change (ΔI) at each wavelength upon oxidation of 1 M hydrazine in 50 mM of PBS.....	65
3.9 (A) Experimental schematic of dark field scattering spectroelectrochemistry (DFS-EC) setup for hydrazine oxidation at single Au NPs (B) Typical SEM image of 176 (+/- 43) nm	

Au NPs electrodeposited onto an ITO working electrode (C) DFS image showing a bright light scattering of Au NPs.....	67
3.10 (A) statistical distribution of initial DFS intensities of single Au NPs and a typical DFS image collected with an EMCCD (inset); (B) summed DFS intensity and electrode current responses of > 150 Au NPs to electrode potential scanning from -0.4 V to 0.75 V then back to -0.4 V (vs. Ag/AgCl) at a scan rate of 0.5 V/s for four cycles; (C) Typical DFS response profile of a selected single Au NP and current of the entire Au NP modified ITO electrode; (D) DFS signal decrease amplitude I dependence of the initial light scattering intensity I_0 of single Au NPs.....	69
3.11 (top) Time evolutions of light scattering intensity relative to initial light intensity I/I_0 of seven selected single Au NP and average variation of scattering intensity I/I_0 of the total 150 Au NPs when the electrode potential was cycled linearly from -0.4 V to 0.75 V and then back to -0.4 V (vs. Ag/AgCl) for four cycles at a scan rate of 0.5 V/s; (bottom) Time evolutions of I/I_0 of all 150 Au NPs in DFS frame when the electrode potential was cycled linearly from -0.4 V to 0.75 V and then back to -0.4 V (vs. Ag/AgCl) for four cycles at a scan rate of 0.5 V/s.....	70
3.12 (A) SEM images of a bare ITO UME in low magnification (a), a zoom-in image of ITO electrode (b), SEM (c) and DFS (d) images of Au NPs-modified ITO UME; (B) DFS intensity of five Au NPs highlighted in (a) of panel A and corresponding particle diameter estimated by SEM at the same location	72
3.13 EDS result of Au NPs modified ITO UME. DFS image (top left) and high resolution SEM image (top right) show the size and shape of UME. EDS spectra (bottom right) indicates the element formation and abundance	73
3.14 10 mM ferrocyanide oxidation on 10 μm ITO UME.....	73
3.15 (A) three consecutive CVs of a few Au NPs modified ITO UME (colored) in 50 mM hydrazine in contract to sluggish reaction at bare ITO UME (black). Inset: SEM image of the Au NPs-modified ITO UME; (B) CVs of hydrazine oxidation and scan rate dependence in 1.0 M hydrazine solution at a few Au NPs modified ITO UME. Inset: SEM image of the Au NPs modified ITO UME.....	75
3.16 DFS intensity and current trajectories of two selected single Au NPs on a 10 μm (in diam.) ITO UME. One Au NP is located on the exposed ITO UME (red), and the other Au NP is buried under the insulating layer outside the ITO UME (black).....	75
3.17 (A) DFS light collection and incident light geometry that is used in DFS-EC equipment for calculating light scattering intensity with Mie theory; (B) Simulated light scattering spectrum of a single 100 nm (in diam.) Au NP in media with various refractive indexes from 1.33 to 1.00; (C) Mie simulation of light scattering intensity in dependences of medium refractive index. (D) Simulated light scattering intensity as a function of Au NP size	77
3.18 (A) Simulation geometry for scattering simulations consisting of a core-shell Au-Au ₂ O ₃ NP at the planar interface of ITO and water (left) and example calculated field distribution,	

given as the ratio of the scattered to incident fields for a 48 nm core radius, 3.7 nm shell thickness, and a wavelength of 650 nm (right). (B) Calculated scattering spectra and scattering intensities at specific wavelengths for the core-shell structure during anodization as a function of inner r_{Au} . r_{Au} and $r_{Au_2O_3}$ are related as described in the text. (C) Calculated scattering intensities at 633 nm for $r = 50$ nm Au NPs with varying thicknesses of N_2 or N_2H_3 shells	80
3.19 Au nanoparticle collision experiment on 10 μ m ITO UME under 0.3 V vs. Ag QRE. Inset is the zoom in of the red rectangular area	82
4.1 (A) Cyclic voltammograms of 3 mM H_2PtCl_6 on bare ITO and Au-modified ITO (Scan rate: 0.1 $V s^{-1}$). (B) Chronoamperometric deposition of Pt NPs on Au-modified ITO substrate for 20 cycles	91
4.2 SEM images of Au-ITO, Au@Pt(1) and Au @Pt(30) and their particle sizes distribution analysis. The scale bar reads 100 nm.....	93
4.3 (A) HRTEM image of Au@Pt(30) sample with the Au core and Pt shell. (B) HAADF-STEM-EDS elemental mapping images of the same sample showing the Au-Pt core-shell structure.....	94
4.4 UV-vis absorption spectra of Au-ITO and Au@Pt NPs samples	94
4.5 CVs of 0.5 M methanol in 0.1 M NaOH solution for Au-ITO and Au@Pt NPs samples. (Scan rate: 0.1 $V s^{-1}$; Arrows indicate the scan direction.)	96
4.6 50 successive CVs of the Au@Pt (30) sample in 0.5 M MeOH in 0.1M NaOH at a scan rate of 0.1 $V s^{-1}$	96
4.7 (A) Experimental setup for in-situ dark-field scattering spectroelectrochemistry study. CVs and dark-field scattering responses of methanol oxidation on Au-ITO (B), Au@Pt(1) (C) and Au@Pt(30) NPs (D) substrates	98
4.8 CVs and dark-field scattering responses of Au-ITO, Au@Pt(1) and Au@Pt(30) NPs in 0.1 M NaOH electrolyte without methanol recorded at the scan rate of 0.1 $V s^{-1}$	98
4.9 CVs and dark-field scattering response of Au-ITO and Au@Pt NPs in 0.1 M H_2SO_4 electrolyte containing 0.1 M formic acid at the scan rate of 0.05 $V s^{-1}$	100
5.1 Schematic of the SECM system with synthesized array as substrate	111
5.2 (A) Schematic of the substrate generation tip collection mode of SECM setup. Side (B) and top (C) view of the Pt disk microelectrode	113
5.3 (A) The array design for studying Au incorporating effects on PEC of hematite spots produced by PL dispensing technique. SECM plots of Au-incorporated hematite array on Ti substrate obtained at substrate potentials of 0.3V (B) and 0.5 V (C) vs. Ag/AgCl. (D) Statistical averaging analysis of the PEC current dependence on Au percentage	115

5.4 Normalized UV-vis spectra of pristine and Au-incorporated hematite photocatalysts incorporated with 1, 3, 5, and 10% of Au (atomic ratio). Inset: photographs of list samples	116
5.5 SEM images of Au-incorporated hematite thin film with 1% (A), 4% (B), 7% (C) and 10% (D) of Au in the film.....	117
5.6 Cross-section SEM image of spin-coat Au-incorporated hematite film with an average thickness of 100 nm	117
5.7 Survey XPS spectra of pristine and 3% Au-incorporated hematite samples on FTO	119
5.8 High-resolution XPS spectra of Fe2p, O1s, Sn3d and Au4f lines for 3% Au-incorporated hematite thin film.....	120
5.9 The J-V curves of pristine and 1, 3, 5, 10% Au-incorporated hematite thin film photoanodes under dark condition and 1 simulated sun light.....	122
5.10 Bar graph showing Photocurrent density measured at -0.2, 0, 0.2 and 0.5 V vs. Ag/AgCl for different Au percentages	123
5.11 Mott-Schottky plot of pristine and Au-incorporated hematite electrodes recorded in 0.1 M NaOH electrolyte under dark condition at an AC frequency of 1 kHz	124
5.12 Nyquist plots of Au-incorporated hematite thin films in dark condition and standard 1 sun illumination	126
5.13 Substrate current density (A) and tip current (B) of pristine and 3% Au-incorporated hematite in 0.1 M NaOH solution under 1 sun irradiation and dark condition, respectively. Substrate potential was scanned from 0 to 0.8 V vs. Ag/AgCl at a scan rate of 0.1 V S ⁻¹ , while tip potential was kept at -0.4 V vs. Ag/AgCl.....	128

CHAPTER 1

INTRODUCTION

1.1 Unique Physical and Chemical Properties of Metallic Nanoparticles

Nanomaterials are materials with sizes less than 100 nm in at least one of its dimensions. Nanomaterials can appear in various structural forms such as spherical particles, nanorods or nanowires (one-dimensional), nanosheets or ultrathin film (two-dimensional), or other three-dimensional nanostructured features.¹ Interesting physical and chemical properties can be obtained from nanomaterials in comparison to their bulk counterparts due to the large surface-to-volume ratio for nanostructured materials and/or quantum confinement effect.² Unique electronic structure accompanied with interesting physical and chemical properties of the nanomaterials because of the size effect and surface activities provide a platform for possible signal transduction of molecule recognition events which is not necessarily achievable with a bulk structure.³

Owing to the unique physical and chemical properties of electron-rich metallic nanoparticles (NPs), they have been extensively studied and broadly applied in industrial, environmental, biomedical and energy-related fields.⁴⁻⁶ For example, the antibacterial property of Ag NPs has been studied because of they can penetrate cell membranes and bind to cellular structures such as proteins and they are incorporated into wound bandage, bone cements and implants.⁷ Au NPs have been applied in diagnostic, therapeutic and targeted cancer treatment considering of their optical and anticancer properties.⁸ In terms of environmental applications, it

is found that Pd NPs can effectively catalyze the reduction of Cr(VI) to the relatively non-toxic Cr(III).⁹ Metallic NPs have been broadly applied to electrochemical systems such as fuel cells, solar cells and photoelectrochemical devices for catalyzing energy conversion efficiently. The compositions, sizes and shapes of catalytic metal NPs can be engineered to tune their catalytic performance.¹⁰⁻¹³ For example, Pt and Pt alloy NPs enable fast kinetics of chemical fuel oxidation in fuel cells.¹⁴ Au NPs have been applied to water gas shift reaction for hydrogen production¹⁵, the production of methyl glycolate¹⁶ and catalytic oxidation of fuels¹⁷. Such noble metals and composites made of Au and Pt has been extensively studied on hydrogen evolution reactions (HER), oxygen evolution reactions (OER), CO₂ reduction reactions and chemical fuel oxidation reactions. Figure 1.1 shows the number of journal article publications of NPs in the field of electrocatalysis. This bar graph represents the statistical analysis of annual publications by searching journal articles with keywords “nanoparticles” and “electrocatalysis” from 2009 to 2018 through the database of ACS Chemical Abstract’s SciFinder. NPs have been intensely investigated in scientific community to explore their new properties, functions and applications in areas such as sensing, catalysis and structural materials. The number of articles of NPs published in the field of electrocatalysis is quadrupled from 2009 to 2018 because of their unique catalytic properties and potential to replace expensive bulk noble metals.

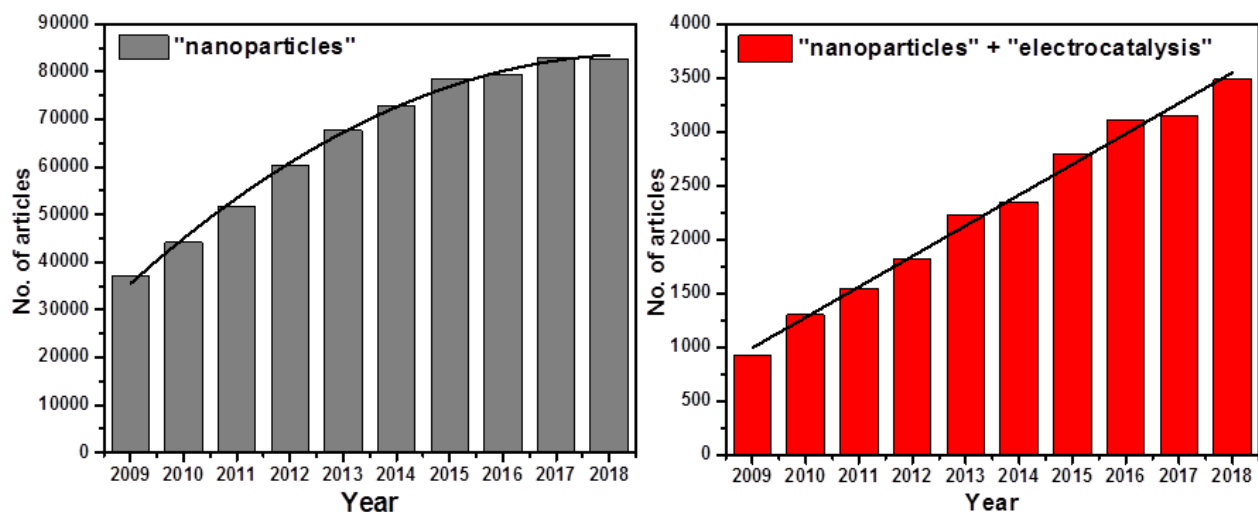


Figure 1.1: Number of journal articles and reviews published in recent ten years with keywords “nanoparticles” and “nanoparticles” + “electrocatalysis”. (Data obtained from SciFinder.)

1.2 Metallic NPs with Both Localized Surface Plasmon Resonance and Electrocatalytic Capability

Localized surface plasmon resonance (LSPR) spectroscopy is a powerful tool used in many chemical and biological sensing areas. LSPR is a coherent vibration of the surface conduction electrons of materials such as metallic NPs excited by electromagnetic radiation. These metallic NPs possess a negative real and small positive imaginary dielectric constant to support such coherent resonance motions of surface electrons.¹⁸ The interaction between the electromagnetic wave and the metallic NP can be resolved optically through the following three methods under the plasmon resonance condition: 1) angle resolved (reflectivity of light from the metal surface as a function of angle of incidence at constant wavelength); 2) wavelength shift (reflectivity of light from the metal surface as a function of wavelength at constant angle); 3) imaging (constant angle and wavelength then map the reflectivity of the surface as a function of position).¹⁹⁻²¹ These spatial distribution of scattered light intensity and wavelength dependence of LSPR of metallic NPs provide insights into the light-matter interaction mechanism and LSPR

can also be very sensitive to surrounding environment such as surface chemical modifications.

Figure 1.2 shows the schematic diagram that illustrating the LSPR, where the electric field could interact with the electron cloud from a much smaller metal sphere than the incident light wavelength. Because of the surface plasmon resonance, the light absorption and scattering of plasmonic NPs varies with their size and shapes, as shown in Figure 1.3.

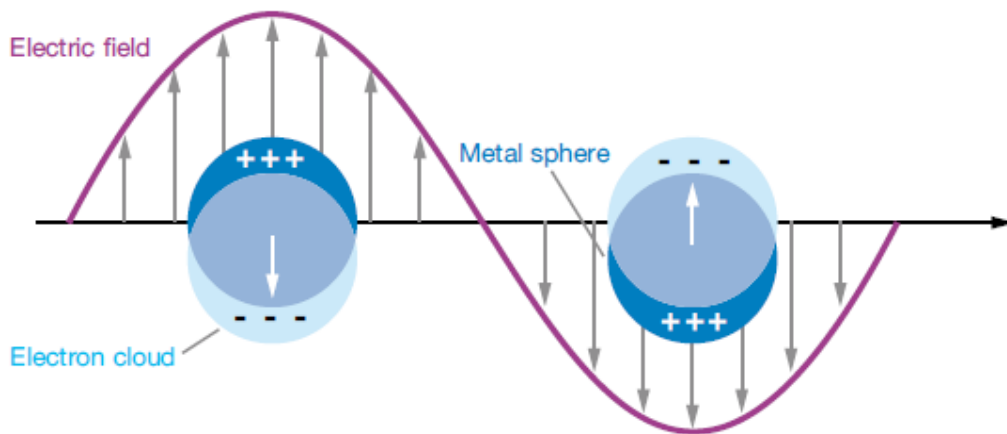


Figure 1.2: Schematic diagram of localized surface plasmon. (Reproduced with permission from Reference 18.)

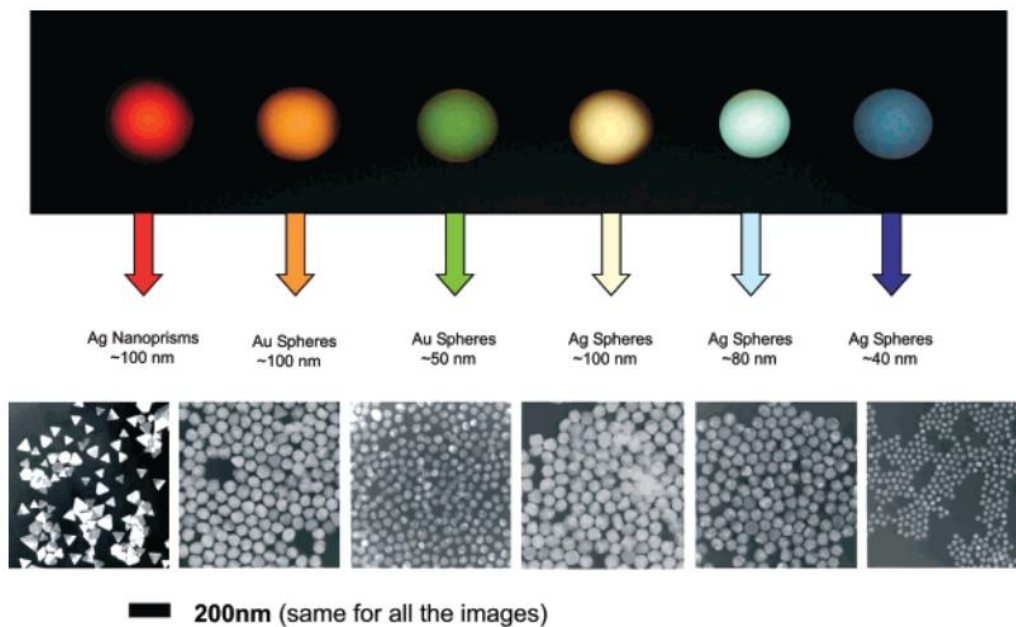


Figure 1.3: Light scattering properties varies with different compositions, sizes and shapes of metal NPs. (Reproduced with permission from Reference 2.)

The Au NP is a perfect material for studying LSPR because its stability, visible region absorption and advanced light scattering properties. Au nanostructures are widely applied in nanofabrication including nanosphere lithography²²⁻²⁴, photolithography²⁵⁻²⁶ and electron-beam lithography²⁷⁻²⁹. Normally, these fabrication techniques result in Au nanopatterns which are suitable for various kinds of spectroscopic measurements. Transmission UV-vis spectroscopy measures the extinction spectrum (the sum of absorption and scattering) of the NPs by recording the wavelength dependence of the light passing through the sample. In the case of nontransparent samples, reflectance spectra could be collected from the reflected light from the metal NPs surface. Dark-field scattering (DFS) microscopy brings the excitation light at a higher angle and collects the scattering light at a lower angle, thus is a powerful tool of measuring single-nanoparticle scattering spectra. Moreover, Au nanostructured patterns are believed to be an ideal surface modification for surface-enhanced Raman spectroscopy where the sample is excited by a laser and the Raman shift is measured.³⁰

In addition, noble metallic NPs are also favored for electro-oxidation of small organic molecules due to their abundant active sites and low-coordination atoms on the surface.³¹ Au is found to have enhanced oxidation of small alcohols, such as methanol, ethanol and glycerol in alkaline solutions.³² Stanley et al.³³ studied the effects of pH and composition on the ethanol electro-oxidation reaction through Au nanoelectrodes. They found the current density of ethanol oxidation increases rapidly with pH, which suggested alkaline condition was more favorable for ethanol oxidation on Au electrodes. A similar situation has been found for CO oxidation.³⁴ Compared with single component NPs, metal nanocomposites have been discovered to hold promising catalytic activity for chemical fuel oxidation reactions. For example, Li et al.³⁵ synthesized Pt-Ni nanocomposite and achieved a 2.065 mA cm⁻² current for methanol oxidation

reaction. Moreover, AuPt alloy foam films nanostructure is introduced by electrodeposition to remove CO_{ads} poisoning during methanol oxidation.³⁶

Although many efforts have been made, challenges still exist in this field. The precise control of nanostructured metal composites and surface modification is still challenging. Besides, the exact mechanism of chemical fuel oxidation on metal nanostructures is still uncertain. Developing noble metal nanostructures in a low-cost and large-scale fashion is also very important for these electrocatalysts.

1.3 Spectroscopy Enhancement of Plasmonic NPs for Understanding Redox Activities of Catalyzed Reactions

LSPR spectroscopy offers many advantages for sensing and spectroscopy experiments³⁷⁻³⁸. First, LSPR spectroscopy is able to provide thermodynamic and real-time kinetic status for local redox processes. Second, LSPR spectroscopy is extremely sensitivity to changes in the bulk/local refractive index even in a very small range such as a molecular adsorption layer.³⁹ Fundamental spectroscopy for plasmonic NPs provides both LSPR wavelength information and the surface enhancement factor of such materials, which is critical when designing them for sensing applications. The measurement of LSPR spectrum includes transmission/reflectance UV-vis spectroscopy, dark-field scattering and surface-enhanced Raman spectroscopy (SERS).^{21, 24, 30}

Researchers have used SERS on plasmonic materials for understanding redox activities of catalyzed reactions. In the initial research, Van Duyne and coworkers studied the SERS responses and enhancement factors as a function of surface morphology,⁴⁰ surface adsorbates and catalytic reactions⁴¹⁻⁴² on Au and Ag nanosphere substrates fabricated by nanosphere lithography.²² Further work has been carried out to determine the effects on the SERS intensity by varying the electrochemical system. These studies have been followed up even under a

monolayer or a single molecule level,⁴³⁻⁴⁵ such as the SERS of a single rhodamine 6G molecule on silver substrate performed by Dieringer et al. which used a tunable optical parametric oscillator as the excitation source.⁴⁶ More recently, in situ SERS has been applied to probe the detailed products and intermediates generated during electrochemical catalytic reactions.⁴⁷⁻⁴⁸ For example, the reaction intermediates for oxygen reduction reaction was studied at single-crystal Pt surfaces using in situ SERS by Dong and coworkers.⁴⁷ In this study, HO_2^* was found to form at Pt(111) surface while the formation of OH^* was found at Pt(110) and Pt(100) surfaces in acidic condition. Under alkaline condition, the authors believed O_2^- was formed at all single-crystal Pt surfaces. Furthermore, core-shell NPs have been developed to hold both catalytic activity and enhancement of Raman spectroscopy.⁴⁹ In the work of Jeong et al., SERS has been obtained on core-shell nanoparticle structures to monitor the generation of CO during the electro-oxidation of formic acid.⁵⁰ Notably, the spectroscopic enhancement of plasmonic NPs offers an effective and reliable way to investigate electrochemical catalytic processes in real time with high reproducibility.

1.4 Basis of Solar Energy Harvesting and Conversion

The global energy consumption in the year of 2018 is close to 170,000 TWh according to the Global Energy Statistical Yearbook 2018. Among the total energy, only less than 15% is from clean renewable energy such as such as hydroelectric energy, wind, geothermal energy, nuclear energy and solar energy. The estimated power of solar energy reaching the earth's surface is 100,000 TW. This means that one and half hours of energy from sunlight is equivalent to the total global energy consumed in an entire year.⁵¹⁻⁵² Thus, developing new technology to make full use of the abundant solar energy has been recognized as a promising and effective way for our long-term energy demand and environmentally friendly development.⁵³⁻⁵⁵

According to the different paths of energy conversion during the charging and discharging processes, the solar energy harvesting and conversion systems can be separated into two groups. First, as shown in Figure 1.4(a), there are no photo-induced redox reactions during the conversion process. For example, the most common use of solar energy is to generate electricity from solar panels and store it with effective electrochemical energy storage devices such as rechargeable batteries.⁵⁶ However, the major drawback of the current solar energy usage is that the efficiency is still at a very low level. The limitation of electrochemical energy storage is also a drawback of the solar energy usage. Second, photo-induced redox reactions (water splitting, CO₂ reduction, etc.) are involved in the energy conversion and storage processes in a photocatalytic system (Figure 1.4(b)). Photoelectrochemical water splitting and CO₂ reduction are good examples for photocatalytic system, which converts solar energy into chemical bonds for further applications.

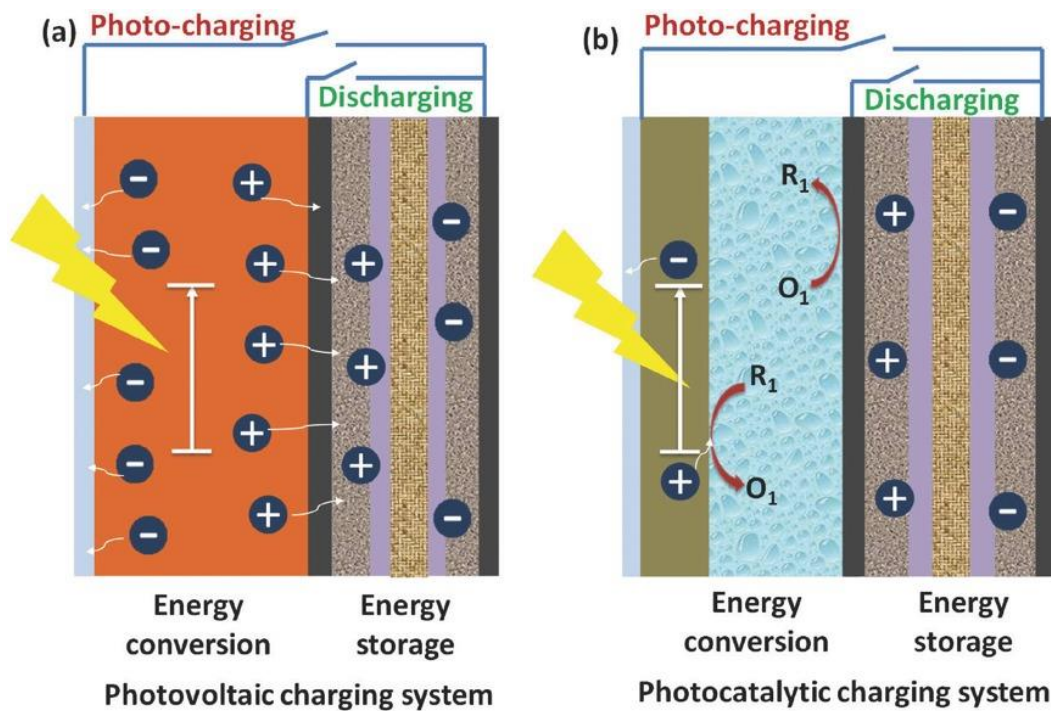


Figure 1.4: Schematic diagram of (a) Photovoltaic charging system and (b) Photocatalytic charging system. (Reproduced with permission from Reference 56.)

The method to harvest solar energy through photolysis of water to generate oxygen and hydrogen is of great interest in recent years due to the high energy density, elemental abundance and zero-emission of hydrogen fuel.^{54, 57-59} Photoelectrochemical water splitting using sunlight has been intensively studied for sustainable generation of hydrogen fuel since the discovery of electrochemical photolysis on TiO_2 .⁶⁰ A typical photoelectrochemical cell (PEC) consists of three parts: photoactive anode, counter electrode, reference electrode and electrolyte, as shown in Figure 1.5. Commonly an n-type semiconductor forms the anode which evolves oxygen by light illumination and hydrogen is generated at the cathode. The electrons are transferred from the anode to the cathode to carry out the water reduction reaction.

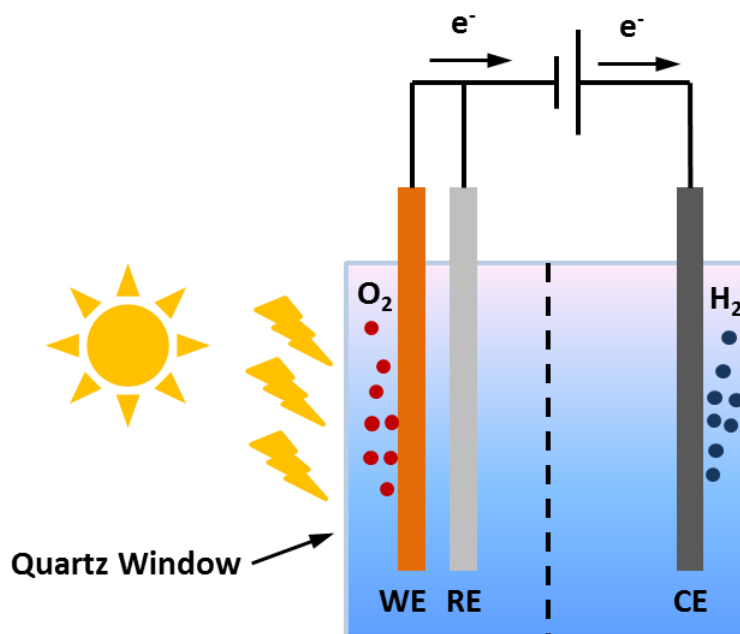


Figure 1.5: Schematic diagram of a photoelectrolysis cell

The water oxidation potential at standard condition of 25°C is 1.23 eV .⁶¹ This energy corresponds to a photon with wavelength of 1000 nm or lower. Therefore, the energy requirement of the water oxidation reaction could be easily fulfilled under sunlight irradiation,

which majorly consists of visible region (380 – 780 nm). A semiconductor with a band gap ≥ 1.23 eV can perform as a light harvesting material for the water splitting reaction.⁶¹⁻⁶³ Upon solar irradiation, inside the semiconductor, electrons in the valence band (VB) are excited to the conduction band (CB) leaving holes (h^+) in the valence band. The photo generated electrons and holes pairs will then reduce protons to H_2 and oxidize water to form O_2 at 1.23 V vs. NHE, as shown in Figure 1.6. The two half reactions described as Hydrogen Evolution Reaction (HER) and Oxygen Evolution Reaction (OER) are shown in Eqn. (1) and (2), respectively.

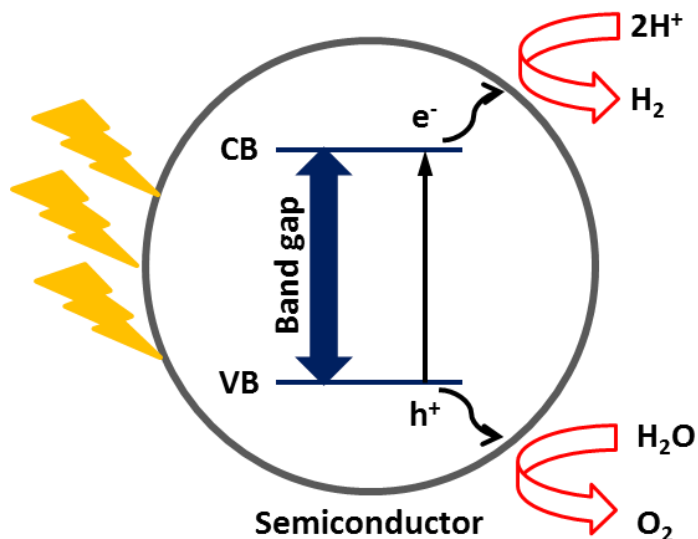
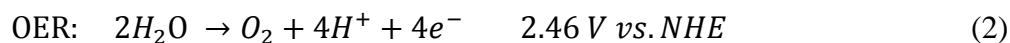
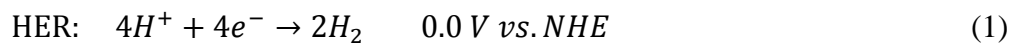


Figure 1.6: Schematic describing semiconductor catalyzed water splitting reaction.

1.5 Plasmonic Nanostructures in Photoelectrochemical Water Splitting

Metallic nanoparticles such as Au, Ag and Al NPs have been extensively investigated to reveal their role in light energy harvesting, photocatalysis, and solar cells. Photoconversion can be enhanced in semiconductors by plasmon via light trapping and hot electron/hole transfer.⁶⁴ A

recent review article from Wei David Wei's group⁶⁵ has revealed the mechanism of surface-plasmon-driven hot electrons in photoelectrochemistry. Plasmon-induced hot electron generation and transfer on metal/semiconductor and metal alloys have been discussed in detail. The Atwater group has focused on CO₂ reduction reactions with plasmonic Au-based materials. They have demonstrated the hot electron collection from Au NPs cooperate with p-type GaN for CO₂ reduction.⁶⁶ In a follow-up study, they report that nanoporous Au exhibits promising electrocatalytic activity for CO₂ reduction to CO. A remarkable current of 6 mA cm⁻² is achieved with a maximum Faradaic efficiency for CO of 99% at -0.5 V vs. RHE. The enhancement is attributed to the large electrochemical surface area of the porous structure.⁶⁷

Researchers have also found that plasmonic nanomaterials have interesting properties that could potentially fulfill the limitations for bulk semiconductor materials in terms of solar water splitting. The absorption of plasmonic nanomaterials is able to be tuned to absorb in a specific wavelength region by varying their sizes and shapes.² The sizes of nanomaterials (0 – 100 nm in at least one dimension) are comparable to charge carrier transfer lengths, thus significantly increasing the charge carrier collection efficiency.⁶⁸ Many plasmonic nanostructures have been incorporated with semiconductor photocatalysts for enhanced solar energy driven water splitting reactions. For example, Au nanohole array pattern has been introduced to α -Fe₂O₃ thin films by Wu and coworkers using nanosphere lithography. The enhancement of light collection and the LSPR was found to be the major contribution of the high photoelectrochemical efficiency.⁶⁹ More recently, plasmonic 10% Au-90% Ag film was sputtered at the bottom of α -Fe₂O₃ films as a back-reflector to maximize the light absorption of hematite film. The photocurrent reached 1.44 mA cm⁻² @ 1.23 V vs. RHE in 1 M NaOH (pH = 13.6) with the support of back-reflector.⁷⁰ Besides, solution chemistry decoration⁷¹, dropwise deposition⁷² and physical evaporation⁷³ are

also utilized to modify photocatalysts with plasmonic nanostructures for enhanced solar water splitting. In previous studies from our group, Au NPs and Au nanorods (NRs) have been successfully incorporated in hematite thin films to improve the photoactivity for solar water splitting. It was discovered that Au NPs deposited underneath the hematite film increases the chances of light absorption in visible region, thereby leading to maximizing the photogenerated charge carriers in the film for enhanced solar water splitting reaction. Furthermore, the decoration of Au NRs on top of hematite thin film electrode using electrostatic forces exhibited a plasmon enhancement towards water oxidation at higher bias potentials and resonance plasmon wavelengths.⁷⁴⁻⁷⁵ In addition, quantum dots⁷⁶⁻⁷⁷, bismuth vanadate (BiVO_4)⁷⁸⁻⁸² and graphene based materials⁸³⁻⁸⁶ also have been developed to improve the efficiency of solar water splitting.

1.6 Challenges in Quantitative Analysis of Single NPs

Although metallic NPs have a wide range of applications, however, producing reproducible and stable catalytic efficient NPs is quite challenging because of their high sensitivity to shape, size and surface capping ligands. Aggregation and corrosion effects on their surface under harsh conditions may also prevent their broad applications. In addition, their surface chemistry and reaction mechanism are often unknown and technically extremely challenging to quantify using conventional bulk ensemble averaging techniques.⁸⁷

Many efforts have been made to study the properties and understand the local reactions of single NPs. Collision experiments of single NPs at a carbon ultramicroelectrode (UME) are the most commonly used methods to detect single NPs by recording amplified Faradaic current by single NPs.⁸⁸⁻⁹⁰ Since the electrode current is typically recorded as a result of the Faradaic and non-Faradaic processes, interactions or collisions of NPs with the electrochemically inert carbon UME results in changes of current, which can be used to detect NPs, as shown in Figure 1.7.

With this method, the NPs collision frequency could be obtained to calculate the NPs diffusion profile. Theoretical calculation of NPs sizes is able to be performed by the Faradaic current. However, the lack of optical information such as NPs shapes is a drawback of this method. Moreover, reproducibility is not possible since the diffusion of a single NP is not under control.

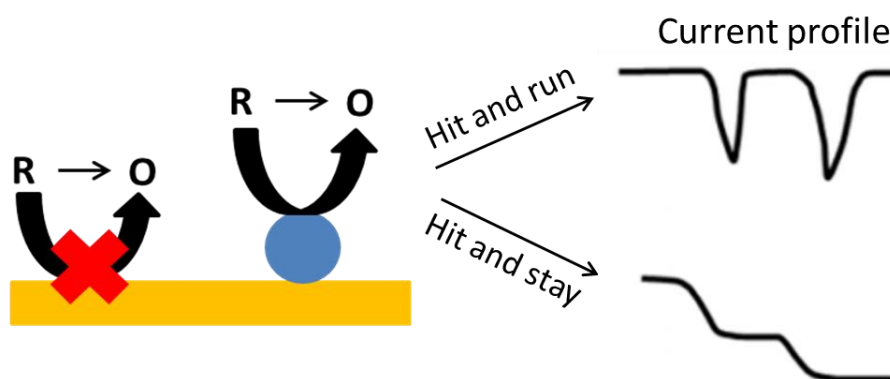


Figure 1.7: Schematic diagram of NP collision experiment

Another approach to study the electrochemical property of single NPs is to immobilize single NPs on an UME.⁹¹⁻⁹³ This technique provides more detailed size and shape information of the NP that being studied. Electrochemical detections and characterizations are commonly used to investigate the local redox reaction on the NP surface because of its proper detection limits. Besides, combined optical and electrochemical methods have been recently developed for understanding the electrochemistry of single NPs.⁹⁴⁻⁹⁷ Single NPs could be visualized by collecting the scattered light with the help of dark-field scattering microscopy. In the meantime, electrochemical reactions are able to be conducted on the NPs surfaces.

1.7 Research Goals, Strategies and Major Results of This Dissertation and Brief Outline of the Content

The major objectives of this doctoral research work are: (1) developing a light scattering based spectroelectrochemistry method to elucidate the reaction mechanisms of catalyzed redox reactions at an electrode comprised of plasmonic nanoparticles; (2) having an improved understanding of the optical and electronic effects of plasmonic nanoparticles on photoelectrochemical reaction at a metal oxide photoanode for solar water splitting.

Our strategy to achieve the first objective is to develop a semi-transparent microelectrode using micro-fabrication technique for plasmonic nanoparticle coating and imaging for spectroelectrochemistry study using single nanoparticle scattering methods developed in the Pan lab. The light scattering intensity and spectrum responses of single nanoparticles upon catalyzed redox reactions (e.g., hydrazine and chemical fuels of fuel cell) are investigated and compared with ensemble electrodes. Our strategy to achieve the second goal is to use scanning electrochemical microscope (SECM) technique to screen and quantify the effects of plasmonic metal modification on PEC performance of hematite photoanode spots produced by a picoliter (pL) dispensing technique. Furthermore, this initial study is extended to bulk thin film fabrication to resemble the SECM study followed by photoelectrochemical and spectroscopic characterization to support the optical and electronic effects.

Specifically, Chapter 3 aims to investigate the kinetics of electrocatalytic oxidation of hydrazine at Au NPs by using combine dark-field scattering and electrochemistry methods. Au NPs are electrodeposited on both transparent planar electrodes and ultramicroelectrodes. The DFS signal changing of Au NPs is correlated to different chemical events, such as Au oxidation, double layer charging and surface adsorbates, that carry out at Au NPs surfaces at high and low overpotentials. The fabrication method of ITO UME is optimized for single Au NPs detection. The particle sizes and DFS responses are correlated at the single NP level. The developed

methodology which combines ITO UME technique with DFS provides a better understanding of catalytic reactions and reproducibility than conventional electrochemical techniques.

In order to investigate the fuel cell type reactions, in Chapter 4, Au-ITO electrode is further modified by Pt to form Au@Pt and Au-Pt core-shell structures using electrochemical deposition for methanol and formic acid oxidation reaction. The thickness of Pt layer can be precisely controlled by varying the number of deposition cycles. The Au@Pt NPs displays desirable electrocatalytic activity for both methanol and formic acid oxidation than Au-ITO. This research project provides insight for side reactions and different pathways during fuel cell based redox reactions.

In Chapter 5, Au NPs are utilized as an incorporating material for hematite semiconductor for more efficient solar water splitting. The molar concentration of 3% Au is found to be optimum for enhancing the PEC performance of hematite thin film photocatalyst by SECM technique. By studying the bulk samples, significant improvements of electronic conductivity and the charge transfer resistance are found for Au-incorporated hematite thin films. Plasmonic enhancement of Au is a minimal contribution towards improvement of water oxidation reaction, which could be enhanced by controlling the size of Au NPs and the hematite film thickness. This research project brings SECM technique for Au-incorporated hematite for the first time and leads a pathway for enhancing the photocatalytic properties of hematite.

A detailed account of the studies on plasmonic Au NPs, Au@Pt NPs and Au-incorporated hematite is provided in the following chapters.

1.8 References

1. Kiss, L. B.; Söderlund, J.; Niklasson, G. A.; Granqvist, C. G., New Approach to the Origin of Lognormal Size Distributions of Nanoparticles. *Nanotechnology* **1999**, *10*, 25-28.

2. Rosi, N. L.; Mirkin, C. A., Nanostructures in Biodiagnostics. *Chem. Rev.* **2005**, *105*, 1547-1562.
3. Robenek, H., Colloidal Gold: Principles, Methods, and Applications Edited by M. A. Hayat Academic Press, Inc., New York, 1989 *Scanning* **1990**, *12*, 244-244.
4. Schröfel, A.; Kratošová, G.; Šafařík, I.; Šafaříková, M.; Raška, I.; Shor, L. M., Applications of Biosynthesized Metallic Nanoparticles – a Review. *Acta Biomaterialia* **2014**, *10*, 4023-4042.
5. Gawande, M. B.; Goswami, A.; Felpin, F.-X.; Asefa, T.; Huang, X.; Silva, R.; Zou, X.; Zboril, R.; Varma, R. S., Cu and Cu-Based Nanoparticles: Synthesis and Applications in Catalysis. *Chem. Rev.* **2016**, *116*, 3722-3811.
6. Liu, L.; Corma, A., Metal Catalysts for Heterogeneous Catalysis: From Single Atoms to Nanoclusters and Nanoparticles. *Chem. Rev.* **2018**, *118*, 4981-5079.
7. Chaloupka, K.; Malam, Y.; Seifalian, A. M., Nanosilver as a New Generation of Nanoproduct in Biomedical Applications. *Trends Biotechnol.* **2010**, *28*, 580-588.
8. Patra, C. R.; Bhattacharya, R.; Mukhopadhyay, D.; Mukherjee, P., Fabrication of Gold Nanoparticles for Targeted Therapy in Pancreatic Cancer. *Adv. Drug Deliv. Rev.* **2010**, *62*, 346-361.
9. Mabbett, A. N.; Macaskie, L. E., A New Bioinorganic Process for the Remediation of Cr(VI). *J. Chem. Technol. Biotechnol.* **2002**, *77*, 1169-1175.
10. Alivisatos, P., The Use of Nanocrystals in Biological Detection. *Nat. Biotechnol.* **2003**, *22*, 47.
11. Jin, R.; Charles Cao, Y.; Hao, E.; Métraux, G. S.; Schatz, G. C.; Mirkin, C. A., Controlling Anisotropic Nanoparticle Growth through Plasmon Excitation. *Nature* **2003**, *425*, 487.
12. Sau, T. K.; Murphy, C. J., Room Temperature, High-Yield Synthesis of Multiple Shapes of Gold Nanoparticles in Aqueous Solution. *J. Am. Chem. Soc.* **2004**, *126*, 8648-8649.
13. Sun, Y.; Xia, Y., Shape-Controlled Synthesis of Gold and Silver Nanoparticles. *Science* **2002**, *298*, 2176.
14. Chen, A.; Holt-Hindle, P., Platinum-Based Nanostructured Materials: Synthesis, Properties, and Applications. *Chem. Rev.* **2010**, *110*, 3767-804.
15. Burch, R., Gold Catalysts for Pure Hydrogen Production in the Water-Gas Shift Reaction: Activity, Structure and Reaction Mechanism. *Phys. Chem. Chem. Phys.* **2006**, *8*, 5483-5500.

16. Thielecke, N.; Vorlop, K.-D.; Prüfe, U., Long-Term Stability of an Au/Al₂O₃ Catalyst Prepared by Incipient Wetness in Continuous-Flow Glucose Oxidation. *Catal. Today* **2007**, *122*, 266-269.
17. Zhong, C.-J.; Luo, J.; Mott, D.; Maye, M. M.; Kariuki, N.; Wang, L.; Njoki, P.; Schadt, M.; Lim, S. I. I.; Lin, Y., Gold-Based Nanoparticle Catalysts for Fuel Cell Reactions. In *Nanotechnology in Catalysis: Volume 3*, Zhou, B.; Han, S.; Raja, R.; Somorjai, G. A., Eds. Springer New York: New York, NY, 2007; pp 289-307.
18. Willems, K. A.; Van Duyne, R. P., Localized Surface Plasmon Resonance Spectroscopy and Sensing. *Annu. Rev. Phys. Chem.* **2007**, *58*, 267-297.
19. Brockman, J. M.; Nelson, B. P.; Corn, R. M., Surface Plasmon Resonance Imaging Measurements of Ultrathin Organic Films. *Annu. Rev. Phys. Chem.* **2000**, *51*, 41-63.
20. Haes, A. J.; Haynes, C. L.; McFarland, A. D.; Schatz, G. C.; Van Duyne, R. P.; Zou, S., Plasmonic Materials for Surface-Enhanced Sensing and Spectroscopy. *MRS Bull.* **2011**, *30*, 368-375.
21. Kelly, K. L.; Coronado, E.; Zhao, L. L.; Schatz, G. C., The Optical Properties of Metal Nanoparticles: The Influence of Size, Shape, and Dielectric Environment. *J. Phys. Chem. B* **2003**, *107*, 668-677.
22. Haynes, C. L.; Van Duyne, R. P., Nanosphere Lithography: A Versatile Nanofabrication Tool for Studies of Size-Dependent Nanoparticle Optics. *J. Phys. Chem. B* **2001**, *105*, 5599-5611.
23. Stuart, D. A.; Yonzon, C. R.; Zhang, X.; Lyandres, O.; Shah, N. C.; Glucksberg, M. R.; Walsh, J. T.; Van Duyne, R. P., Glucose Sensing Using near-Infrared Surface-Enhanced Raman Spectroscopy: Gold Surfaces, 10-Day Stability, and Improved Accuracy. *Anal. Chem.* **2005**, *77*, 4013-4019.
24. Zhang, X.; Young, M. A.; Lyandres, O.; Van Duyne, R. P., Rapid Detection of an Anthrax Biomarker by Surface-Enhanced Raman Spectroscopy. *J. Am. Chem. Soc.* **2005**, *127*, 4484-4489.
25. Ma, Y.; Highsmith, A. L.; Hill, C. M.; Pan, S., Dark-Field Scattering Spectroelectrochemistry Analysis of Hydrazine Oxidation at Au Nanoparticle-Modified Transparent Electrodes. *J. Phys. Chem. C* **2018**, *122*, 18603-18614.
26. Ma, Y.; Highsmith, A. L.; Pan, S., Dark Field Scattering Spectroelectrochemistry of Single Au Nanoparticles at Transparent Planar and Micro-Sized Electrodes. *ECS Trans.* **2018**, *85*, 1155-1162.
27. Hicks, E. M.; Zou, S.; Schatz, G. C.; Spears, K. G.; Van Duyne, R. P.; Gunnarsson, L.; Rindzevicius, T.; Kasemo, B.; Käll, M., Controlling Plasmon Line Shapes through Diffractive Coupling in Linear Arrays of Cylindrical Nanoparticles Fabricated by Electron Beam Lithography. *Nano Lett.* **2005**, *5*, 1065-1070.

28. Wiley, B.; Sun, Y.; Xia, Y., Polyol Synthesis of Silver Nanostructures: Control of Product Morphology with Fe(Ii) or Fe(Iii) Species. *Langmuir* **2005**, *21*, 8077-8080.
29. Xu, Q.; Bao, J.; Capasso, F.; Whitesides, G. M., Surface Plasmon Resonances of Free-Standing Gold Nanowires Fabricated by Nanoskiving. *Angew. Chem.* **2006**, *118*, 3713-3717.
30. McFarland, A. D.; Young, M. A.; Dieringer, J. A.; Van Duyne, R. P., Wavelength-Scanned Surface-Enhanced Raman Excitation Spectroscopy. *J. Phys. Chem. B* **2005**, *109*, 11279-11285.
31. Alia, S. M.; Jensen, K. O.; Pivovarov, B. S.; Yan, Y., Platinum-Coated Palladium Nanotubes as Oxygen Reduction Reaction Electrocatalysts. *ACS Catal.* **2012**, *2*, 858-863.
32. Kwon, Y.; Lai, S. C. S.; Rodriguez, P.; Koper, M. T. M., Electrocatalytic Oxidation of Alcohols on Gold in Alkaline Media: Base or Gold Catalysis? *J. Am. Chem. Soc.* **2011**, *133*, 6914-6917.
33. Lai, S. C. S.; Kleijn, S. E. F.; Öztürk, F. T. Z.; van Rees Vellinga, V. C.; Koning, J.; Rodriguez, P.; Koper, M. T. M., Effects of Electrolyte Ph and Composition on the Ethanol Electro-Oxidation Reaction. *Catal. Today* **2010**, *154*, 92-104.
34. Rodriguez, P.; Koper, M. T. M., Electrocatalysis on Gold. *Phys. Chem. Chem. Phys.* **2014**, *16*, 13583-13594.
35. Li, L.; Wu, Y.; Lu, J.; Nan, C.; Li, Y., Synthesis of Pt–Ni/Graphene Via in Situ Reduction and Its Enhanced Catalyst Activity for Methanol Oxidation. *Chem. Commun.* **2013**, *49*, 7486-7488.
36. Liu, J.; Cao, L.; Huang, W.; Li, Z., Preparation of Aupt Alloy Foam Films and Their Superior Electrocatalytic Activity for the Oxidation of Formic Acid. *ACS Appl. Mater. Interfaces* **2011**, *3*, 3552-3558.
37. Haes, A. J.; Van Duyne, R. P., A Unified View of Propagating and Localized Surface Plasmon Resonance Biosensors. *Anal. Bioanal. Chem.* **2004**, *379*, 920-930.
38. Yonzon, C. R.; Jeoung, E.; Zou, S.; Schatz, G. C.; Mrksich, M.; Van Duyne, R. P., A Comparative Analysis of Localized and Propagating Surface Plasmon Resonance Sensors: The Binding of Concanavalin a to a Monosaccharide Functionalized Self-Assembled Monolayer. *J. Am. Chem. Soc.* **2004**, *126*, 12669-12676.
39. Jung, L. S.; Campbell, C. T.; Chinowsky, T. M.; Mar, M. N.; Yee, S. S., Quantitative Interpretation of the Response of Surface Plasmon Resonance Sensors to Adsorbed Films. *Langmuir* **1998**, *14*, 5636-5648.
40. Caldwell, W. B.; Chen, K.; Herr, B. R.; Mirkin, C. A.; Hulteen, J. C.; Van Duyne, R. P., Self-Assembled Monolayers of Ferrocenylazobenzenes on Au(111)/Mica Films: Surface-Enhanced Raman Scattering Response Vs Surface Morphology. *Langmuir* **1994**, *10*, 4109-4115.

41. Campbell, D. J.; Herr, B. R.; Hulteen, J. C.; Van Duyne, R. P.; Mirkin, C. A., Ion-Gated Electron Transfer in Self-Assembled Monolayer Films. *J. Am. Chem. Soc.* **1996**, *118*, 10211-10219.
42. Yang, W. h.; Hulteen, J.; Schatz, G. C.; Van Duyne, R. P., A Surface - Enhanced Hyper - Raman and Surface - Enhanced Raman Scattering Study of Trans - 1,2 - Bis(4 - Pyridyl)Ethylene Adsorbed onto Silver Film over Nanosphere Electrodes. Vibrational Assignments: Experiment and Theory. *J. Chem. Phys.* **1996**, *104*, 4313-4323.
43. Kneipp, K.; Kneipp, H.; Bohr, H. G., Single-Molecule Sers Spectroscopy. In *Surface-Enhanced Raman Scattering: Physics and Applications*, Kneipp, K.; Moskovits, M.; Kneipp, H., Eds. Springer Berlin Heidelberg: Berlin, Heidelberg, 2006; pp 261-277.
44. Le Ru, E. C.; Etchegoin, P. G., Single-Molecule Surface-Enhanced Raman Spectroscopy. *Annu. Rev. Phys. Chem.* **2012**, *63*, 65-87.
45. Lee, H. M.; Jin, S. M.; Kim, H. M.; Suh, Y. D., Single-Molecule Surface-Enhanced Raman Spectroscopy: A Perspective on the Current Status. *Phys. Chem. Chem. Phys.* **2013**, *15*, 5276-5287.
46. Dieringer, J. A.; Wustholz, K. L.; Masiello, D. J.; Camden, J. P.; Kleinman, S. L.; Schatz, G. C.; Van Duyne, R. P., Surface-Enhanced Raman Excitation Spectroscopy of a Single Rhodamine 6g Molecule. *J. Am. Chem. Soc.* **2009**, *131*, 849-854.
47. Dong, J.-C., et al., In Situ Raman Spectroscopic Evidence for Oxygen Reduction Reaction Intermediates at Platinum Single-Crystal Surfaces. *Nature Energy* **2019**, *4*, 60-67.
48. Wang, Y.-H.; Wei, J.; Radjenovic, P.; Tian, Z.-Q.; Li, J.-F., In Situ Analysis of Surface Catalytic Reactions Using Shell-Isolated Nanoparticle-Enhanced Raman Spectroscopy. *Anal. Chem.* **2019**, *91*, 1675-1685.
49. Li, J.-F.; Zhang, Y.-J.; Ding, S.-Y.; Panneerselvam, R.; Tian, Z.-Q., Core-Shell Nanoparticle-Enhanced Raman Spectroscopy. *Chem. Rev.* **2017**, *117*, 5002-5069.
50. Jeong, H.; Kim, J., Insights into the Electrooxidation Mechanism of Formic Acid on Pt Layers on Au Examined by Electrochemical Sers. *J. Phys. Chem. C* **2016**, *120*, 24271-24278.
51. Lewis, N. S., Toward Cost-Effective Solar Energy Use. *Science* **2007**, *315*, 798-801.
52. Shang, Y.; Hao, S.; Yang, C.; Chen, G., Enhancing Solar Cell Efficiency Using Photon Upconversion Materials. *Nanomaterials* **2015**, *5*, 1782.
53. Chu, S.; Majumdar, A., Opportunities and Challenges for a Sustainable Energy Future. *Nature* **2012**, *488*, 294.
54. Dresselhaus, M. S.; Thomas, I. L., Alternative Energy Technologies. *Nature* **2001**, *414*, 332-7.

55. Graetzel, M.; Janssen, R. A. J.; Mitzi, D. B.; Sargent, E. H., Materials Interface Engineering for Solution-Processed Photovoltaics. *Nature* **2012**, *488*, 304.
56. Luo, B.; Ye, D.; Wang, L., Recent Progress on Integrated Energy Conversion and Storage Systems. *Advanced Science* **2017**, *4*, 1700104.
57. Armaroli, N.; Balzani, V., The Future of Energy Supply: Challenges and Opportunities. *Angew. Chem. Int. Ed.* **2007**, *46*, 52-66.
58. Bockris, J. O. M., The Origin of Ideas on a Hydrogen Economy and Its Solution to the Decay of the Environment. *Int. J. Hydrogen Energy* **2002**, *27*, 731-740.
59. Marbán, G.; Valdés-Solís, T., Towards the Hydrogen Economy? *Int. J. Hydrogen Energy* **2007**, *32*, 1625-1637.
60. Fujishima, A.; Honda, K., Electrochemical Photolysis of Water at a Semiconductor Electrode. *Nature* **1972**, *238*, 37.
61. Navarro Yerga, R. M.; Álvarez Galván, M. C.; del Valle, F.; Villoria de la Mano, J. A.; Fierro, J. L. G., Water Splitting on Semiconductor Catalysts under Visible-Light Irradiation. *ChemSusChem* **2009**, *2*, 471-485.
62. Abe, R., Recent Progress on Photocatalytic and Photoelectrochemical Water Splitting under Visible Light Irradiation. *J. Photochem. Photobiol. C: Photochem. Rev.* **2010**, *11*, 179-209.
63. Maeda, K., Photocatalytic Water Splitting Using Semiconductor Particles: History and Recent Developments. *J. Photochem. Photobiol. C: Photochem. Rev.* **2011**, *12*, 237-268.
64. Cushing, S. K.; Wu, N., Progress and Perspectives of Plasmon-Enhanced Solar Energy Conversion. *J. Phys. Chem. Lett.* **2016**, *7*, 666-675.
65. Zhang, Y.; He, S.; Guo, W.; Hu, Y.; Huang, J.; Mulcahy, J. R.; Wei, W. D., Surface-Plasmon-Driven Hot Electron Photochemistry. *Chem. Rev.* **2018**, *118*, 2927-2954.
66. DuChene, J. S.; Tagliabue, G.; Welch, A. J.; Cheng, W.-H.; Atwater, H. A., Hot Hole Collection and Photoelectrochemical CO₂ Reduction with Plasmonic Au/P-GaN Photocathodes. *Nano Lett.* **2018**, *18*, 2545-2550.
67. Welch, A. J.; DuChene, J. S.; Tagliabue, G.; Davoyan, A.; Cheng, W.-H.; Atwater, H. A., Nanoporous Gold as a Highly Selective and Active Carbon Dioxide Reduction Catalyst. *ACS Appl. Energy Mater.* **2019**, *2*, 164-170.
68. Joy, J.; Mathew, J.; George, S. C., Nanomaterials for Photoelectrochemical Water Splitting – Review. *Int. J. Hydrogen Energy* **2018**, *43*, 4804-4817.

69. Li, J.; Cushing, S. K.; Zheng, P.; Meng, F.; Chu, D.; Wu, N., Plasmon-Induced Photonic and Energy-Transfer Enhancement of Solar Water Splitting by a Hematite Nanorod Array. *Nat. Commun.* **2013**, *4*, 2651.
70. Kay, A.; Scherrer, B.; Piekner, Y.; Malviya, K. D.; Grave, D. A.; Dotan, H.; Rothschild, A., Film Flip and Transfer Process to Enhance Light Harvesting in Ultrathin Absorber Films on Specular Back-Reflectors. *Adv. Mater.* **2018**, *30*, 1802781.
71. Wang, L.; Zhou, X.; Nguyen, N. T.; Schmuki, P., Plasmon-Enhanced Photoelectrochemical Water Splitting Using Au Nanoparticles Decorated on Hematite Nanoflake Arrays. *ChemSusChem* **2015**, *8*, 618-622.
72. Li, C.; Wang, P.; Li, H.; Wang, M.; Zhang, J.; Qi, G.; Jin, Y., Plasmon-Driven Water Splitting Enhancement on Plasmonic Metal–Insulator–Semiconductor Hetero-Nanostructures: Unraveling the Crucial Role of Interfacial Engineering. *Nanoscale* **2018**, *10*, 14290-14297.
73. Gross Koren, M.; Dotan, H.; Rothschild, A., Nano Gold Rush: On the Origin of the Photocurrent Enhancement in Hematite Photoanodes Decorated with Gold Nanoparticles. *J. Phys. Chem. C* **2016**, *120*, 15042-15051.
74. Archana, P. S.; Pachauri, N.; Shan, Z.; Pan, S.; Gupta, A., Plasmonic Enhancement of Photoactivity by Gold Nanoparticles Embedded in Hematite Films. *J. Phys. Chem. C* **2015**, *119*, 15506-15516.
75. Wang, J.; Pan, S.; Chen, M.; Dixon, D. A., Gold Nanorod-Enhanced Light Absorption and Photoelectrochemical Performance of A-Fe₂O₃ Thin-Film Electrode for Solar Water Splitting. *J. Phys. Chem. C* **2013**, *117*, 22060-22068.
76. Dong, Y.; Wu, R.; Jiang, P.; Wang, G.; Chen, Y.; Wu, X.; Zhang, C., Efficient Photoelectrochemical Hydrogen Generation from Water Using a Robust Photocathode Formed by CdTe Qds and Nickel Ion. *ACS Sustainable Chem. Eng.* **2015**, *3*, 2429-2434.
77. Zhang, J.; Zhu, W.; Liu, X., Stable Hydrogen Generation from Vermiculite Sensitized by Cds Quantum Dot Photocatalytic Splitting of Water under Visible-Light Irradiation. *Dalton Trans.* **2014**, *43*, 9296-9302.
78. He, H.; Berglund, S. P.; Rettie, A. J. E.; Chemelewski, W. D.; Xiao, P.; Zhang, Y.; Mullins, C. B., Synthesis of Bivo₄ Nanoflake Array Films for Photoelectrochemical Water Oxidation. *J. Mater. Chem. A* **2014**, *2*, 9371-9379.
79. Monfort, O.; Raptis, D.; Satrapinsky, L.; Roch, T.; Plesch, G.; Lianos, P., Production of Hydrogen by Water Splitting in a Photoelectrochemical Cell Using a Bivo₄/Tio₂ Layered Photoanode. *Electrochim. Acta* **2017**, *251*, 244-249.
80. Yang, J.-S.; Wu, J.-J., Low-Potential Driven Fully-Depleted Bivo₄/Zno Heterojunction Nanodendrite Array Photoanodes for Photoelectrochemical Water Splitting. *Nano Energy* **2017**, *32*, 232-240.

81. Zhou, S.; Tang, R.; Zhang, L.; Yin, L., Au Nanoparticles Coupled Three-Dimensional Macroporous BivO₄/SnO₂ Inverse Opal Heterostructure for Efficient Photoelectrochemical Water Splitting. *Electrochim. Acta* **2017**, *248*, 593-602.
82. Shinde, P. S.; Peng, X.; Wang, J.; Ma, Y.; McNamara, L. E.; Hammer, N. I.; Gupta, A.; Pan, S., Rapid Screening of Photoanode Materials Using Scanning Photoelectrochemical Microscopy Technique and Formation of Z-Scheme Solar Water Splitting System by Coupling P- and N-Type Heterojunction Photoelectrodes. *ACS Appl. Energy Mater.* **2018**, *1*, 2283-2294.
83. Iwashina, K.; Iwase, A.; Ng, Y. H.; Amal, R.; Kudo, A., Z-Schematic Water Splitting into H₂ and O₂ Using Metal Sulfide as a Hydrogen-Evolving Photocatalyst and Reduced Graphene Oxide as a Solid-State Electron Mediator. *J. Am. Chem. Soc.* **2015**, *137*, 604-607.
84. Tamirat, A. G.; Su, W.-N.; Dubale, A. A.; Pan, C.-J.; Chen, H.-M.; Ayele, D. W.; Lee, J.-F.; Hwang, B.-J., Efficient Photoelectrochemical Water Splitting Using Three Dimensional Urchin-Like Hematite Nanostructure Modified with Reduced Graphene Oxide. *J. Power Sources* **2015**, *287*, 119-128.
85. Yan, Y.; Wang, C.; Yan, X.; Xiao, L.; He, J.; Gu, W.; Shi, W., Graphene Acting as Surface Phase Junction in Anatase–Graphene–Rutile Heterojunction Photocatalysts for H₂ Production from Water Splitting. *J. Phys. Chem. C* **2014**, *118*, 23519-23526.
86. Yang, J.; Zeng, X.; Chen, L.; Yuan, W., Photocatalytic Water Splitting to Hydrogen Production of Reduced Graphene Oxide/SiC under Visible Light. *Appl. Phys. Lett.* **2013**, *102*, 083101.
87. Weng, Y. C.; Fan, F.-R. F.; Bard, A. J., Combinatorial Biomimetics. Optimization of a Composition of Copper(II) Poly-L-Histidine Complex as an Electrocatalyst for O₂ Reduction by Scanning Electrochemical Microscopy. *J. Am. Chem. Soc.* **2005**, *127*, 17576-17577.
88. Xiao, X.; Bard, A. J., Observing Single Nanoparticle Collisions at an Ultramicroelectrode by Electrocatalytic Amplification. *J. Am. Chem. Soc.* **2007**, *129*, 9610-9612.
89. Xiao, X.; Fan, F.-R. F.; Zhou, J.; Bard, A. J., Current Transients in Single Nanoparticle Collision Events. *J. Am. Chem. Soc.* **2008**, *130*, 16669-16677.
90. Jung, A. R.; Lee, S.; Joo, J. W.; Shin, C.; Bae, H.; Moon, S. G.; Kwon, S. J., Potential-Controlled Current Responses from Staircase to Blip in Single Pt Nanoparticle Collisions on a Ni Ultramicroelectrode. *J. Am. Chem. Soc.* **2015**, *137*, 1762-1765.
91. Dudin, P. V.; Unwin, P. R.; Macpherson, J. V., Electro-Oxidation of Hydrazine at Gold Nanoparticle Functionalised Single Walled Carbon Nanotube Network Ultramicroelectrodes. *Phys. Chem. Chem. Phys.* **2011**, *13*, 17146-17152.
92. Chen, S.; Kucernak, A., Electrodeposition of Platinum on Nanometer-Sized Carbon Electrodes. *J. Phys. Chem. B* **2003**, *107*, 8392-8402.

93. Chen, S.; Kucernak, A., Electrocatalysis under Conditions of High Mass Transport: Investigation of Hydrogen Oxidation on Single Submicron Pt Particles Supported on Carbon. *J. Phys. Chem. B* **2004**, *108*, 13984-13994.
94. Hill, C. M.; Clayton, D. A.; Pan, S., Combined Optical and Electrochemical Methods for Studying Electrochemistry at the Single Molecule and Single Particle Level: Recent Progress and Perspectives. *Phys. Chem. Chem. Phys.* **2013**, *15*, 20797-20807.
95. Hill, C. M.; Pan, S., A Dark-Field Scattering Spectroelectrochemical Technique for Tracking the Electrodeposition of Single Silver Nanoparticles. *J. Am. Chem. Soc.* **2013**, *135*, 17250-17253.
96. Hill, C. M.; Bennett, R.; Zhou, C.; Street, S.; Zheng, J.; Pan, S., Single Ag Nanoparticle Spectroelectrochemistry Via Dark-Field Scattering and Fluorescence Microscopies. *J. Phys. Chem. C* **2015**, *119*, 6760-6768.
97. Pan, S.; Liu, J.; Hill, C. M., Observation of Local Redox Events at Individual Au Nanoparticles Using Electrogenerated Chemiluminescence Microscopy. *J. Phys. Chem. C* **2015**, *119*, 27095-27103.

CHAPTER 2

EXPERIMENTAL METHODS

2.1 Introduction

This chapter provides a brief description of the basic principles of the experimental methods and techniques used in the entire research, including the preparation and characterization of the analyzed materials. The chapter is divided into two parts: (1) materials preparation techniques: gives an overview of the sample preparation techniques that used in the research; (2) materials characterization techniques: provides a brief summary of the working principles of the materials characterization techniques, such as CV, DFS, SEM, TEM, UV-Vis spectroscopy, Raman spectroscopy and photoelectrochemical characterization techniques.

2.2 Materials Preparation Techniques

2.2.1 Electrodeposition

Electrodeposition is a class of well-known methods to produce in situ metallic coatings by the action of an electric current on a conductive material immersed in a solution containing a salt of the metal to be deposited.¹ It is usually used to improve the surface decorative and functional characteristics of an electrode. Recently, electrodeposition appears as a common technique for the preparation of nanomaterials. Metal nanoparticles, alloys, matrix composites and multilayers are prepared by using electrodeposition in the literature.²

The experimental setup of a typical electrodeposition system uses a three electrode system which consists of a counter electrode (CE), a working electrode (WE) and a reference electrode (RE). The WE normally is the cathode of the system where the metal ion is reduced and deposited. The three electrodes are immersed in an electrolyte solution which contains a typical metal salt. During the electrodeposition, metal ions are reduced on the surface of WE on where a metal film is formed. The film thickness can be controlled by deposition time. A potentiostat is used to apply potential to the system. The potential to be applied depends on the reduction potential of the metal ion and the conductivity of the substrate. The reference electrode ensures a stable and reproducible potential applied on the WE.

There are two electrodeposition processes discussed in this dissertation: (1) CV method and (2) multistep potential method. CV method is a cyclic scan of the potential which passes through the reduction potential peak of the metal by the potentiostat. Multistep potential method consists of two potentials and two deposition times that potential being applied. The first step involves the generation of the nanoparticle seeds in a very short period of time where the second step function as the growth step of these seeds. The multistep potential deposition method was developed by Penner et al. to achieve size-selective deposition of uncoupled Au and Ag NPs.³ A theoretical calculation of the uncoupled limit was reported in their work. In the previous work of the Pan group, Ag NPs⁴ and Au NPs⁵⁻⁶ with selective particle sizes were successfully obtained by the multistep potential deposition method. Figure 2.1 shows a comparison of the deposition of Au NPs on ITO substrates by CV method and multistep potential method in 0.5 mM H₂AuCl₄ with 0.1 M NaCl. It is clear to see that the sample deposited by the multistep potential method is much more uniform than that deposited by the CV method. Moreover, the particle density and size can be precisely controlled by varying the nucleation and growth potentials and times.

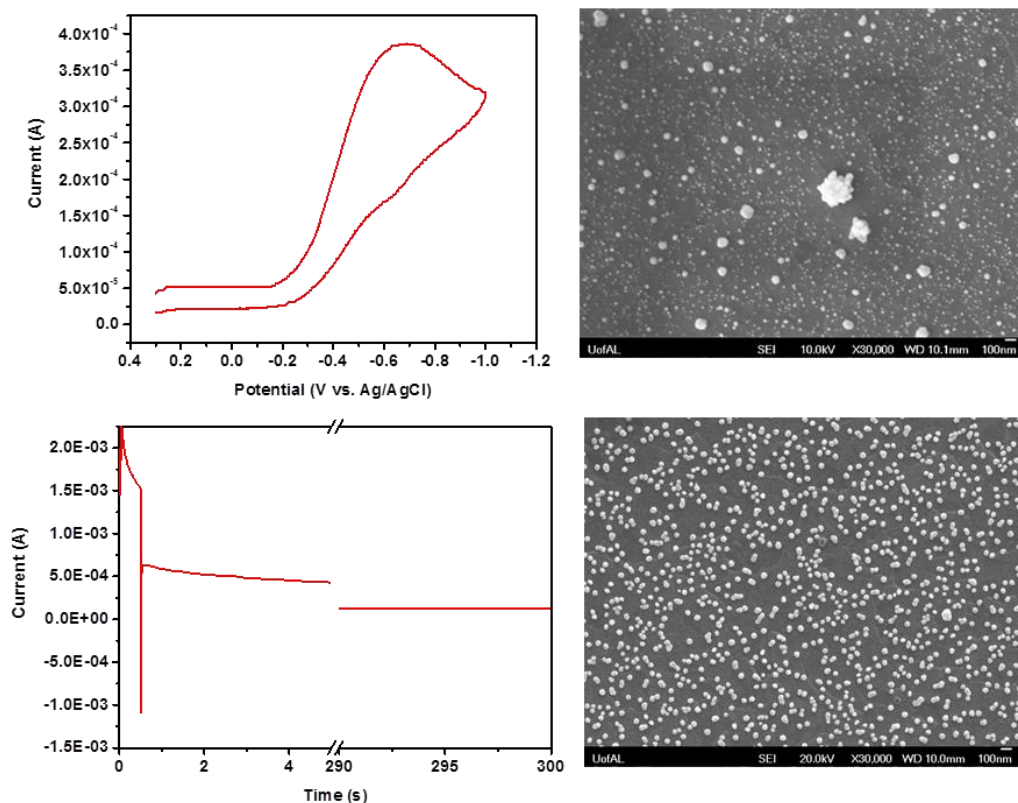


Figure 2.1: Electrodeposition of Au NPs on ITO substrate by CV method (top panel) and multistep potential method (bottom panel).

2.2.2 Photolithography

Photolithography is the process that describes and transfers a pattern onto a thin film layer on a substrate.⁷ In the process, a UV light is usually used as the light source to transfer the specific pattern onto a photosensitive layer (photoresist) through a shadow mask. The shadow mask identifies the area to be exposed and protected from the UV light. Then the thin film is developed in the chemical developer to dissolve the photoresist from the exposed area. Patterned photoresist is also used as a hard mask for many dry and wet etch processes.

A photolithography process consists of four basic steps (Figure 2.2): (1) Coat: a layer of photoresist is applied to the substrate surface by spin coating; (2) Align: align the substrate and the shadow mask precisely by alignment marks through an optical microscope; (3) Expose: the

photoresist is exposed to UV light to generate desired pattern; (4) Develop: the exposed photoresist is subsequently dissolved with a chemical developer. The type of photoresist (positive or negative) determines which part (exposed or unexposed) of the resist is dissolved. A soft bake at 90 to 100°C is applied to the substrate after spin coating in order to remove the residual solvents of the photoresist. A post-develop hard bake at 120 to 140°C is used to harden and stabilize the photoresist for following application.

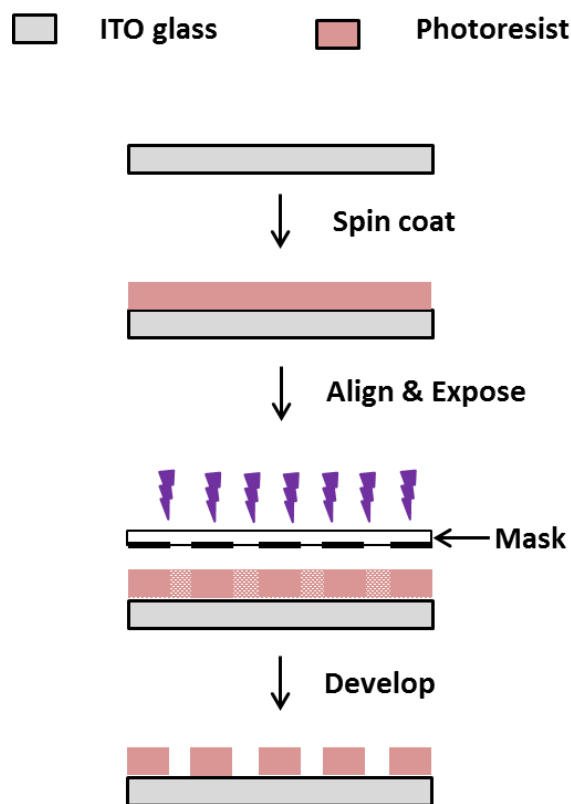


Figure 2.2: Schematic of photolithography steps using a positive photoresist.

2.2.3 Ion Milling

Ion milling is a physical etching technique that physically remove the amorphous surface of a substrate to reveal the under layer for imaging or other purposes.⁸ During the ion milling process, the ions of an inert gas (typically argon) are accelerated to an extremely high speed in a

vacuum. The pressure is usually in the lower 10^{-4} torr range. The high speed ions are neutralized by a neutralization filament before reaching the sample surface. The fully neutralized ion beam (300 to 1000 eV of energy) interacts with the sample surface at an incident angle to remove it and reveal an atomic level clean surface. In order to optimize the sample preparation time and the quality of the surface, several parameters such as the ion energy, incident angle should be adjusted throughout the process. In many applications such as electronics, semiconductors and biomaterials, a defect-free sample surface is required; thus ion mill provides a satisfactory treatment to the samples in these areas.

2.2.4 O₂ Plasma Etching

Plasma etching is a technique of etching in which plasma is used as an etchant. Plasma is formed by ionizing gas particles, through radio frequency application or heating.⁹ O₂ and Ar are normally used as the gas to generate plasma. The plasma generation system consists of two symmetrical electrodes for the generation of radio frequency and a ground electrode on which the sample to be etched is placed. A gas inlet and an outlet are connected to the chamber of the system. As the gas enters the system, high voltage is applied to partially ionize gas particles. The frequency of the power is at 13.6 MHz, which is considered as the standard plasma forming frequency. During the process, the etching chamber is evacuated. Then the chamber is filled with O₂ gas to 1 torr followed by the plasma generation for a few minutes. The benefits of O₂ plasma etching compared to the traditional acid etching are as follows: 1) O₂ plasma improves the physical properties of etched material; 2) no by-product is formed during the etching process or the by-product is volatile; 3) plasma etching is also an excellent cleaning process and removes all the unwanted organic residues from the material surface.

2.3 Materials Characterization Techniques

2.3.1 Cyclic Voltammetry

Cyclic voltammetry is a direct current (DC) electrochemical measurement, which applies different potentials to the working electrode with respect to the reference electrode while recording the output current response in the forward and reverse scans for one or several cycles. It allows the study of redox properties of compounds and interfacial structures.¹¹⁻¹² The current response is plotted versus the potential applied to give the cyclic voltammogram. The characteristics of a cyclic voltammogram depend on the type of the redox species and the nature of reaction on the electrode surface. Figure 2.4 shows a CV of Au NPs electrode in phosphate buffer solution (PBS). Au NPs are oxidized to gold oxide at 1.0 V vs. Ag/AgCl and reduced back to gold at around 0.35 V vs. Ag/AgCl, which means Au oxidation in PBS is reversible. There are several parameters involved in CVs that usually required analyzing the data: 1) scan rate: the rate of potential change over time; 2) onset potential: the potential at which the current starts to increase above the base value; 3) steady state current: usually for a microelectrode, the current at when charge flowing into any point in the circuit equals the charge flowing out.

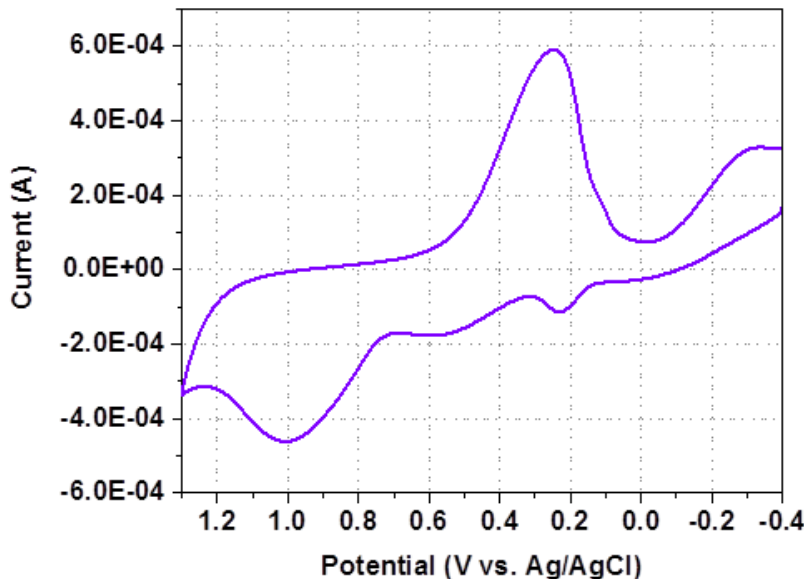


Figure 2.4: Cyclic voltammogram of Au NPs electrode in PBS at a scan rate of 0.1 V/s.

2.3.2 Amperometry

Amperometry monitors the changes in current during the reduction or oxidation of a compound at a fixed potential.¹³ Like CV, amperometry is also conducted in a three electrode system. It continuously measures the current resulting from the oxidation or reduction of a species in a redox reaction. Therefore, a current vs. time plot is obtained from this technique at a constant potential. This technique is widely used in testing the stability of a photoactive electrode by holding a certain potential for a long time.

2.3.3 Dark-Field Scattering Microscopy

A bright-field microscopy uses light that passes through the sample specimen to image. In order to build an image, the incident light rays must be changed enough and interfere with each other when passing through the specimen. However, in some cases, when a specimen has a refractive index very similar to the surrounding medium, the image could not be obtained by the conventional bright-field microscope. In order to visualize these samples, a dark-field condenser

is used to form a hollow cone of light, and the objective lens is located at a certain distance where the incident light is not collected, as shown in Figure 2.5. The hollow cone of light is focused onto the sample specimen so that the scattered light from the sample could be collected by the objective lens. As a result, the entire background field is dark and only the sample appears bright against the dark background.¹⁴ The objective can be easily coupled with an electron multiplying charge-coupled device (EMCCD) camera to record the images. A DFS image of Au NPs on ITO glass substrate is shown in Figure 2.6. Due to the scattering limit of visible light, DFS images of NPs do not provide direct size information, but spatial information is provided. The sizes of NPs could be correlated to the DFS intensities, which will be discussed in the following chapters.

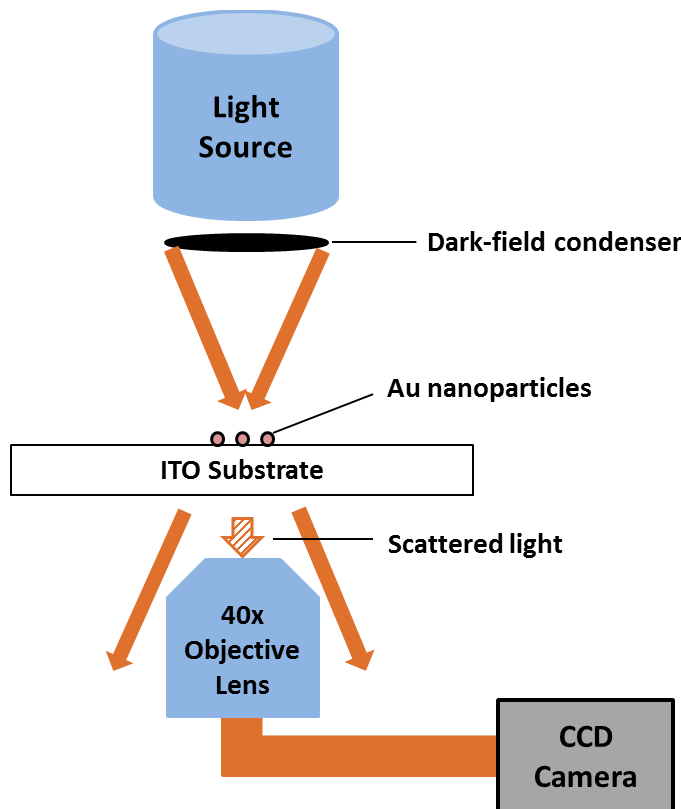


Figure 2.5: Schematic diagram of a dark-field microscope.

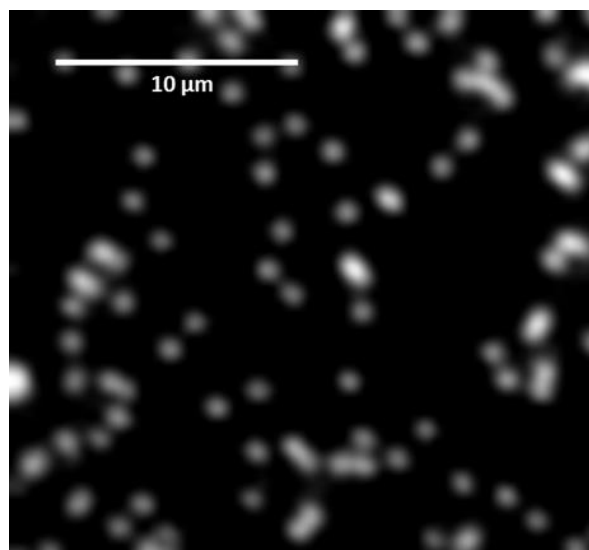


Figure 2.6: DFS image of Au NPs on ITO glass substrate.

2.3.4 Scanning Electron Microscopy

Scanning electron microscopy (SEM) is a surface imaging method that operates with the help of focused electron beam. The incident electron beam that accelerated at a high voltage (5 – 30 kV) scans across and interacts with the sample surface to generate back scattered and secondary electrons that are used to build an image of the sample (Figure 2.7). Secondary electrons which contain the topographical information about the sample surface are used to imaging the sample while back scattered electrons are used for chemical mapping. In addition to the scattering electrons generation, X-rays and Auger electrons are also generated due to the excitation and relaxation of the electrons between the energy levels. The energy of the characteristic X-rays gives information on the chemical composition of the sample. By comparing the energy of the X-rays with the library values of different elements, the elemental analysis or mapping can be obtained, which is known as the energy-dispersive X-ray spectroscopy (EDS).¹⁵

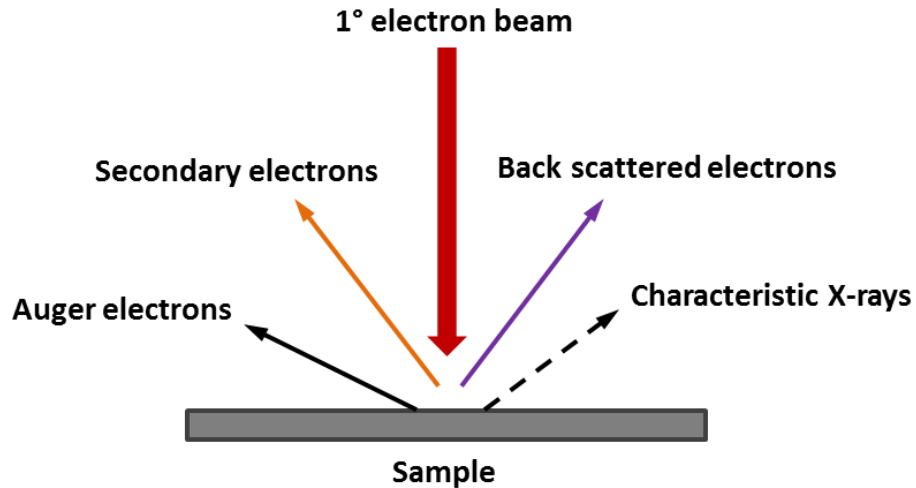


Figure 2.7: Illustration of signals generated by the electron beam–specimen interaction in SEM.

Figure 2.8 shows the column structure of a conventional SEM. The electron gun produces the electrons and accelerates them to a high energy level. The condenser lenses and apertures are used to focus and refine the electron beam to form a small focused electron spot (1 – 100 nm) on the specimen. A high vacuum ($\sim 10^{-4}$ Pa) is needed in the entire column and specimen chamber to allow electrons travel without scattering by the air molecules. The secondary electron detector detects the secondary electrons which can be processed to obtain real-time observation and image recording. An X-ray detector is utilized to analyze the elemental composition. An example of SEM image, EDS spectrum and mapping are shown in Figure 2.9.

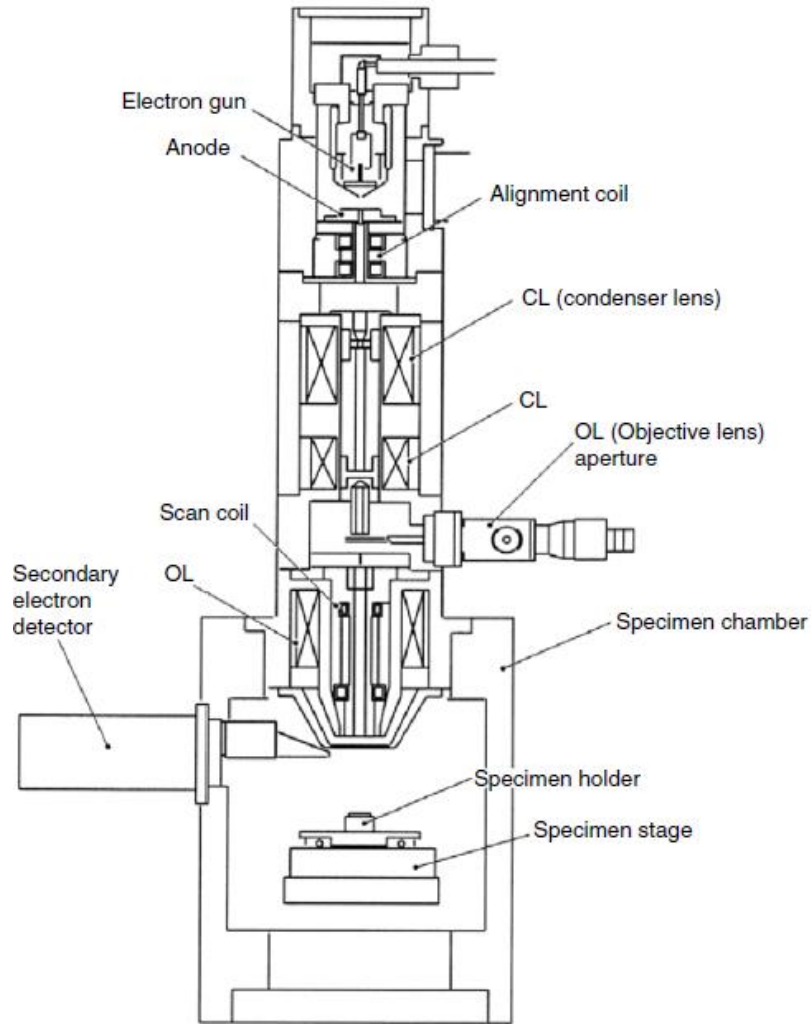


Figure 2.8: Schematic diagram of a scanning electron microscope. (Reproduced with permission from Reference 15.)

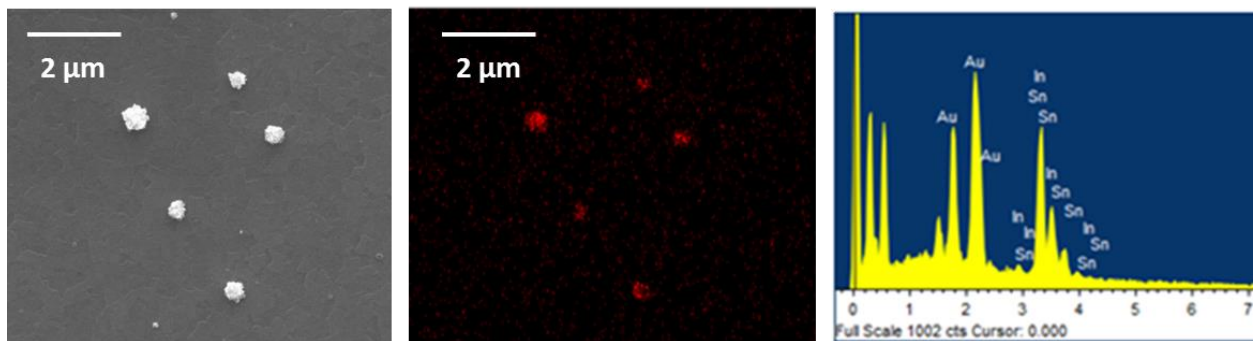


Figure 2.9: SEM image (left), corresponding EDS mapping (middle) and EDS elemental analysis (right) of Au NPs on ITO substrate.

2.3.5 Transmission Electron Microscopy

In an SEM, secondary electrons are collected from scattering for imaging purpose. Transmission electron microscopy (TEM), which uses transmitted electrons through ultrathin films to generate images, is one of the most widely used imaging tools for atomic scale characterizations. The accelerating voltage of the incident electron beam in a TEM is typically 200-300 kV with the chamber pressure lower than 10^{-7} Pa. The high energy electrons are able to pass through the thin film sample and are focused onto a phosphor screen.¹⁶ Figure 2.10 shows the simplified schematic cross-sections configuration of a TEM instrument. As shown in the figure, there are three types of lenses that compose the key part of TEM: 1) condenser lenses (CL1 and CL2) centralized and concentrate the electron beam; 2) the objective lens (OL) focuses the electron beam to the sample; 3) the projector lens expands the electrons to the phosphor screen for imaging.¹⁷ The sample preparation process in TEM is normally a key factor for good images. NPs are usually ultrasonicated in acetone and drop casted on to the TEM grid. Sometimes a focused ion beam (FIB) technique is used to prepare site-specific electron transparent lamella for TEM analysis. Figure 2.11 shows the TEM images of Au@Pt NPs prepared by FIB technique in low and high magnifications.

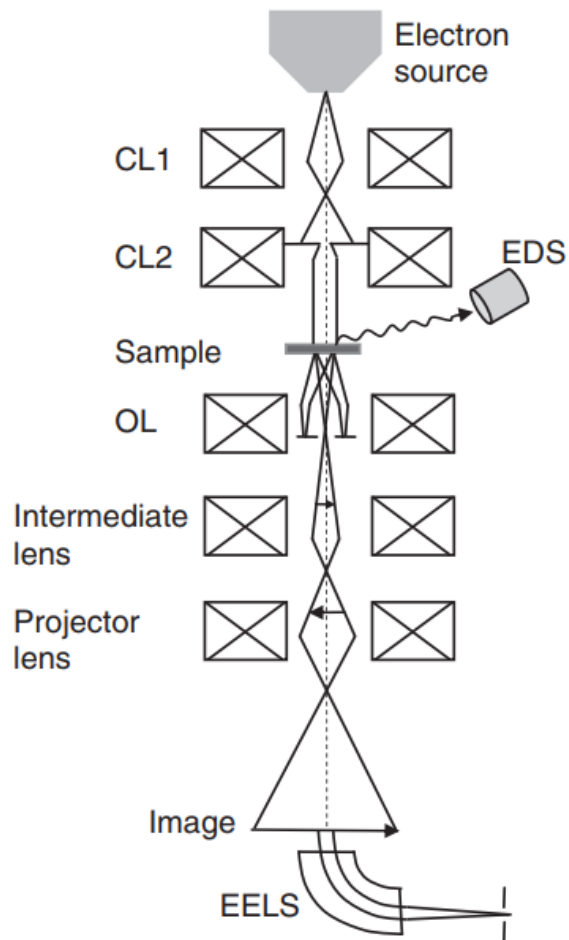


Figure 2.10: Simplified schematic cross-sections configuration of a TEM instrument. (Reproduced with permission from Reference 17.)

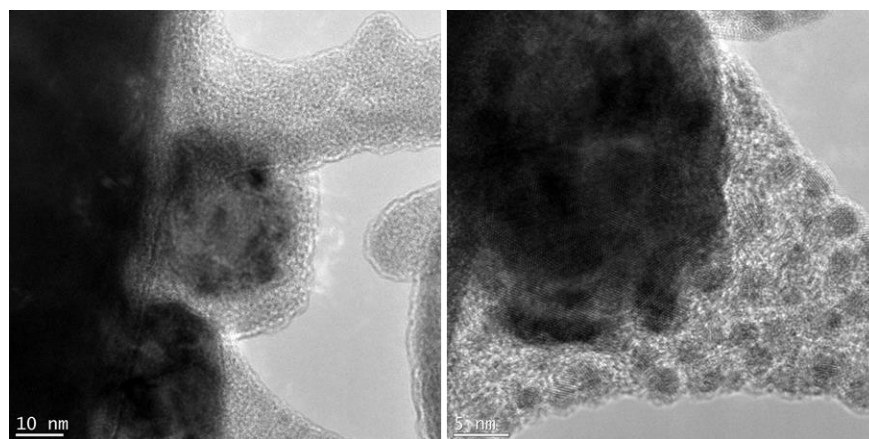


Figure 2.11: TEM images of Au@Pt NPs in low (left) and high (right) magnifications.

2.3.6 UV-Vis Absorption Spectroscopy

Ultraviolet–visible (UV-Vis) absorption spectroscopy measures the extinction of light when passes through a sample and is used widely for both qualitative and quantitative analysis. Absorption of ultraviolet and visible radiation is associated with excitation of electrons from lower to higher energy levels. Since only light with the precise amount of energy between the two energy levels will be absorbed, this technique is commonly used for sample characterizations. Electron excitations can happen under different mechanisms. For example, transition metal complexes promote d electrons in the lower energy level to the higher energy level upon light absorption; conjugated organic molecules absorb via π to π^* orbital transitions; semiconductor materials excite electrons from valence band to conduction band upon light absorption. Based on Beer-Lambert's Law, the absorbance is proportional to the concentration of a solution, thus UV-Vis spectroscopy can be used to quantitatively determine the concentration of a substance. Beer-Lambert's Law is expressed as $A = \epsilon bc$, where A is the absorbance, ϵ is the molar absorption coefficient, b is the optical path length and c is the concentration of solution.¹⁸

A typical UV-Vis spectrometer consists of a light source, a monochromator which splits light into different wavelengths, a sample holder and a photo detector, as shown in Figure 2.12. The absorbance is plotted as function of the incident light wavelength for a UV-Vis spectrum. Figure 2.13 shows a UV-Vis spectrum of a ~100 nm Au NPs sample on ITO substrate.

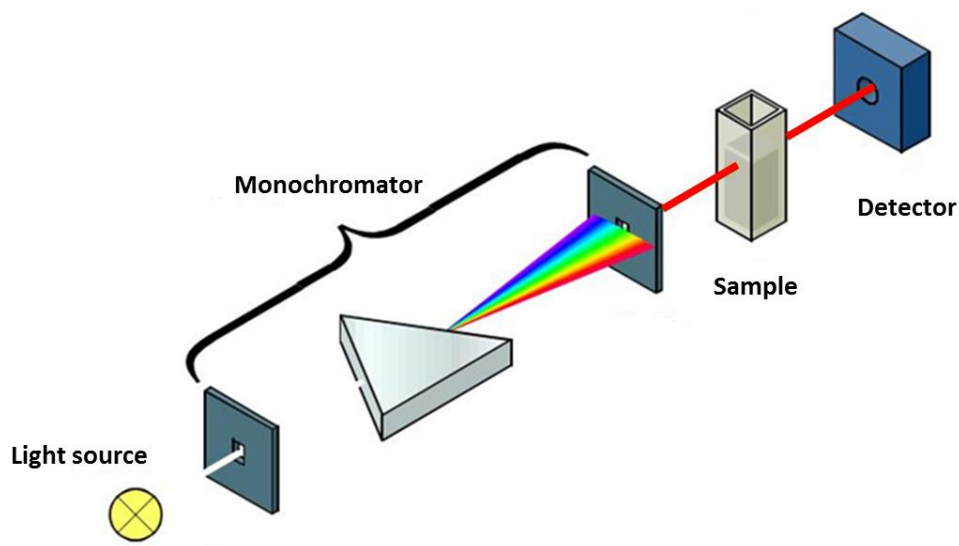


Figure 2.12: Schematic diagram of UV-Vis spectrometer.

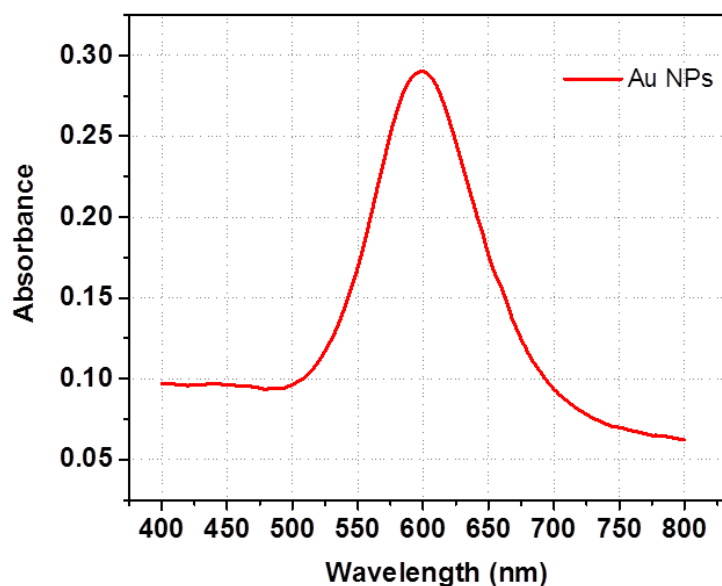


Figure 2.13: UV-Vis spectrum of ~100 nm Au NPs on ITO substrate.

2.3.7 Scanning Photoelectrochemical Microscopy

In order to rapidly discover new materials suitable for efficient solar water splitting, especially for fast screening of multiple compositions of two or three different components, scanning photoelectrochemical microscopy (SPECM) has been developed. SPECM is built based

on scanning electrochemical microscopy (SECM), which is an electroanalytical scanning probe technique with the function of imaging local reactivity and substrate topography with an ultrahigh resolution.¹⁹ In SECM technique, a small scale electrode (normally an ultramicroelectrode) is scanned across a substrate immersed in electrolyte solution. Current from both the tip and the substrate could be recorded simultaneously.²⁰

Unlike SECM, the tip on an SPECM is replaced by a small scale optical fiber, the position of which is controlled by an XYZ positioner.²¹ Once the position of the optical fiber approaches the substrate surface, it will only illuminate an area comparable to the size of the optical fiber. By controlling the X and Y position of the optical fiber, one can easily illuminate the selected area. Figure 2.14 shows the schematic diagram of a typical SPECM system. Different compositions of photoactive materials are prepared by a picoliter dispenser on a fluorine doped tin oxide (FTO) or Ti substrate. The substrate is immersed in proper electrolyte and then subject to optical fiber illumination, while the current of the substrate is recorded. When the non-photoactive substrate is illuminated, water oxidation reaction is unable to occur, so non-faradaic background current is detected. Once the optical fiber is moved to the top of photoactive species, electron and hole pairs are generated and water oxidation is carried out, thus oxidation current can be recorded by the potentiostat which represents the water oxidation current for a specific sample spot. By comparing the water oxidation current of all sample spots, the most efficient composition for water splitting could be determined. The SPECM technique is able to screen up to one hundred sample spots in less than 20 min which significantly shortens the time of finding new photoactive materials for solar water splitting.

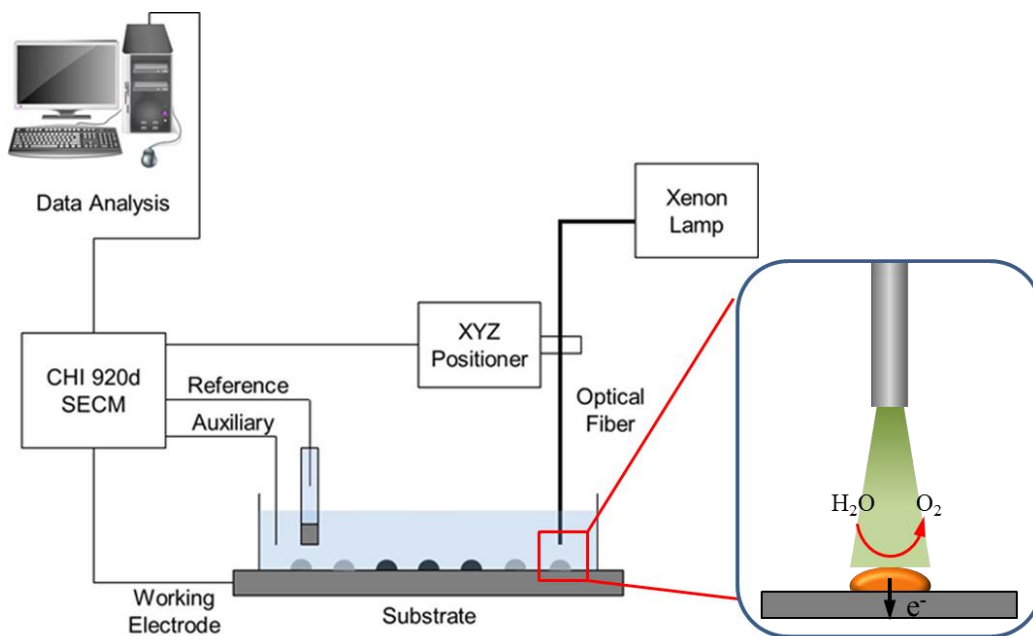


Figure 2.14: Schematic diagram of the SPECIM system.

2.3.8 Photoelectrochemical Characterization

To study the photoactivity of a material, photoelectrochemical characterization is required. Photoelectrochemical characteristics of an electrode are studied in a three electrodes system with the target material as working electrode, a platinum wire as counter electrode and a reference electrode.²² An electrochemical workstation (CHI 760 bipotentiostat) is used to apply potential to the electrodes and record the current simultaneously. The studied material is normally coated onto a conducting substrate, such as ITO, FTO or Ti plate by spin coating or electrodeposition. As shown in the schematic diagram in Figure 2.15, the working electrode is irradiated by a simulated sunlight source (a 300 W xenon lamp source) under 1 sun irradiation (1000 W m^{-2}) at AM 1.5G conditions and I-V curve is recorded by the potentiostat. Since light dependent photoactivity of the materials need to be studied, the I-V curve is recorded in presence and in absence of the light source. Figure 2.16 shows the I-V curve of hematite and 3% Au doped hematite photoanodes in 0.1 M NaOH solution under 1 sun illumination and in dark

condition. The photoactivity of the electrode is evaluated by the onset potential and the photocurrent obtained at 1.23 V vs. RHE. A negative onset potential is preferred for a photoanode.

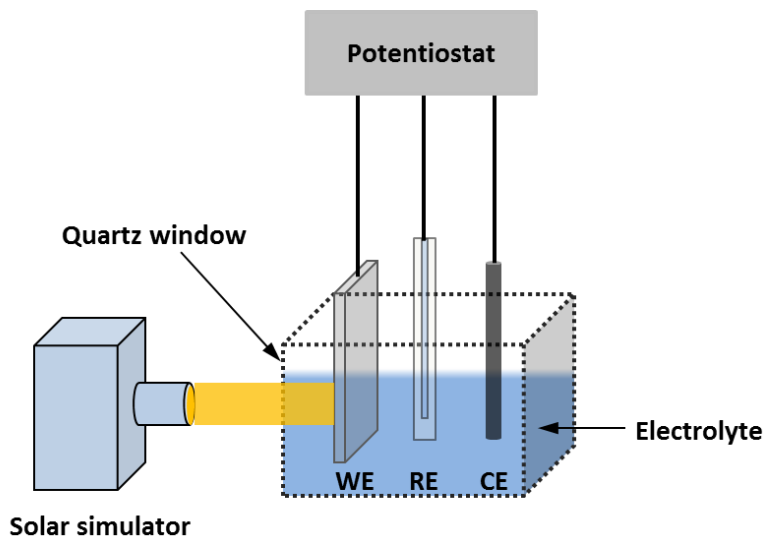


Figure 2.15: Schematic representation of a cell setup for PEC measurements.

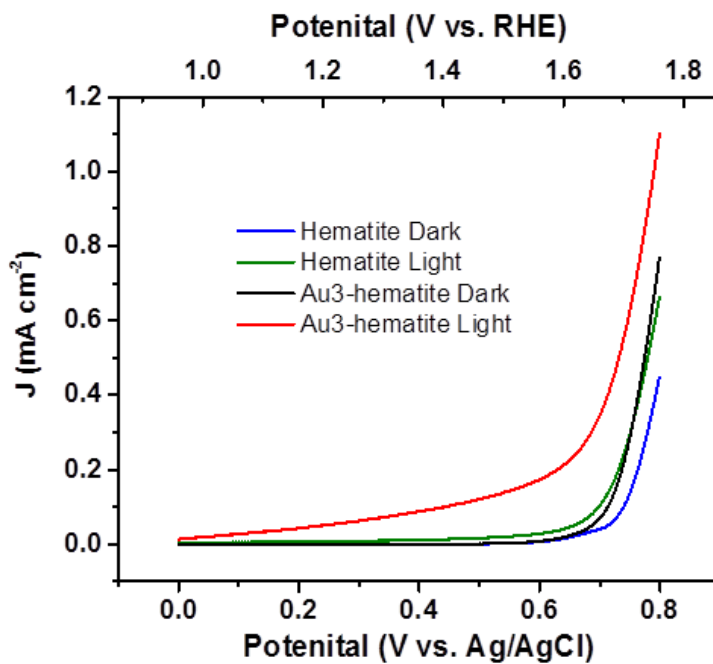


Figure 2.16: I-V curve of pristine and 3% Au doped hematite photoanode in 0.1 M NaOH under 1 sun illumination.

2.3.9 Mott-Schottky Analysis

The Mott-Schottky analysis is used to measure the changes that occur between the electrode surface and the bulk solution with different potential applied. A fixed-frequency AC potential excitation is applied to an electrochemical cell and the impedance of the working electrode interface is measured as a function of potential applied. The reciprocal of the square of capacitance ($1/C^2$) is plotted as a function of potential, described as the Mott-Schottky (M-S) plot.²³ The flat band potential of a semiconductor film in a liquid junction can be calculated from the Mott-Schottky equation:

$$\frac{1}{C_{sc}^2} = \frac{2}{e\epsilon_0\epsilon A^2 N_D} \left(E - E_{fb} - \frac{k_b T}{e} \right) \quad (3)$$

where C_{sc} is the space charge capacitance in $F\text{ cm}^{-2}$, e is the electronic charge in C, ϵ is the dielectric constant of the semiconductor, ϵ_0 is the permittivity of free space, N_D is the carrier density in cm^{-3} , E is the applied potential in V, E_{fb} is the flat band potential in V, k_b is the Boltzmann constant and T represents the temperature in K. As shown in Figure 2.17, the flat band potential can be obtained from the x-intercept of the extended linear region from the plot.²⁴ The Mott-Schottky analysis is widely used for study the electrode surfaces for semiconductor electrodes.

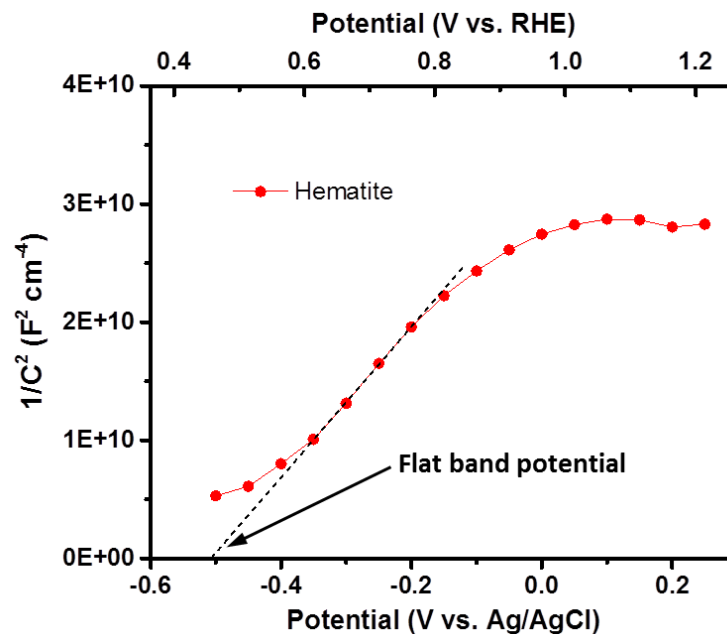


Figure 2.17: Mott-Schottky plot of thin film hematite photoanode.

2.3.10 Electrochemical Impedance Spectroscopy

Electrochemical impedance spectroscopy (EIS) is a characterization measurement built by applying a sinusoidal potential of different frequencies ($0.01\text{-}10^3$ Hz) to the system. The response of the system, output current, as a function of the perturbation frequency is measured. The response of the system is usually displayed in a Nyquist plot. Several important characteristics of the electrode such as series resistance (R_s), charge transfer resistance (R_{CT}), and space charge capacitance (C_s) could be obtained from fitting the plot to an equivalent circuit.²⁵ Figure 2.18 shows the Nyquist plot of spin coating prepared hematite photoanode under 1 sun irradiation and dark condition. It could be revealed that charge transfer resistance (radius of the fitted semicircle) decreases when the electrode is under light illumination, which indicates the increase of charge carriers in the film.

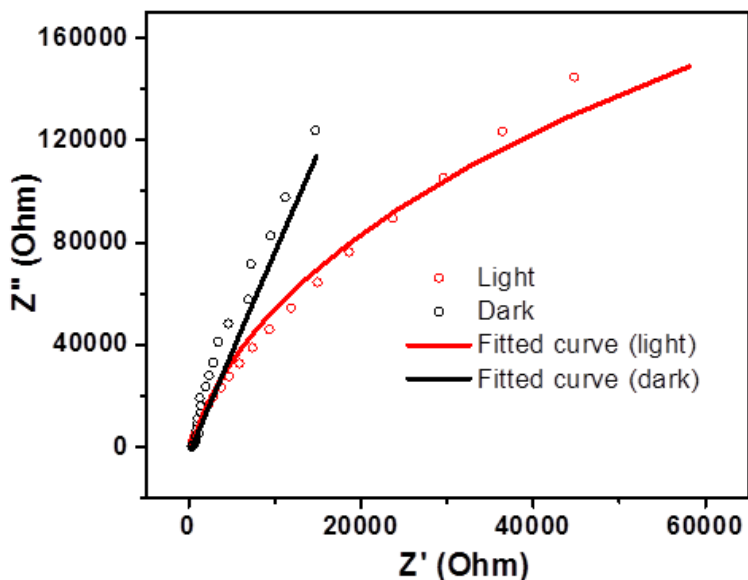


Figure 2.18: Nyquist plots of hematite thin film under dark and 1 sun irradiation condition

2.4 References

1. Basile, F.; Benito, P.; Fornasari, G.; Monti, M.; Scavetta, E.; Tonelli, D.; Vaccari, A., A Novel Electrochemical Route for the Catalytic Coating of Metallic Supports. In *Stud. Surf. Sci. Catal.*, Gaigneaux, E. M.; Devillers, M.; Hermans, S.; Jacobs, P. A.; Martens, J. A.; Ruiz, P., Eds. Elsevier: 2010; Vol. 175, pp 51-58.
2. Sobha Jayakrishnan, D., 5 - Electrodeposition: The Versatile Technique for Nanomaterials. In *Corrosion Protection and Control Using Nanomaterials*, Saji, V. S.; Cook, R., Eds. Woodhead Publishing: 2012; pp 86-125.
3. Liu, H.; Penner, R. M., Size-Selective Electrodeposition of Mesoscale Metal Particles in the Uncoupled Limit. *J. Phys. Chem. B* **2000**, *104*, 9131-9139.
4. Shan, Z.; Clayton, D.; Pan, S.; Archana, P. S.; Gupta, A., Visible Light Driven Photoelectrochemical Properties of Ti@TiO₂ Nanowire Electrodes Sensitized with Core-Shell Ag@Ag₂S Nanoparticles. *J. Phys. Chem. B* **2014**, *118*, 14037-14046.
5. Ma, Y.; Highsmith, A. L.; Hill, C. M.; Pan, S., Dark-Field Scattering Spectroelectrochemistry Analysis of Hydrazine Oxidation at Au Nanoparticle-Modified Transparent Electrodes. *J. Phys. Chem. C* **2018**, *122*, 18603-18614.
6. Xu, C.; Geng, H.; Bennett, R.; Clayton, D. A.; Pan, S., Ti@TiO₂ Nanowire Electrode with Polydisperse Gold Nanoparticles for Electrogenerated Chemiluminescence and Surface Enhanced Raman Spectroelectrochemistry. *J. Phys. Chem. C* **2013**, *117*, 1849-1856.
7. Stevenson, J. T. M.; Gundlach, A. M., The Application of Photolithography to the Fabrication of Microcircuits. *Journal of Physics E: Scientific Instruments* **1986**, *19*, 654-667.

8. Giannuzzi, L. A.; Stevie, F. A., A Review of Focused Ion Beam Milling Techniques for Tem Specimen Preparation. *Micron* **1999**, *30*, 197-204.
9. Donnelly, V. M.; Kornblit, A., Plasma Etching: Yesterday, Today, and Tomorrow. *J. Vac. Sci. Technol. A* **2013**, *31*, 050825.
10. Steinert, C. P.; Goutier, I.; Gutmann, O.; Sandmaier, H.; Messner, S.; Daub, M.; Heij, B. d.; Zengerle, R. In *An Improved 24 Channel Picoliter Dispenser Based on Direct Liquid Displacement*, TRANSDUCERS '03. 12th International Conference on Solid-State Sensors, Actuators and Microsystems. Digest of Technical Papers (Cat. No.03TH8664), 8-12 June 2003; 2003; pp 376-379 vol.1.
11. Bałczewski, P.; Kudelska, W.; Bodzioch, A., 4.12 - 1,3-Dithioles. In *Comprehensive Heterocyclic Chemistry Iii*, Katritzky, A. R.; Ramsden, C. A.; Scriven, E. F. V.; Taylor, R. J. K., Eds. Elsevier: Oxford, 2008; pp 955-1090.
12. Valero Vidal, C.; Igual Muñoz, A., 9 - Influence of Protein Adsorption on Corrosion of Biomedical Alloys. In *Bio-Tribocorrosion in Biomaterials and Medical Implants*, Yan, Y., Ed. Woodhead Publishing: 2013; pp 187-219.
13. Hanson, K. M.; Pappas, T. J.; Holland, L. A., Electrochemical Detection in Capillary Electrophoresis. In *Comprehensive Analytical Chemistry*, Marina, M. L.; Ros, A.; Valcree, M., Eds. Elsevier: 2005; Vol. 45, pp 413-440.
14. Ueno, H.; Nishikawa, S.; Iino, R.; Tabata, K. V.; Sakakihara, S.; Yanagida, T.; Noji, H., Simple Dark-Field Microscopy with Nanometer Spatial Precision and Microsecond Temporal Resolution. *Biophys. J.* **2010**, *98*, 2014-2023.
15. Zhou, W.; Wang, Z. L., *Scanning Microscopy for Nanotechnology. Techniques and Applications*, 2007, p 1-522.
16. Williams, D. B.; Carter, C. B., The Transmission Electron Microscope. In *Transmission Electron Microscopy: A Textbook for Materials Science*, Williams, D. B.; Carter, C. B., Eds. Springer US: Boston, MA, 1996; pp 3-17.
17. Bell, D. C.; Erdman, N., Introduction to the Theory and Advantages of Low Voltage Electron Microscopy. In *Low Voltage Electron Microscopy*, 2012.
18. Tissue, B. M., Ultraviolet and Visible Absorption Spectroscopy. In *Characterization of Materials*, Kaufmann, E. N., Ed. 2012.
19. Bard, A. J.; Fan, F. R. F.; Kwak, J.; Lev, O., Scanning Electrochemical Microscopy. Introduction and Principles. *Anal. Chem.* **1989**, *61*, 132-138.
20. Polcari, D.; Dauphin-Ducharme, P.; Mauzeroll, J., Scanning Electrochemical Microscopy: A Comprehensive Review of Experimental Parameters from 1989 to 2015. *Chem. Rev.* **2016**, *116*, 13234-13278.

21. Lee, J.; Ye, H.; Pan, S.; Bard, A. J., Screening of Photocatalysts by Scanning Electrochemical Microscopy. *Anal. Chem.* **2008**, *80*, 7445-7450.
22. Riha, S. C.; Fredrick, S. J.; Sambur, J. B.; Liu, Y.; Prieto, A. L.; Parkinson, B. A., Photoelectrochemical Characterization of Nanocrystalline Thin-Film Cu₂ZnSnS₄ Photocathodes. *ACS Appl. Mater. Interfaces* **2011**, *3*, 58-66.
23. Bard, A.; Faulkner, L., *Electrochemical Methods: Fundamentals and Applications*; John Wiley & Sons, Inc, 2001.
24. Gelderman, K.; Lee, L.; Donne, S. W., Flat-Band Potential of a Semiconductor: Using the Mott–Schottky Equation. *J. Chem. Educ.* **2007**, *84*, 685.
25. Chang, B.-Y.; Park, S.-M., Electrochemical Impedance Spectroscopy. *Annu. Rev. Anal. Chem.* **2010**, *3*, 207-229.

CHAPTER 3

DARK-FIELD SCATTERING SPECTROELECTROCHEMISTRY ANALYSIS OF HYDRAZINE OXIDATION AT GOLD NANOPARTICLES-MODIFIED TRANSPARENT ELECTRODES

Reproduced in part with permission from [Yanxiao Ma, Alton L. Highsmith, Caleb M. Hill, and Shanlin Pan, *The Journal of Physical Chemistry C* 2018, 122, 18603-18614] Copyright [2018] American Chemical Society.

3.1 Abstract

Gold nanoparticles (NPs) have interesting optical properties, such as local field enhancement for improving light absorption and Raman scattering cross-section of an organic chromophore, and catalytic properties of improving the kinetics of redox reactions involved in clean energy transformations. Real-time electrochemical measurements of catalytic Au NPs would help resolve their local structure-function relationship, which can further provide insights into developing an optimal catalytic condition. It is extremely challenging to resolve electrochemical events of electrocatalytic Au NPs at single particle level using conventional ensemble averaging methods. Here, we present a light scattering based spectroelectrochemistry analysis of single catalytic Au NPs at transparent planar electrode and ultramicroelectrode (UME) with combined methods of electrochemistry and dark field light scattering (DFS). Hydrazine oxidation reaction is used as a model system to characterize the catalytic characteristics of single Au NPs. Real-time light scattering response of Au NPs to surface adsorbates, Au oxide

formation, double layer charging, and nitrogen bubble formation upon hydrazine oxidation are investigated for both ensemble and single Au NPs. Such light scattering response to catalytic hydrazine oxidation at single Au NPs is highly sensitive to Au NP sizes. DFS study of single Au NPs shows a minor decrease in light scattering signal in the low overpotential region because of the double layer charging in the absence of hydrazine, and the surface adsorbates N_2H_3 in the presence of hydrazine. Significant decrease in DFS signal of Au NPs upon Au oxidation in the high overpotential region can be obtained in the absence of hydrazine. Such oxide-induced light scattering signal loss effect can be weakened in the presence of hydrazine and completely eliminated in the presence of > 50 mM hydrazine. Strong light scattering can be obtained due to nitrogen bubble formation on Au NP surface. Theoretical modeling with COMSOL Multiphysics is applied to support above conclusions.

3.2 Introduction

Nanostructured materials of metal, semiconductor, and insulators with various structural forms such as nanorods, nanowires, nanosheets, and nanocomposites made of these structural forms have been studied in the past decades. Some of these nanomaterials show interesting physical and chemical properties which otherwise cannot be obtained with their bulk counterparts.¹ For example, Pt and Pt alloy NPs enable fast kinetics of chemical fuel oxidation in fuel cells.² Au NPs have been applied to water gas shift reaction for hydrogen production,³ the production of methyl glycolate⁴ and catalytic oxidation of fuels.⁵ However, producing reproducible and stable catalytic efficient NPs are quite challenging because of their high sensitivity to shape, size and surface capping ligands. Aggregation and corrosion effects on their surface under harsh conditions may also prevent their broad applications. In addition, their surface chemistry and reaction mechanism are often unknown and technically extremely

challenging to quantify using conventional bulk ensemble averaging techniques.⁶ Therefore, new analytical methods need to be developed to study local catalytic activities and structure-functionality relationship at a single NP level with high spectral and spatial resolution. Many efforts have been made recently to detect single NPs and study redox reaction mechanisms on their surface. For example, single Pt NP detection with the collision method was reported by Bard et al.⁷⁻⁸ Such a collision-based particle analyzer can detect individual NP collision events based on their superior catalytic activity such as proton reduction over a non-catalytic carbon UME. Kwon et al.⁹ discovered the transient current of Pt NPs collision on Ni UME turned from staircase to blip with the change of potential applied. In this study, Pt NPs with an average size of 3.8 nm in diameter were used to catalyze hydrazine oxidation reaction on Ni surface. Although these collision methods can detect and count single NPs electrochemically, the particle size and shape information cannot be detected simultaneously and detailed surface chemistry and reaction mechanism of individual NPs cannot be resolved.

Another approach to studying the electrochemical properties of single NPs is to immobilize single NPs on a UME. Chen and Kucernak¹⁰⁻¹¹ developed a method to electrochemically deposit single Pt NPs onto a carbon UME. The surface area of the carbon UME is 1 nm² which only allowed one nucleation to form. They further analyzed the electrocatalytic properties of the single NP by proton reduction reaction. Single Au NPs were electrostatically adsorbed on a Pt nanoelectrode by Sun et al.¹² This study suggested that the energy required to achieve efficient oxidation of the Au NPs increased as the size of the NP decreased. Macpherson et al.¹³ fixed Au NPs onto a carbon nanotube UME for mercury ion sensing. Surface coverage, particle size, and shape of Au NPs and their effect on quantitative analysis of mercury ion were studied in their work. Detailed particle size and shape information

and their correlation to electrochemical performance can be studied with such surface attachment configurations of single NPs.

Besides electrochemical detection of single NPs, combined optical and electrochemical methods¹⁴ have been recently developed for understanding the electrochemistry of single NPs. Tao and coworkers¹⁵⁻¹⁶ demonstrated a plasmonic-based electrochemical current imaging method to measure the zeta potentials and surface charges as well as study the electrocatalytic properties of single nanoparticles. By reducing the protons to hydrogen, the refractive index near the electrode surface was decreased, which changes the surface plasmon resonance and allow one to image the local redox current on platinum nanoparticles. The Pan group recently has developed a dark-field scattering and photoluminescence spectroelectrochemical technique to track single silver NPs deposited on ITO substrate.¹⁷⁻¹⁸ The scattered light intensity was analyzed for each NP in a $\sim 100 \mu\text{m} \times 100 \mu\text{m}$ area. Particle size distribution was determined through the scattering intensities and compared with SEM images. Our group also demonstrated the observation of local redox events at individual Au NPs using electrogenerated chemiluminescence (ECL) microscopy.¹⁹ ECL at individual Au NPs was found to linearly increase with the increase of particle size under $1 \mu\text{m}$ because of the spherical mass transfer profile of redox species at an NP electrode. More recently, I was able to achieve in-situ growth of single Au NP with a diameter as low as 80 nm at the tip of a tungsten wire by DFS microscopy.²⁰ A significant increase of ECL intensity was obtained by increasing the size of Au NPs. Single molecule fluorescence on single NPs is also a powerful technique to image single NPs. Xu et al.²¹ developed a single molecule fluorescence imaging routine to help map the catalytic activity distribution. Single NPs were immobilized on a glass surface that can convert a non-fluorescent reactant to a fluorescent product. This method provided information on the

catalytic activity and reaction kinetics of different NPs. Tessier, Kanoufi, and coworkers²² have developed a DF scattering-based 3D holographic microscopy technique to study Ag NP oxidation reaction in different electrolytes. In this system, they assumed a one-to-one relationship between electrochemical and optical signatures. This technique can be easily coupled with spectroscopic detection and characterization of single NP.

Here, a study of Au NPs is presented using optically transparent planar electrode and UME to understand the electrocatalytic hydrazine oxidation at single Au NP levels with combined methods of electrochemistry and DFS microscopy. Theoretical modeling with both Mie theory and COMSOL Multiphysics are used to qualitatively understand our experimental results. The UME technique and spectroelectrochemistry imaging methods provide a unique capability to understand redox activities at the nanometer scale.

3.3 Experimental

3.3.1 Reagents and Materials

HAuCl₄ (30% wt. in dilute HCl) and hydrazine (35% wt. in water) were purchased from Sigma-Aldrich. Phosphate buffer solution (PBS) (pH = 7.3) was prepared from KH₂PO₄ (Acros Organics) and K₂HPO₄ (Fisher Scientific International, Inc.). All chemicals and solvents were purchased and used as received without any further purification. ITO coated glass (< 15 ohms/sq.) was purchased from Colorado Concept Coatings, LLC. ITO UMEs were fabricated in Micro-Fabrication Facility of The University of Alabama. Detailed fabrication procedure is described below. SEM images were taken from JOEL 7000 SEM in Central Analytical Facility of The University of Alabama. The electrochemical measurements were performed by CH Instruments 760C bipotentiostat.

3.3.2 ITO UME Fabrication

Figure 3.1 shows a schematic of ITO UME fabrication procedures. Prior to patterning its surface with photoresist, a 20 mm × 20 mm (in square) ITO coated glass slide was sequentially sonicated in 25 g/L ethanol solution of NaOH, DI water, ethanol, DI water and was then treated with UV-O₃ (UV/Ozone procleaner, Bioforce nanosciences) after drying under a stream of N₂ gas. The cleaned ITO glass was then spin coated with S1818 photoresist followed by UV light exposure in a Suss Microtec MA-6 mask aligner. After development, the eight-patterned ITO sites covered with photoresist remained. Then, the sample was ion milled to remove the intermediate ITO in order to yield eight ITO electrodes electrically isolated from each other. Then the photoresist was stripped from the substrate by sonicating in acetone and isopropanol, respectively. Finally, a second photolithography step was utilized to expose tiny holes (5 and 10 μm in diameter) followed by development to form transparent ITO UME. Dark-field microscopy and SEM were used to characterize the fabrication of ITO UME.

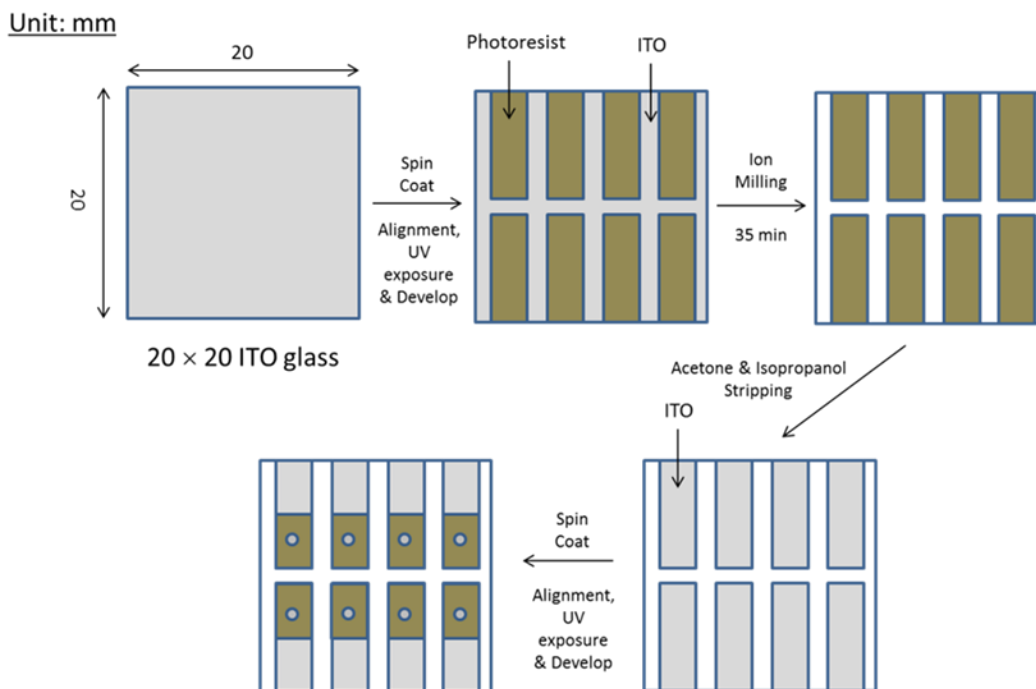


Figure 3.1: Schematic diagram of ITO UME fabrication

3.3.3 Au NPs Modification

Planar ITO glass and ITO UME modified with Au NPs can be formed via electrodeposition of Au NPs before or after patterning the ITO surface. The electrodeposition was carried out with a three-electrode system including platinum wire as a counter electrode, planar ITO or ITO UME as a working electrode and Ag/AgCl as a reference electrode. 0.5 mM HAuCl₄ in 0.1 M NaCl solution was added to the electrochemical cell. Electrodeposition was performed by multistep potential deposition with different nucleation potential (-0.6, -0.5, -0.4, -0.3 and 0 V vs. Ag/AgCl) and with growth potential held at 0 V (vs. Ag/AgCl) for 300 s. The deposited Au NPs were further characterized by DFS and SEM. SEM analysis of samples was performed using a JEOL 7000 FE-SEM operating at a 20 keV accelerating voltage for planar ITO and 10 keV for ITO UME. Average particle size and distribution was calculated by free imaging processing and analysis software ImageJ available through the National Institutes of Health (NIH). Au deposition on ITO UME, however, does not provide similar NP size and coverage as planar ITO electrode. This has to do with the differences in the mass transfer profile of AuCl₄⁻ at UME and planar ITO electrode, and also the surface hydrophobicity of ITO UME which is obtained by ion-mill treatment of ITO involved in a photolithograph. Such surface cleaning technique may help improve the local conductivity of ITO and remove surface contaminants as it is broadly used in the fabrication of optoelectronic devices such as organic light emitting diodes (OLEDs).

3.3.4 Light Scattering Spectroelectrochemistry Study of Hydrazine Oxidation

Au modified ITO was vertically put into a home-built electrochemical cell with two quartz windows for laser light excitation and scattering. A THORLABS INC. 10 mW HRP050 632.8 nm laser or a 40 W halogen lamp was used as the light source. The electrochemical cell

was filled with 50 mM of PBS containing 1.0 M hydrazine. In-situ light scattering was detected by a photomultiplier tube (PMT) (R4220P, Hamamatsu) or a spectrometer with a liquid-nitrogen-cooled digital CCD spectroscopy system (Acton Spec-10:100B, Princeton Instruments, Trenton, NJ, USA) through a monochromator (Acton SP-2558, Princeton Instruments). A 5 mm (in diam.) graphite rod was used as counter electrode and Ag/AgCl (or a calibrated Ag QRE) as reference electrode while Au NP-modified ITO was used as working electrode. Both counter and reference electrodes were kept out of the laser excitation beam path to avoid interruption of laser intensity. The scattered laser intensity signal from the PMT was converted to an analog current signal and recorded along with working electrode current response with a CHI 760C potentiostat or a 1000C CHI multipotentiostat. Based on the cathode radiant sensitivity (10 mA/W at 633 nm) of the PMT, the power of the light collected could be obtained by the current responses.

3.3.5 Electrocatalytic Hydrazine Oxidation and DFS

A 1.0 M hydrazine solution was prepared in DI water for electrocatalytic experiments. ITO UME was used as working electrode. Pt wire and Ag wire served as a counter and a reference electrode, respectively. A droplet of hydrazine solution was deposited on the center of ITO UME with the counter and reference electrodes connected through a micro-positioner. CV was performed from -0.5 V to 0.5 V vs. Ag quasi-reference electrode (QRE) (from -0.5001 V to 0.4999 V vs. Ag/AgCl) at a scan rate of 0.1 V/s. The electrochemistry setup was combined with a confocal dark-field microscope (Olympus IX71) for combined spectroelectrochemistry study. The scattered light signal was collected by an electron multiplying charge coupled device ANDOR Technology iXon X3 EM-CCD camera using a 40 × objective (N.A. = 0.75). The exposure time of the EM-CCD camera was set to be 0.1 s. The EM-CCD camera for collecting

dark field scattering and potential scanning was triggered at the same time to collect data simultaneously.

3.4 Results and Discussion

3.4.1 Cyclic Voltammetry of Bare Au NPs in PBS and Hydrazine Oxidation at Planar Au NPs-ITO Electrodes

Au NPs were coated onto planar ITO using electrochemical multistep method deposition method. -0.6 V, -0.5 V, -0.4 V, -0.3 V, -0.2 V, -0.1 V and 0 V (vs. Ag/AgCl) were used as nucleation potentials and 0 V (vs. Ag/AgCl) was used as growth potential to optimize Au NPs size and coverage that could be detected by both SEM and DFS microscopy. Light scattering of individual <100 nm NPs can be optically resolved with the DFS technique, although the optical image spot size is limited by the optical diffraction limit. Au NPs grown at 0 V (vs. Ag/AgCl) nucleation potential can be detected by both SEM and DFS microscopy without further treatment. Typical light absorption spectra and SEM images of Au NPs deposited onto ITO electrodes are presented in Figure 3.2. Figure 3.3A shows a typical SEM image and statistical analysis of particle size distribution on an ITO surface. Au NPs with the size of 117 (+/-18) nm and density of 1.4×10^9 particles/cm² can be obtained by this electrochemical deposition method for spectroelectrochemistry study.

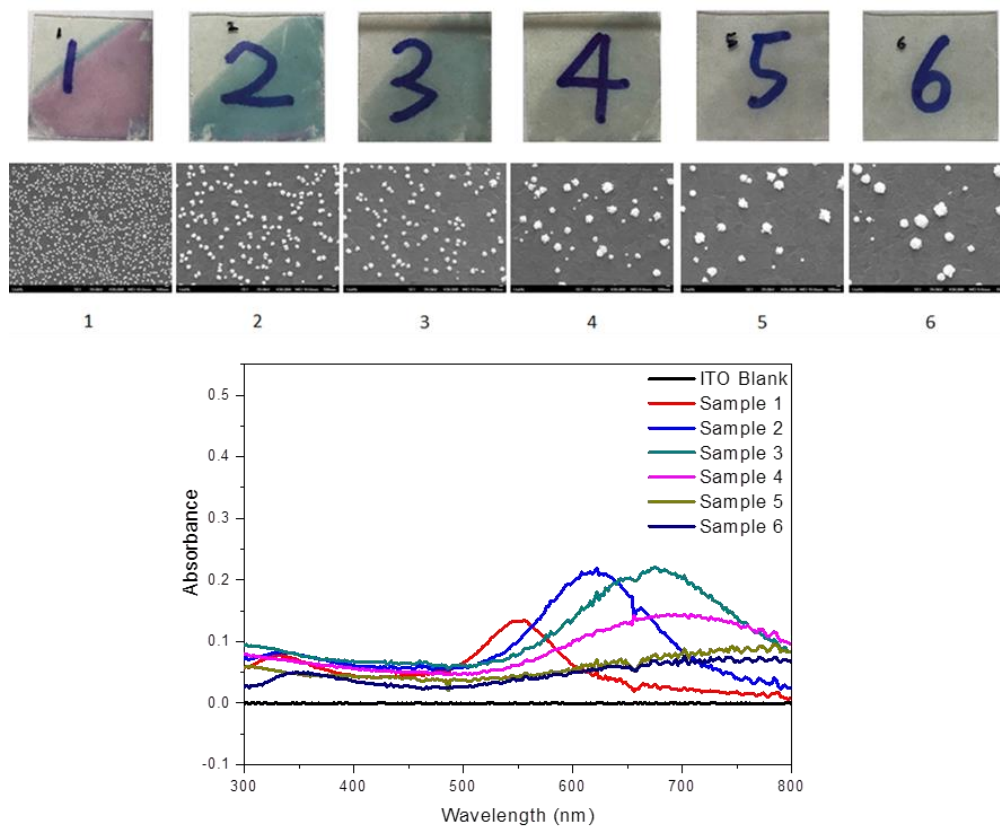


Figure 3.2: UV-Vis absorption spectra of Au NPs modified bare ITO with different coverage

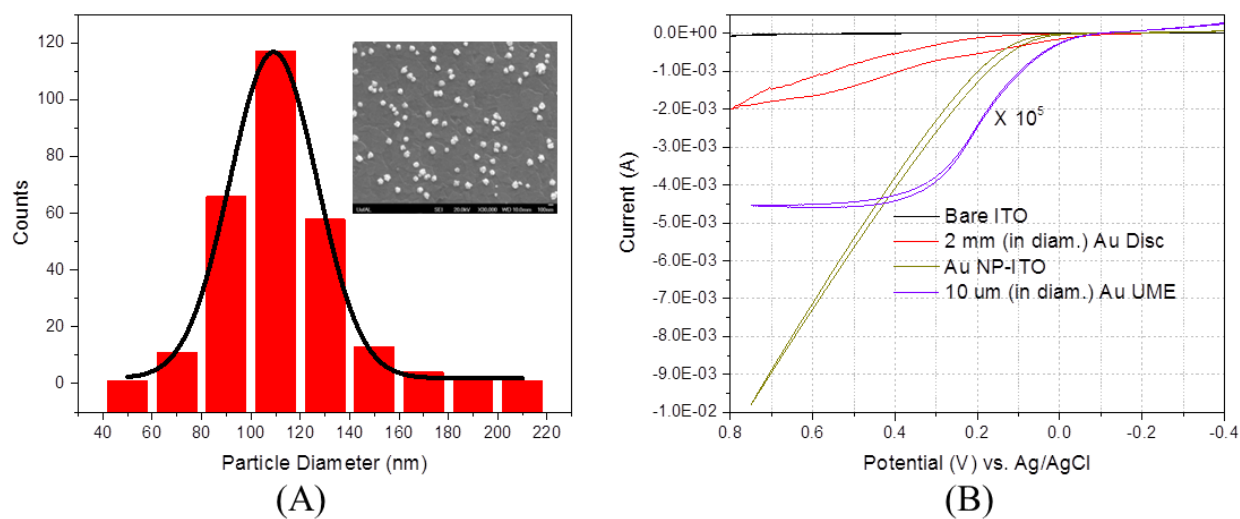
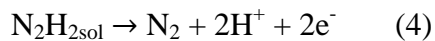


Figure 3.3: (A) SEM image and particle size distribution of Au NPs modified planar ITO electrode with average particle diameter of 117 (\pm 18) nm and particle coverage of $1.4 \times 10^9/\text{cm}^2$; (B) Cyclic voltammograms (CVs) of 1.0 M hydrazine oxidation at a planar bare ITO, 2.0 mm (in diam.) Au disc, 117 nm Au NPs modified ITO, and a 10 μm (in diam.) Au microelectrode.

Local redox reaction of Au NPs-modified ITO was tested with hydrazine as a model system. A 2 mm (in diam.) Au disc electrode and a 10 μm Au microelectrode was used to compare with the electrocatalytic oxidation of hydrazine by Au NPs. As shown in Figure 3.3B, significantly enhanced catalytic current is obtained in the presence of Au at Au NPs-ITO, Au disc electrode, and a microelectrode. In contrast, hydrazine oxidation is very sluggish on ITO as indicated by nearly zero oxidation current. Hydrazine oxidation is a well-known kinetically limited reaction, which is highly dependent on pH and involves multiple charge-transfer and surface adsorption/desorption reactions as shown in the followings:²³



The net reaction of hydrazine oxidation is given below



The entire oxidation has the rate-limiting step (3) for oxidation of adsorbed N_2H_3 product. Hydrazine oxidation is more favorable on Au surface than ITO because of the amine oxidation steps (2) and (4) can be catalyzed by Au, although the entire reaction is still kinetically slow and irreversible as evidenced by the slow increase in oxidation current accompanied with only two minor mass transfer limited peaks at 0.15 and 0.55 V (vs. Ag/AgCl) corresponding to reaction (2) and (4), respectively, at an Au disc electrode. There is a mass transfer limited current above 0.3

V vs. Ag/AgCl with an onset potential of 0 V at the Au microelectrode as shown in Figure 3.3B. There was no mass transfer limited oxidation current detected for Au NPs-ITO electrode in the presence of 1.0 M hydrazine because of rapid mass transfer to Au NPs and low surface coverage of Au NPs; the entire anodic current is simply limited by the slow kinetics of hydrazine oxidation at Au NPs.

3.4.2 Light Scattering Spectroelectrochemistry Response of Hydrazine Oxidation

To fully resolve the surface reactivity of hydrazine oxidation at Au NPs, light scattering and extinction properties of surface plasmon resonance of Au NPs were measured using the spectroelectrochemistry setup shown in the schematic of Figure 3.4. Scattered light was obtained by avoiding the direct light excitation beam and its reflection. A monochromatic light source such as a polarized laser or a white light source was used in this detection configuration from a home-built electrochemical cell in a three-electrode configuration. This allows us to collect light scattering intensity and cyclic voltammetry (CV) simultaneously.

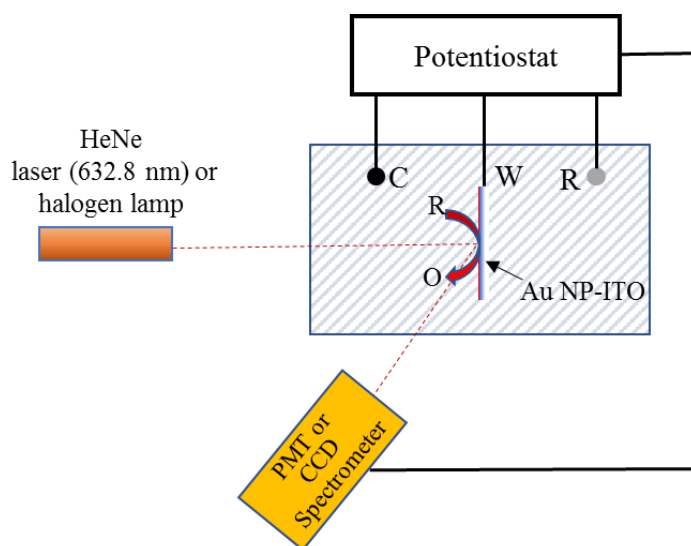


Figure 3.4: Schematic of experimental setup with a halogen lamp or a HeNe laser (632.8 nm) for probing the light scattering intensity and spectrum changes of Au NPs upon hydrazine oxidation and Au anodization.

Figure 3.5 shows CVs an Au NPs-modified ITO electrode in 50 mM PBS and responses of light scattering signal upon Au NP anodization. The maximum anodization potential was gradually increased from -0.05 to 1.5 V vs. Ag/AgCl to follow the reversibility of light scattering from Au NPs. The light scattering spectroelectrochemistry study shows that Au NPs can be anodized above 0.75 V accompanied by a decrease in light scattering. Light scattering decreases with the increase in the anodization potential until the electrode potential reaches the Au anodization peak current at 1.0 V. The light scattering decrease reaches 32.1% of the initial intensity above 1.0 V oxidation potential. The low-light scattering gold oxide product remains the same until the reduction of Au oxide at electrode potential below 0.5 V to fully regain the initial light scattering Au NP surface. Slow light scattering decrease can be obtained in the potential region less than 0.75 V in PBS because of double layer charging and decrease in surface state of Au NPs. In order to resolve the effects of hydrazine oxidation on the light scattering decrease by surface oxide formation, hydrazine concentration was gradually increased from 1 μ M to 100 mM in the 50 mM PBS. As shown in Figure 3.6, Au anodization is weakened by an increase in hydrazine concentration as shown by both CVs and laser scattering intensities. With 50 mM of hydrazine or above, the light scattering decrease upon Au anodization completely disappears. In comparison to light scattering response in PBS, oxidation of 100 mM hydrazine in the PBS provides only 1/7 of the light scattering decrease amplitude in the presence of hydrazine. Light scattering decreases in the electrode potential region less than 0.2 V with a decreasing amplitude of 5.8% of the initial intensity and reaches a plateau above 0.2 V. Scanning the electrode potential slower than 0.25 V/s or toward more positive potential will be more likely to produce nitrogen gas bubbles which will increase light scattering. The presence of hydrazine oxidation clearly prevents surface anodization of Au NPs while limiting the further decrease of

light scattering because of the fast mass transfer and surface catalytic reaction as shown in equation (1) - (4) at an Au NP surface. The only minor light scattering decrease upon hydrazine is attributed to the surface adsorption of N_2H_3 .

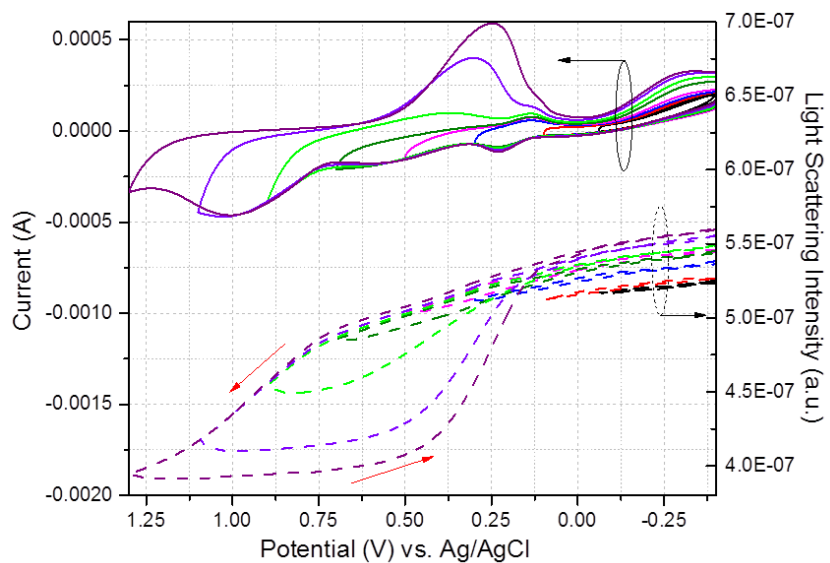


Figure 3.5: CVs (top) of a Au NPs-modified ITO electrode in 50 mM PBS with highest anodization potential gradually increased from -0.05 to 1.5 V vs. Ag/AgCl at a scan rate of 0.5 V/s while laser scattering responses (bottom) at 632.8 nm.

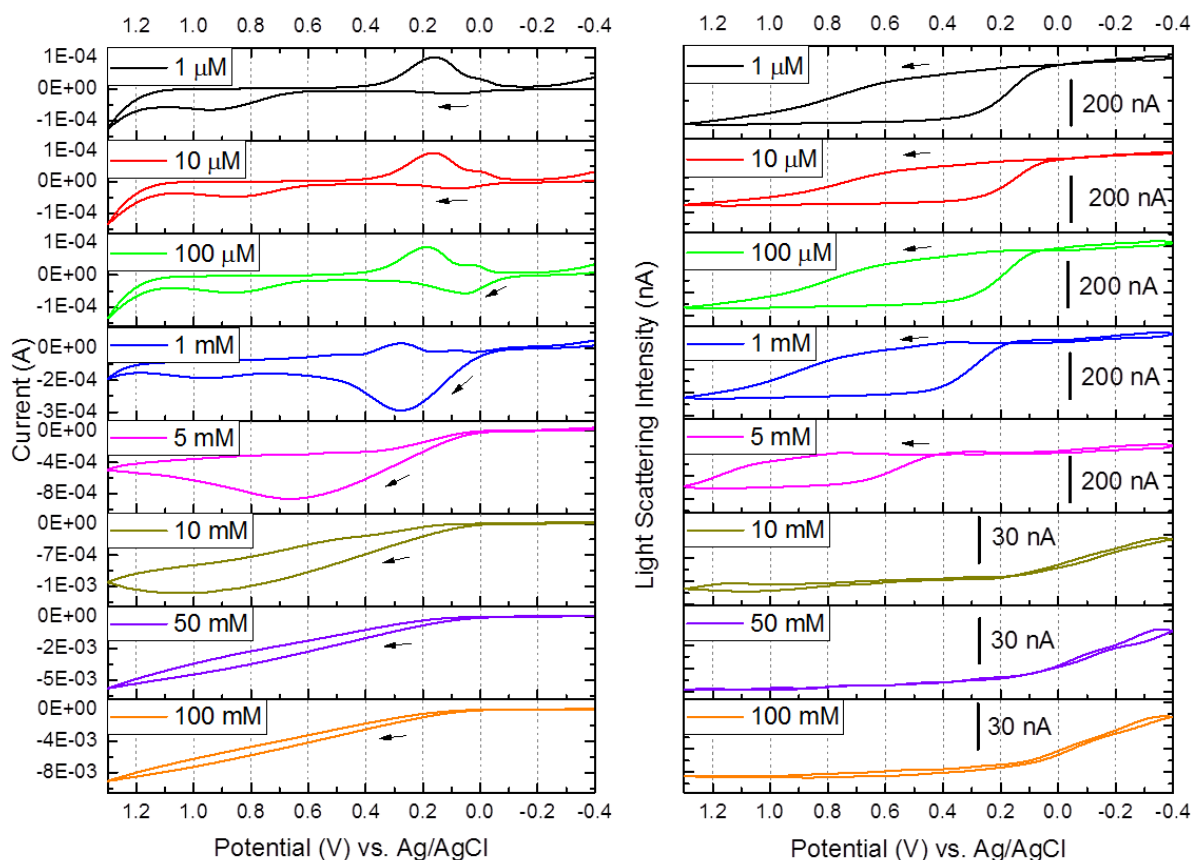


Figure 3.6: CVs (left) and laser scattering responses (right) of a Au NPs-modified ITO electrode in 50 mM PBS containing hydrazine concentration from 1 μM to 100 mM at a scan rate of 0.5 V/s. The arrows indicate scanning directions.

Scan rate dependences of the light scattering spectroelectrochemistry data are shown in Figure 3.7. This experiment was conducted in 1 M hydrazine with 50 mM PBS. Au NPs modified ITO served as a working electrode while graphite and Ag QRE were used as counter and reference electrodes, respectively. The same light scattering decrease is obtained at low oxidation potential region and not much change above the certain potential threshold, except the bursts of light scattering due to the formation of hydrogen bubbles. Many bubbles were detected at low scan rates of 0.1 and 0.05 V/s because of the total charges increase at a low scan rate during the entire CV scan period. With a low scan rate, the total time period is getting longer, thus the total charge transfer increases at a low scan rate. We conclude that the adsorption of

N_2H_3 on Au NP surface and presence of nitrogen gas molecules eliminate the formation of Au oxide, which would otherwise decrease the scattering of light. Once the adsorption and desorption of N_2H_3 reached a dynamic equilibrium, the scattering intensity was not further decreased or increased, although the mass transfer rate to/from the Au NP or current may increase with electrode potential. The only minor decrease and fluctuation in light intensity above 0.2 V are due to further kinetically limited oxidation and regeneration of $\text{N}_2\text{H}_{3\text{ads}}$ accompanied with molecular nitrogen formation. Further oxidation of $\text{N}_2\text{H}_{3\text{ads}}$ and $\text{N}_2\text{H}_{2\text{sol}}$ does not seem to have much effect on the light scattering intensity.

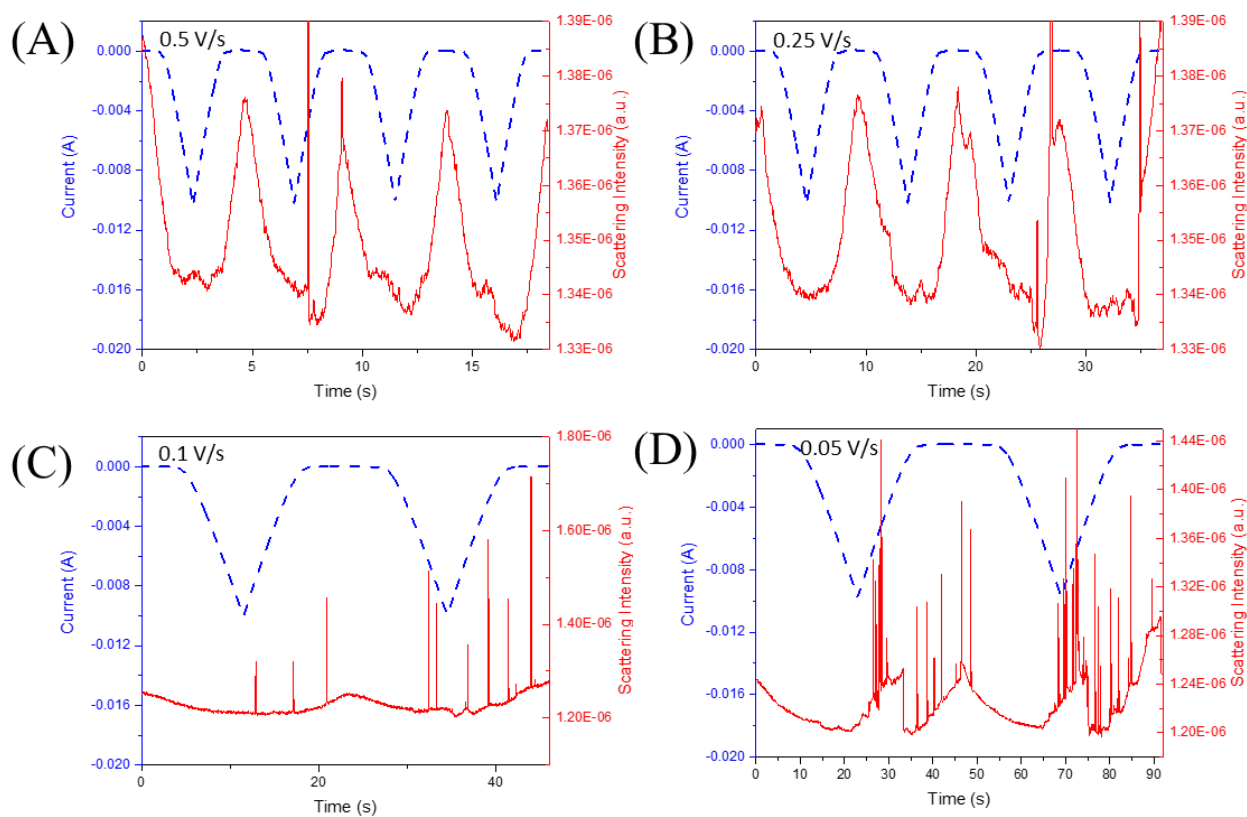


Figure 3.7: Time evolution of laser scattering intensity and current during linearly cycling the electrode potential from -0.4 V to 0.75 V and then back to -0.4 V (vs. Ag QRE) for four cycles at scan rate of 0.5 (A), 0.25 (B), 0.1 (C), and 0.05 (D) V/s. Light scattering intensity of panel A and B are plotted with a different scale from panel C and D.

Figure 3.8A shows the absorption and light scattering spectra of 117 (+/-18) nm Au NPs modified ITO glass. The redshift in scattering spectrum peak position from absorption peak position is attributed to light absorption of Au NPs, and the difference in scattering light collection geometries of absorption and scattering spectra and the heterogeneities in Au NP size and geometry. Typical response of light scattering spectrum of Au-ITO electrode upon hydrazine oxidation is shown in Figure 3.8B. Time evolution light scattering spectrum of the Au-NPs-ITO electrode and its intensity change (ΔI) at each wavelength upon oxidation of 1 M hydrazine in 50 mM of PBS is shown in this study. The total integrated intensity from 600-680 nm shows the most sensitivity to hydrazine oxidation, as shown in Figure 3.8B (i-iii), because of the light scattering cross-section is the highest in this wavelength region. Consistent with results illustrated in Figure 3.6-3.7, light scattering decreases and then reaches a plateau as the electrode potential was scanned from -0.4 to 0.75 V and then reverses back to -0.4 V. There is no spectroscopy peak shift obtained in this study because of the broad plasmon light scattering peaks. More precise particle size control and plasmon peak tuning would yield narrow light scattering peak in order to resolve wavelength dependence of the spectrum upon hydrazine oxidation.

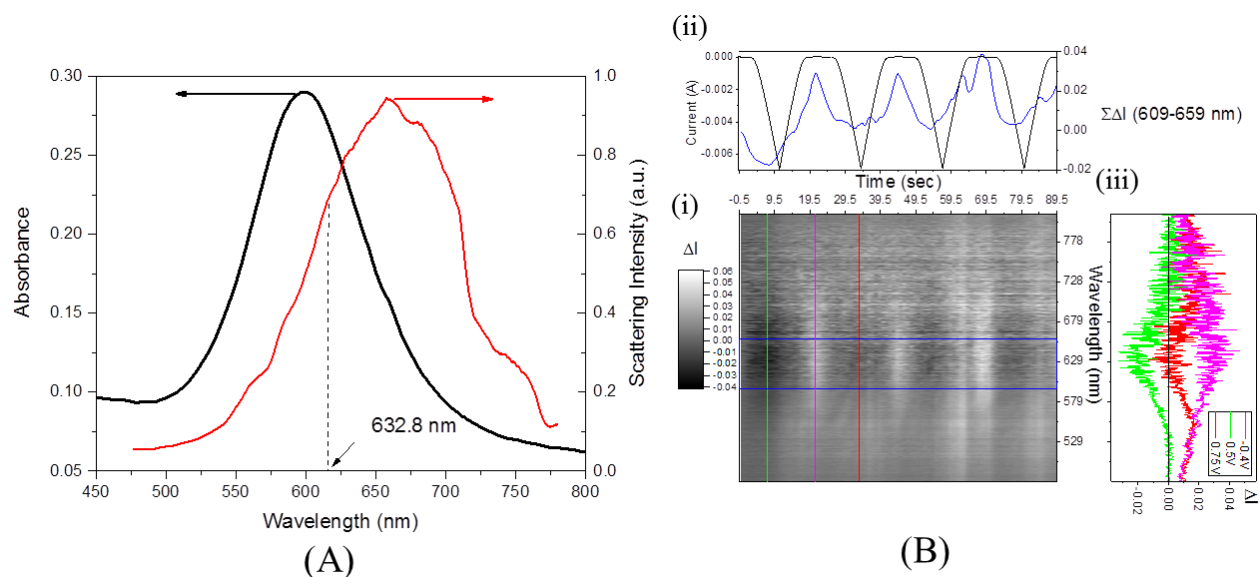


Figure 3.8: (A) Absorption spectrum of 117 (\pm 18) nm Au NPs modified ITO and light scattering spectrum of the same sample with spectrum collection geometry shown in panel A; (B) Time evolution light scattering intensity change (ΔI) at each wavelength upon oxidation of 1M hydrazine in 50 mM of PBS with electrode potential linearly cycled from -0.4 to 0.75 V and then back to -0.4 V (vs. Ag/AgCl) for four cycles at a scan rate of 0.1V/s. b is the current and ΔI sum from 609 to 659 nm trajectories corresponding to the CV, and c is ΔI spectra at electrode potentials of 0.5, -0.4, and then 0.75 V vs. Ag/AgCl. ΔI spectrum is obtained by subtracting the initial light scattering spectrum from all other spectra during hydrazine oxidation.

3.4.3 DFS-EC Spectroelectrochemistry Method to Resolve Hydrazine Oxidation at Single Au NPs on Planar ITO Electrodes

DFS of single plasmonic nanoparticle has been applied to understand how light scattering and resonance conditions respond to surface chemistry and electrochemical reactions.²⁴ For example, a blue shift in light scattering plasmon peak of the single gold nanorod, sphere, and trigonal prisms was obtained upon electron injection in KCl solution.²⁵ Plasmon peak red shift upon catalytic oxidation of H_2O_2 at single Au nanorods was also resolved. Such surface catalytic reaction and the presence of reducing redox species would prevent the formation of Au oxide upon oxidation as shown by Jing and coworkers²⁶. The redshift and light scattering intensity decrease can be also detected for individual Au nanorods²⁷⁻²⁸ and bulk film of Au NPs²⁹⁻³⁰ in

0.1M NaCl, because of i) double layer charging near the rest potential region, ii) anion adsorption region due to decrease in surface states at slightly higher electrode potential than rest potential, and iii) Au oxide surface. Although our electrodeposition method can potentially synthesize spherical Au NPs with a very narrow size distribution on a flat substrate, the rough surface and heterogeneities in local conductivities of ITO can only yield Au NPs with broad size distribution from tens of nm to a few hundred nm, as shown in Figure 3.3. To detect the local redox event correlation to particle size, single Au NP DFS spectroscopy is used to study light scattering response to hydrazine oxidation (Figure 3.9A). We hypothesize that DFS of individual Au NPs will respond to the applied electrode potential because of local redox reaction-induced activities (e.g., surface adsorption or reaction product, refractive index change, change in surface states, and double layer charging). DFS signal change is expected in response to the hydrazine oxidation current and potential because it is very sensitive particularly for Au NPs, which have surface plasmon resonance characteristics very sensitive to all above activities. Single Au NP DFS imaging method is expected to provide useful information about reaction mechanism at single particle level with both current and optical information with known particle size and shape. As shown in Figure 3.9B, individual Au NPs sparsely coated onto ITO planar surface can be obtained using our electrodeposition methods so that individual particles can be resolved using both DFS imaging (Figure 3.9C) and SEM (Figure 3.9B) in the presence of single plasmon resonance mode without complications of particle aggregation or plasmon coupling. This would help simplify the theoretical modeling of this spectroelectrochemical system.

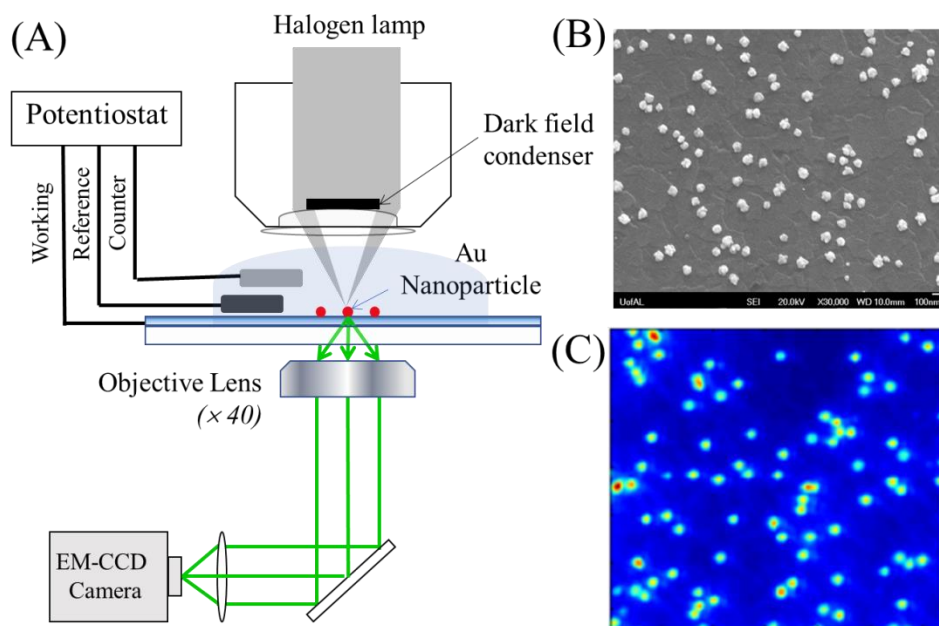


Figure 3.9: (A) Experimental schematic of dark field scattering spectroelectrochemistry (DFS-EC) setup for hydrazine oxidation at single Au NPs containing an electrochemical cell in a 3-electrode configuration and an EMCCD camera connected through an inverted optical microscope with a dark field condenser with top light illumination. (B) Typical SEM image of 176 (+/- 43) nm Au NPs electrodeposited onto an ITO working electrode and (C) DFS image showing a bright light scattering of Au NPs.

CV and DFS images were recorded at the same time to resolve DFS response of individual Au NPs. Figure 3.10 shows DFS-EC results of single Au NPs with their DFS light responses upon hydrazine oxidation. Electrode potential was scanned only toward 0.75 V to avoid Au anodization at NP surface. The inset of Figure 3.10A is a typical DFS image of single Au NPs. Statistical analysis DFS of single Au NPs and spatial distribution can be obtained with this method. The broad DFS signal distribution is attributed to the size distribution of Au NPs. DFS intensity increase with Au NP size due to its increase in light scattering cross-section in the visible light region, as shown by our previous study.¹⁷ Figure 3.10B shows DFS intensity decreases significantly upon hydrazine oxidation. To analyze how DFS light intensity decrease depends on electrode potential and particle size, we measured the initial DFS intensity I_0 and also its intensity decrease amplitude ΔI as shown in Figure 3.10C. We then plotted ΔI against initial

DFS intensity in Figure 3.10D to show that the DFS intensity decrease amplitude almost linearly increases with initial light intensity I_0 . Relative DFS decrease in $\Delta I/I_0$ does not show much variation. We also obtained only minor DFS decrease in its intensity upon forwarding potential scan and the minimum DFS intensity is located near the middle of the reversed segment of the potential, strongly suggesting DFS responded to the accumulated product of hydrazine oxidation. Light scattering decrease in the electrode potential window was not detected because of the sluggish oxidation of hydrazine at ITO surface. The DFS intensity decrease is consistent with the results in Figure 3.7-3.8 obtained with the bulk-averaging laser scattering method. Surface adsorption of anodized product N_2H_3 is mainly responsible for the DFS signal decrease. Such surface adsorption of anodized product N_2H_3 will weaken the oscillator strength of an Au NP to decrease its light scattering cross-section. We also hypothesize that oxidation of hydrazine produces nitrogen molecules that can either diffuse rapidly in water or be accumulated around Au NPs to form nitrogen bubbles, which can very likely increase light scattering should the bubble large and stable enough. All DFS response I/I_0 trajectories of > 150 NPs are extracted and plotted as a function time along with oxidation current in Figure 3.11. Each trajectory has a light intensity decrease upon hydrazine oxidation. This helps conclude that catalytic reaction at single Au NP sites is responsible for the bulk ensemble performance.

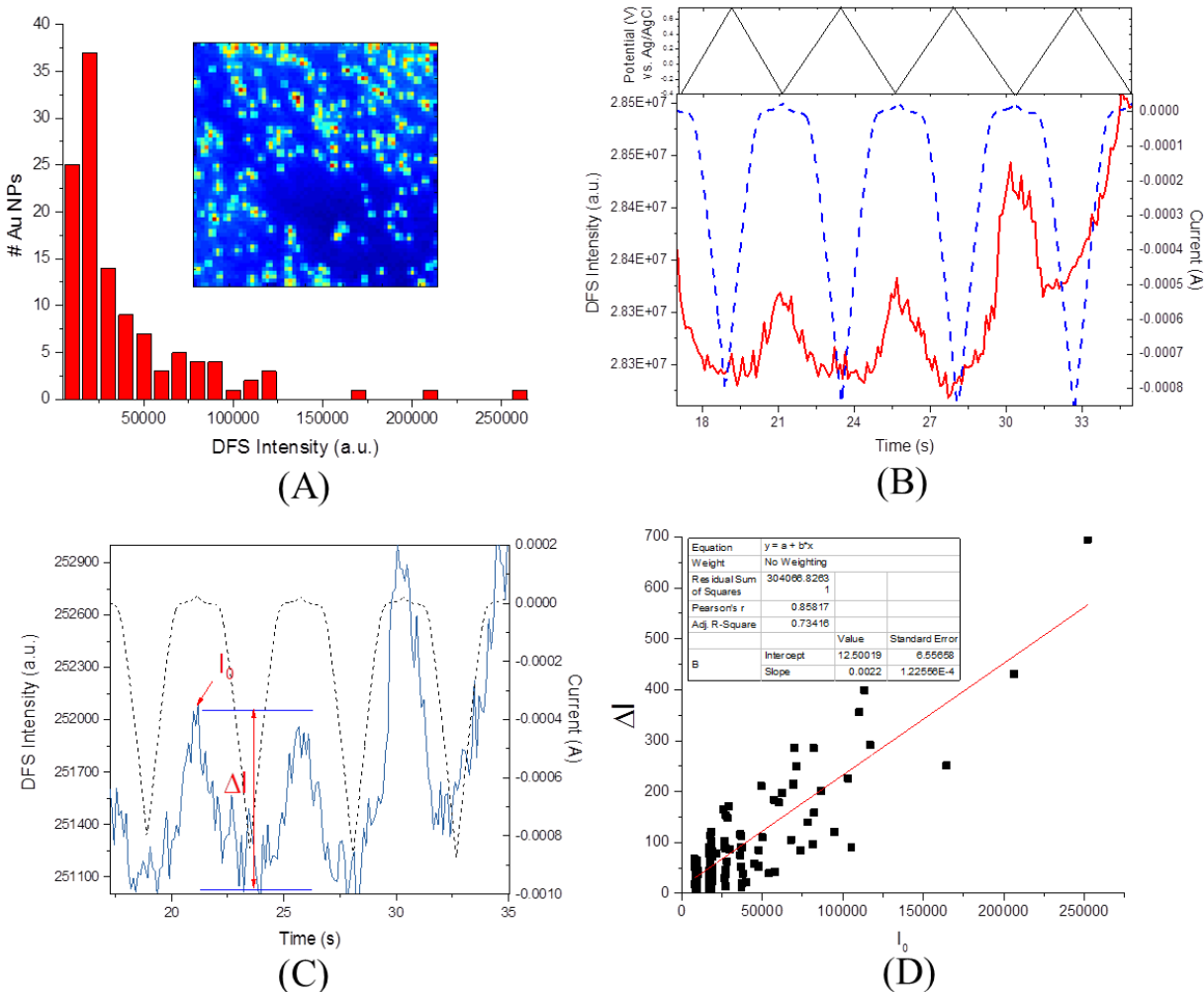


Figure 3.10: (A) statistical distribution of initial DFS intensities of single Au NPs and a typical DFS image collected with an EMCCD (inset); (B) summed DFS intensity and electrode current responses of > 150 Au NPs to electrode potential scanning from -0.4 V to 0.75 V then back to -0.4 V (vs. Ag Ag/AgCl) at a scan rate of 0.5 V/s for four cycles; (C) Typical DFS response profile of a selected single Au NP and current of the entire Au NP modified ITO electrode; (D) DFS signal decrease amplitude ΔI dependence of the initial light scattering intensity I_0 of single Au NPs.

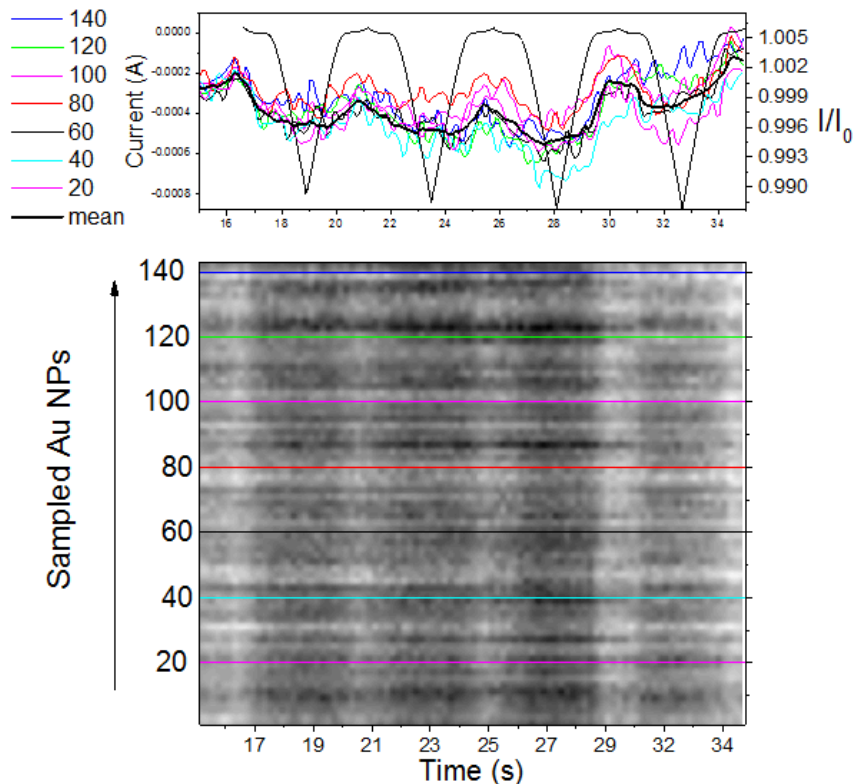


Figure 3.11: (top) Time evolutions of light scattering intensity relative to initial light intensity I/I_0 of seven selected single Au NP and average variation of scattering intensity I/I_0 of the total 150 Au NPs when the electrode potential was cycled linearly from -0.4 V to 0.75 V and then back to -0.4 V (vs. Ag/AgCl) for four cycles at a scan rate of 0.5 V/s; (bottom) Time evolutions of I/I_0 of all 150 Au NPs in DFS frame when the electrode potential was cycled linearly from -0.4 V to 0.75 V and then back to -0.4 V (vs. Ag/AgCl) for four cycles at a scan rate of 0.5 V/s.

3.4.4 Formation of Single Au NPs on ITO UME for DFS Spectroelectrochemistry Study of Hydrazine Oxidation

DFS light scattering intensity needs to be correlated to actual NP size to understand the shape and size dependence of the DFS spectroelectrochemistry responses to hydrazine oxidation. Also, a large amount of bubble formation at a planar ITO electrode coated with Au NPs can obscure more accurate analysis of DFS signal response and its correlation to current. A miniaturized ITO electrode is needed to address these issues of bulk ITO electrode without producing too much bubble near the imaging area while allowing us to obtain particle size, DFS

intensity, and current information. Multiple 10 μm (in diam.) ITO UMEs were fabricated using photolithography methods with each individual ITO UMEs electrically isolated from each other by ion mill process so that redox reaction can be addressed for each individual UME. SEM images of a typical ITO UME are shown in Figure 3.12A (a-c) to indicate the success of fabrication of ITO UME although the electrode size of 8.3 μm (in diam.) is smaller than our shadow mask used for photolithography because of the lack of quality control over focus distance of our microfabrication method. No residual photoresist was found on the surface of UMEs. It is worth mentioning that the ITO surface is quite heterogeneous at nanometer scale as suggested by our previous work¹⁷⁻¹⁹ that would affect the local contact and also contribute to DFS intensity as background signal. EDS results of Au NPs modified ITO UME indicates characteristic peaks for Au, as shown in Figure 3.13. The fabricated 10 μm (in diam.) ITO UMEs were tested electrochemically with 10 mM $\text{Fe}(\text{CN})_6^{4-}$ oxidation showing limiting current of $7.2 \times 10^{-9}\text{A}$ (Figure 3.14). The predicted disc electrode size using regular disc microelectrode model with the limiting current is around 5.7 μm (in diam.) by following $i_{\text{ss}}=2nFdCD_0$ with diffusion constant $D_0=6.5 \times 10^{-6}\text{cm}^2/\text{s}$, where d is the disc diameter. The calculated diameter is slightly smaller than actual size measured by SEM image. This is because of the presence of a <5 μm thick insulating photoresist layer, which can decrease the mass transfer of redox molecule by forming a small microwell. Figure 3.12A (c & d) shows the SEM and DFS images of ITO UME modified with Au NPs. The two images were taken at the same location and resemble each other although DFS is lack of spatial resolution as it only provides local light scattering features. Particles diameters were labeled in both figures for comparison. Au NPs covered by transparent photoresist outside of active UME were also resolved by DFS microscope, although those particles did not respond to hydrazine oxidation because they were not in contact with the

hydrazine solution. ITO UME clearly shows the potential of benefit in spectroelectrochemistry study of single NPs by providing both optical and electrochemical information of catalytic reaction at single or a few Au NPs. Such UME based transparent electrodes can also allow us to determine particle size and DFS intensity. After further analysis of the light intensity data, since it is possible to locate the same UME under both SEM and dark field microscope, Au NP size can be estimated from the initial DFS light intensity. The diameters of the Au NPs were obtained from SEM images. As shown in Figure 3.12B, a linear relationship between initial DFS light intensity and particle size was found in the range of 100-400 nm. In our previous study,¹⁷ the DFS intensities was correlated to particle sizes by Mie theory approximation with the help of SEM. With the help of UME technique in this study, all the particles on the active UME could be found under SEM and dark field microscope easily.

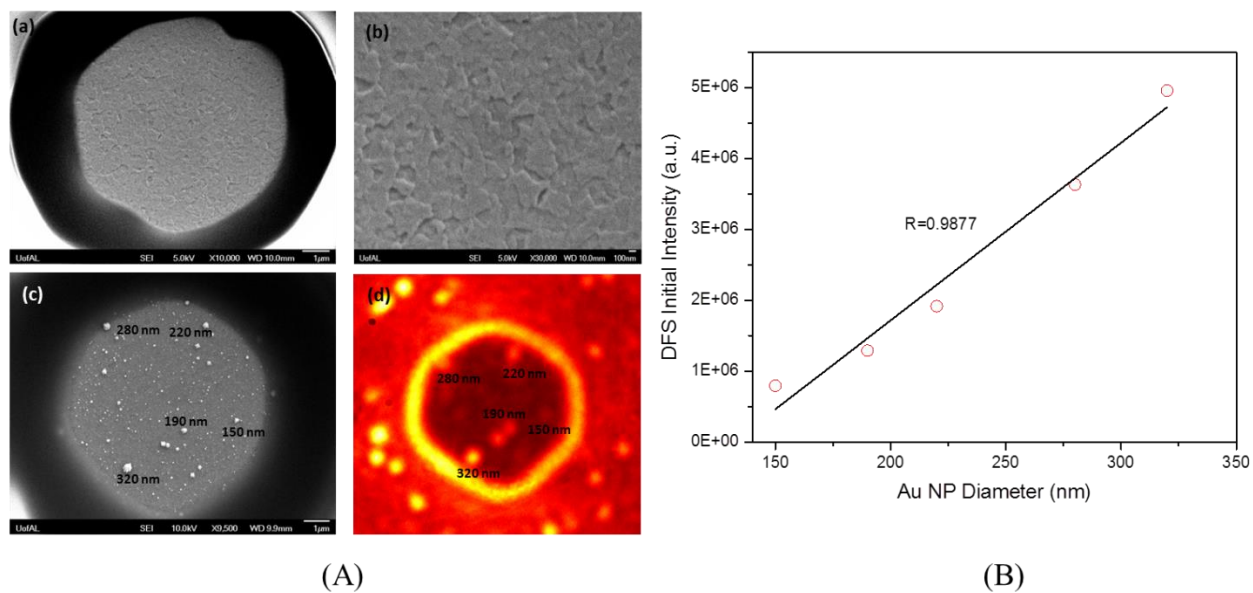


Figure 3.12: (A) SEM images of a bare ITO UME in low magnification (a), a zoom-in image of ITO electrode (b), SEM (c) and DFS (d) images of Au NPs-modified ITO UME; (B) DFS intensity of five Au NPs highlighted in (a) of panel A and corresponding particle diameter estimated by SEM at the same location.

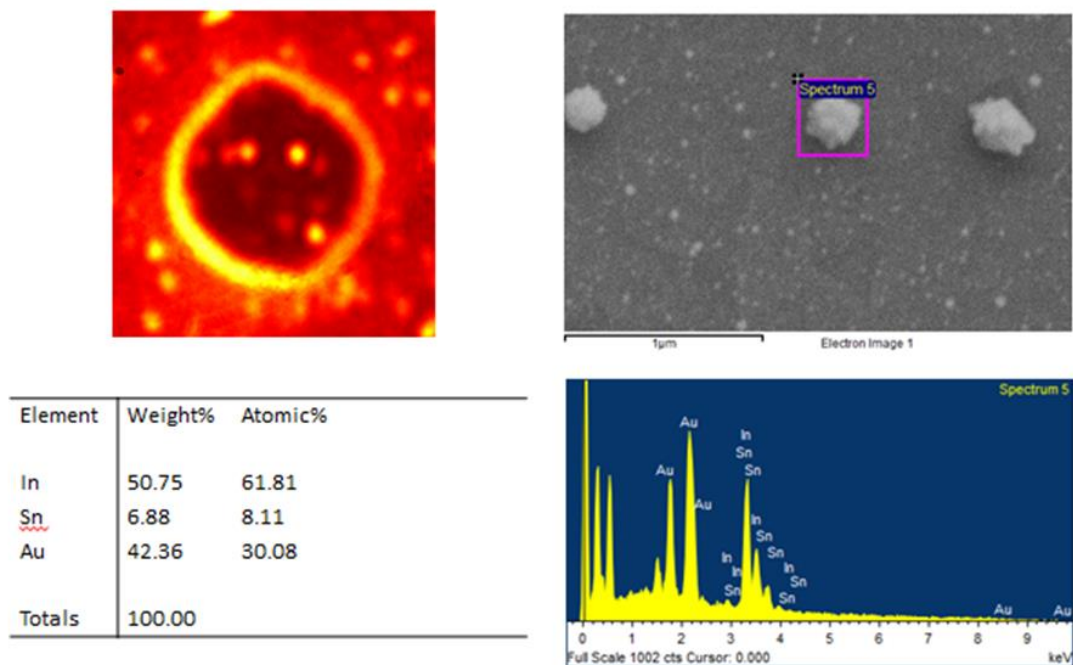


Figure 3.13: EDS result of Au NPs modified ITO UME. DFS image (top left) and high resolution SEM image (top right) show the size and shape of UME. EDS spectra (bottom right) indicates the element formation and abundance.

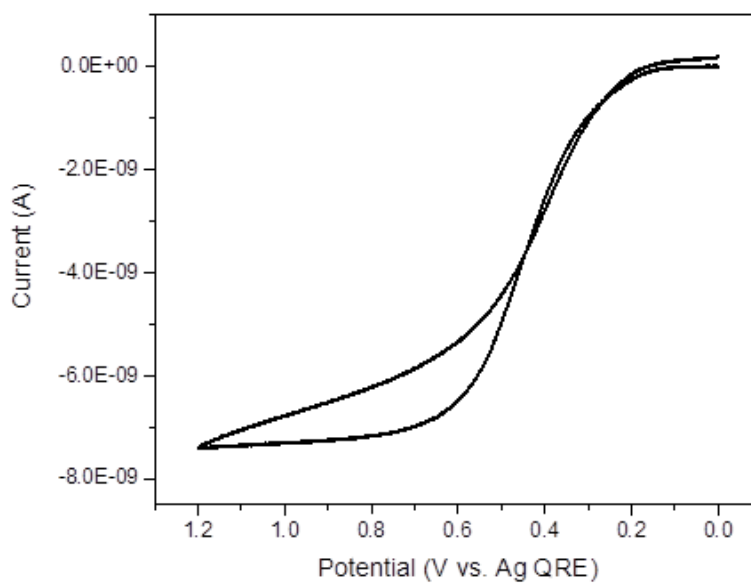


Figure 3.14: 10 mM ferrocyanide oxidation on 10 μm ITO UME

Hydrazine oxidation on ITO UME is sluggish, in contrast to Au UME. After coating with Au NPs, ITO electrode shows enhanced catalytic current and the catalytic current increase is dependent on Au NP coverage and particle size. Hydrazine oxidation was performed with Au

modified ITO UME in 50 mM and 1 M of hydrazine solution (Figure 3.15). Three consecutive cycles of oxidation show a decrease in current over the time. The possible explanation of the current decrease is the formation of N_2 bubble directly at the surface of Au NPs and/or ITO UME to partially blocking the active sites of Au NPs. Unlike the single nanobubble study of White and coworkers³¹⁻³³ at a single nanoelectrode, Au NPs supported by the ITO UME have size of ~170 nm (in diam.), N_2 shell on a Au NP may form temporarily in this case, but there is no evidence in our study to show that they will fully cover the whole area of Au NPs to prohibit oxidation of hydrazine. To correlate the DFS signal to current and potential signal of single Au NPs, combined electrochemistry and DFS experiment was repeated for Au NPs modified ITO UME. One particle from inside the UME and one particle from outside of the UME were selected for analysis, as shown in Figure 3.16. Four complete cycles of hydrazine oxidation were performed. The catalytic current upon hydrazine oxidation was in 10^{-9} A range when applying Au NPs modified UME as a working electrode due to the small surface area of ITO UME and a small number of active Au NPs for hydrazine oxidation. In addition, oxidation current for cycles 2, 3 and 4 is lower than the first cycle because the generation of N_2 gas molecules in the electrochemical reaction and surface adsorption of N_2H_3 would likely deactivate the surface of Au NPs inside UME, decreasing the faradaic current in the following cycles. Scattered light intensity from Au NPs inside UME shows different aspect than those from outside of UME. With the adsorbed N_2H_3 , the light intensity of Au NPs inside UME decreased. In contrast, there was only a minor effect on the particles outside of UME because of none contact with hydrazine solution. The minimum effect could be due to a capacitive charging of the Au NP. This light intensity decrease result agrees with that on planar ITO in previous experiments.

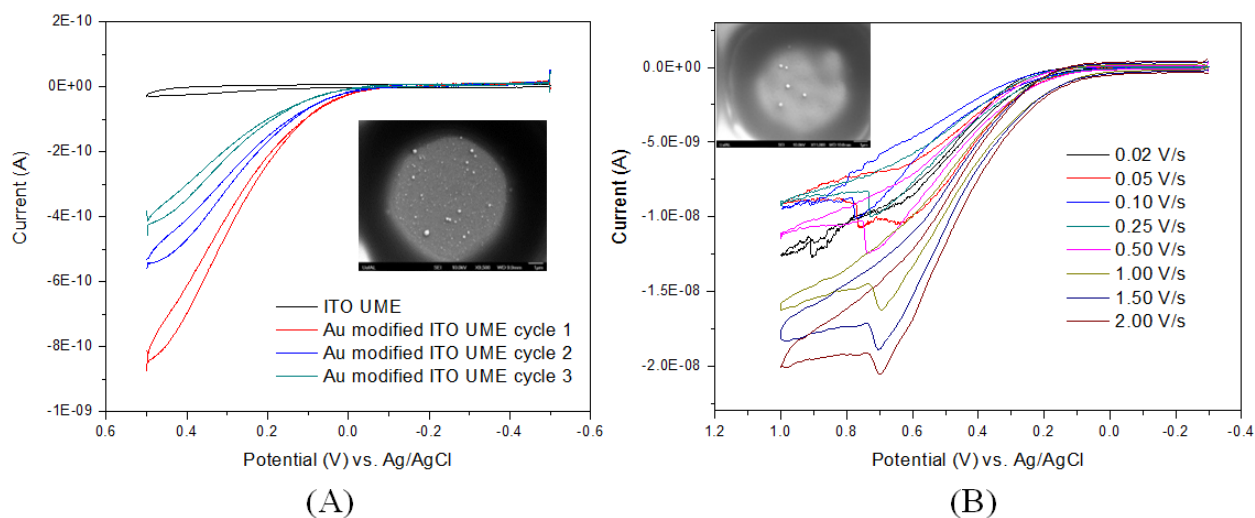


Figure 3.15: (A) three consecutive CVs of a few Au NPs modified ITO UME (colored) in 50 mM hydrazine in contrast to sluggish reaction at bare ITO UME (black). Inset: SEM image of the Au NPs-modified ITO UME; (B) CVs of hydrazine oxidation and scan rate dependence in 1.0 M hydrazine solution at a few Au NPs modified ITO UME. Inset: SEM image of the Au NPs-modified ITO UME.

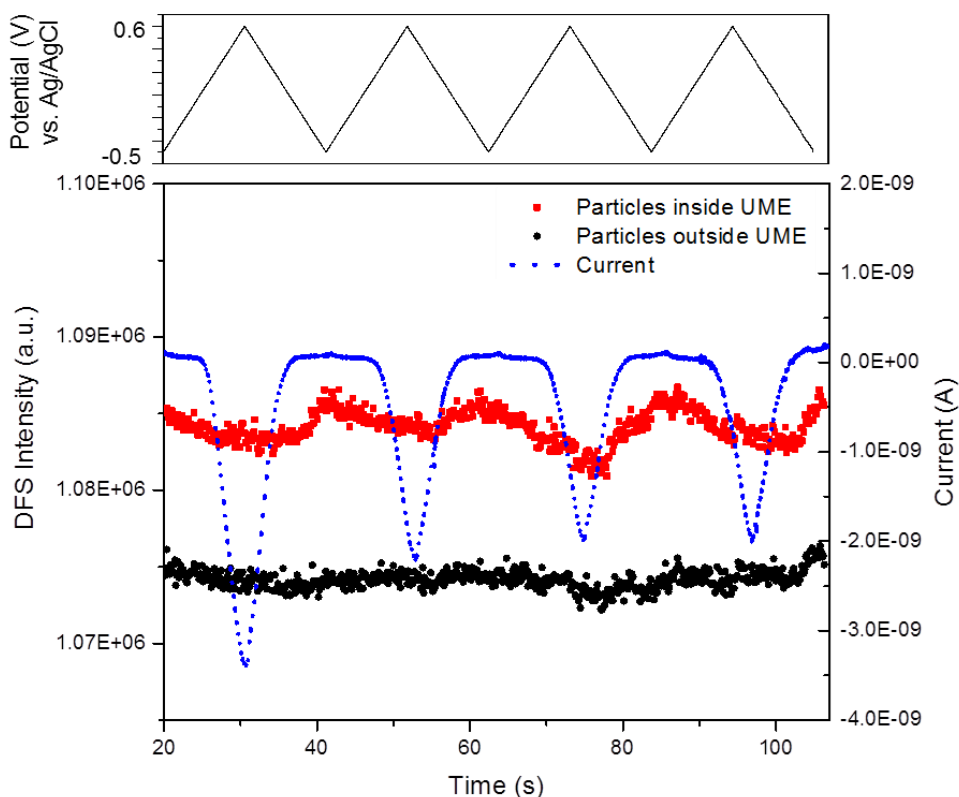


Figure 3.16: DFS intensity and current trajectories of two selected single Au NPs on a 10 μm (in diam.) ITO UME. One Au NP is located on the exposed ITO UME (red), and the other Au NP is buried under the insulating layer outside the ITO UME (black).

3.4.5 Scattering Simulations Using Mie Theory and COMSOL Multiphysics for Understanding the Effect of Local Refractive Index and Shell Thickness on Plasmon Scattering by Single Au NPs

Single NP light scattering intensity is related to many factors (e.g. particle size, refractive index, scattering angle, light wavelength etc.) according to Mie theory³⁴⁻³⁶ by solving the Maxwell equation, which provides numerical solutions with boundary conditions of light scattering small spherical objectives. As shown in Figure 3.17A, 134 ° incident light angle and 97 ° light scattering collection angle were used for computing the light scattering intensity dependence on incident light wavelength, refractive index of media and particle size based on the N.A.=0.8-0.92 of the dark field condenser and N.A.=0.75 OF A X40 optical objective. Dielectric function of Au NP used for Mie simulation is from a modified Drude-type model according to previous work of Derkachova and coworkers³⁷. Dielectric function of Au NP is plotted in Figure 3.17B. The scattering intensity vs. wavelengths of incident light was plotted with single gold scattering sphere under different refractive indexes of the surrounding medium. The refractive index of water is 1.33 at 25°C and the refractive index of nitrogen gas is 1.00 at 25°C. The simulated particle size was 100 nm in diameter. The simulation was based on monochromatic incident light with a wavelength of 633 nm and stand-alone single particle without considering the substrate light reflection and interference. The scattered light intensity was simulated at an incident light of 1 W/m² and the detection distance of 0.51 mm. As shown in Figure 3.17C, the scattering light intensity decreases significantly with the decrease of medium refractive index (from 1.33 to 1.00). Particle size effect was also studied by Mie simulation. Figure 3.17D shows the particle size effect on scattering intensity with particle diameter from 10 to 200 nm. With the increase of the particle size, the scattering intensity increased accordingly. Different refractive

indexes of surrounding medium were also considered in the particle size dependence of light scattering. Consistent trend of light scattering intensity decrease was obtained with the decrease of medium refractive index. The simulation result indicates that less scattered light was transmitted to the objective when the refractive index of the surrounding medium decreased, which agrees with the above experimental results.

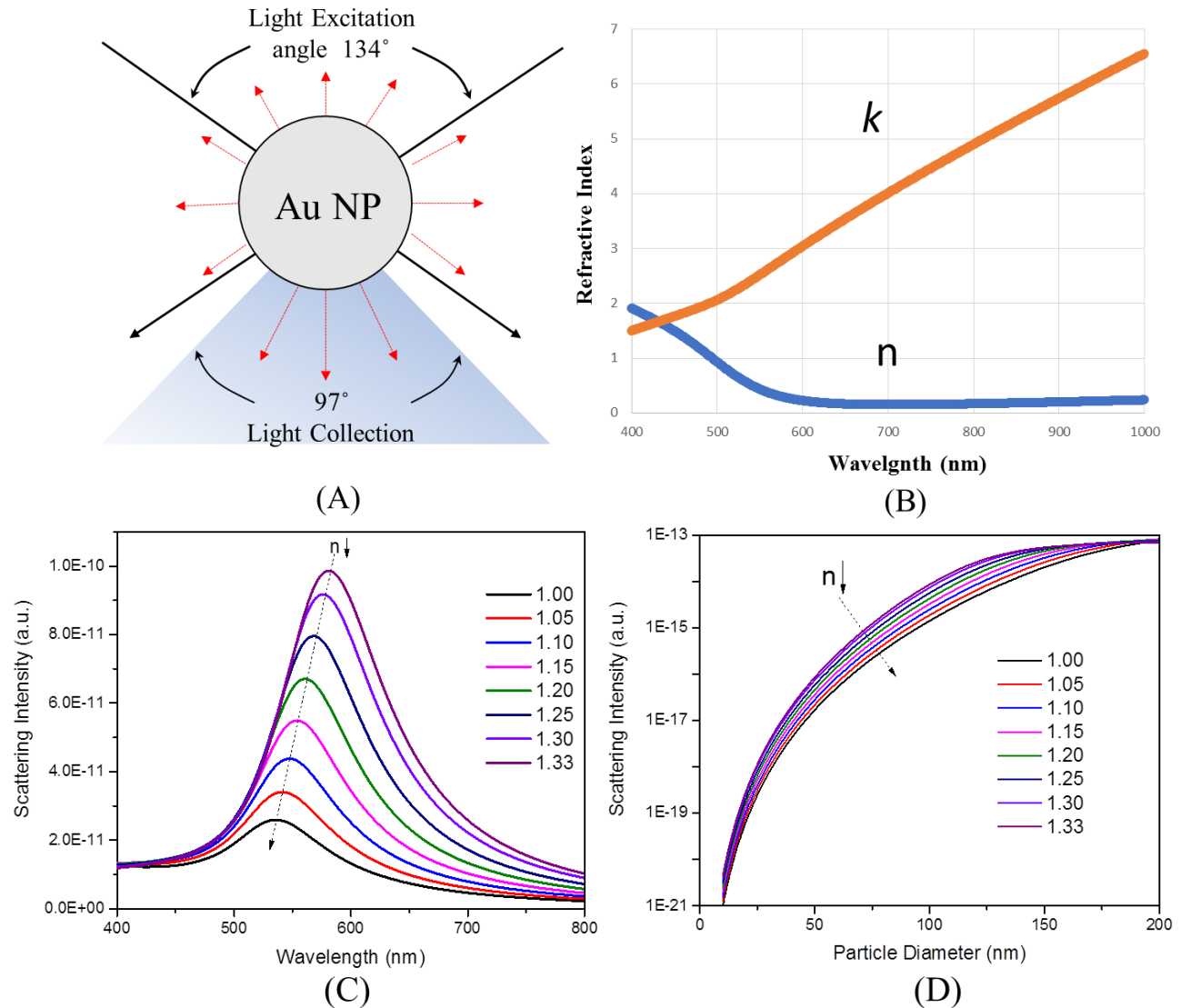


Figure 3.17: (A) DFS light collection and incident light geometry that is used in DFS-EC equipment for calculating light scattering intensity with Mie theory; (B) Simulated light scattering spectrum of a single 100 nm (in diam.) Au NP in media with various refractive indexes from 1.33 to 1.00; (C) Mie simulation of light scattering intensity in dependences of medium refractive index. (D) Simulated light scattering intensity as a function of Au NP size.

To generate an improved understanding of the observed light scattering responses during hydrazine oxidation at Au NPs, COMSOL Multiphysics was used to model the light scattering properties of a single Au NP in the core-shell geometry in water as depicted in Figure 3.18A. Solutions were found for Au@Au₂O₃ NPs placed at the planar interface between two non-absorbing dielectric media, one representing the substrate (ITO, $n_{sub} = 2$) and one representing the solution (H₂O, $n_{med} = 1.33$). Values for the wavelength-dependent complex refractive indices of Au and Au₂O₃ were taken from literature values.³⁸⁻³⁹ The values for Au₂O₃ were taken from ellipsometry studies of anodically formed, 1.1 nm Au₂O₃ films, and should thus be readily applicable to the present studies. Simulations were carried out for varying Au₂O₃ thicknesses, assuming the inner (Au) and outer (Au + Au₂O₃) radii of the core-shell structure were related as:

$$r_{Au_2O_3}^3 = \frac{V_{Au_2O_3}^m r_0^3}{2V_{Au}^m} + \left(1 - \frac{V_{Au_2O_3}^m}{2V_{Au}^m}\right) r_{Au}^3 \quad (6)$$

where $r_{Au_2O_3}$ is the outer radius of the core-shell structure, r_{Au} is the inner radius of the structure, r_0 is the initial radius of the non-oxidized Au NP, and $V_{Au}^m/V_{Au_2O_3}^m$ are the molar volumes of Au and Au₂O₃. Results from these simulations for structures with varying Au₂O₃ thicknesses are given in Figure 3.18B.

Calculations were carried out to simulate the effects of oxidation on a Au NP with a 50 nm radius. Calculated spectra are given for inner Au core radii between 50 nm (no Au₂O₃ shell) and 48 nm (~3.7 nm thick Au₂O₃ shell). The calculated scattering spectra display significant peak shifts over this range from ~590 nm to ~650 nm. These redshifts as the Au₂O₃ shell is grown via oxidation would result in a significant decrease in the scattering of radiation initially on resonance with the NP, which is illustrated in Figure 3.18B for several excitation wavelengths. For excitation at the peak wavelength (590 nm), 30% of the scattering intensity is lost after just 1

nm of the Au core is oxidized, which provides quantitative support for the interpretation of the experimental scattering data discussed above in terms of the formation of ultrathin Au₂O₃ layers on the surface of Au NPs. When the concentration of hydrazine is low, thin (1-2 nm) Au₂O₃ layers are formed anodically on the NP surface during voltammetry, resulting in a significant loss in scattering intensity. Higher concentrations of hydrazine inhibit the formation of Au₂O₃ and result in smaller changes in scattering intensity upon anodization.

Changes in scattering intensity due to the formation of adsorbed N₂ or N₂H₃ species were also investigated. Simulations were again carried out for the geometry depicted in Figure 3.18A for r = 50 nm Au NPs with varying thicknesses of N₂ (n = 1) or N₂H₃ (n = 1.46) shells.³⁷ Simulated scattering cross-sections at 633 nm for shell thicknesses between 10 and 200 nm are given in Figure 3.18C. Although no strong experimental evidence suggests the formation of a stable nitrogen shell around the Au NPs, these simulations only qualitatively suggest that the formation of N₂ on the NP would lead to a blue-shift in the light scattering spectrum, yielding a decrease in scattering intensity at moderate shell thicknesses (< 50 nm) at the wavelengths longer than the plasmon resonance peak position. Above these thicknesses, an increase in scattering is observed due to scattering by the large N₂ bubble formed around the NP. Adsorption of N₂H₃ would result in only minor red-shifts induced by its larger refractive index in contrast to Au₂O₃, yielding only a minor increase in light scattering at wavelengths longer than plasmon resonance wavelength (590 nm). The discrepancy between these results and our experimental data is due to our sample exhibiting a longer resonance scattering peak at 650 nm (Figure 3.8A) than the calculated spectrum, ascribed to heterogeneities in Au NP shapes and size as well as NP aggregation, yielding a decrease in light scattering at 633 nm upon the red-shifting in scattering spectrum in the presence of the N₂H₃ shell. The observed shift is not as significant as that

observed for gold oxide because of the lower refractive index than of N_2H_3 . The lack of any observed change in scattering suggests that monolayer of N_2H_3 accumulation at the NP surface causes only a minor change in light scattering intensity, in contrast to the formation of Au_2O_3 and N_2 bubble.

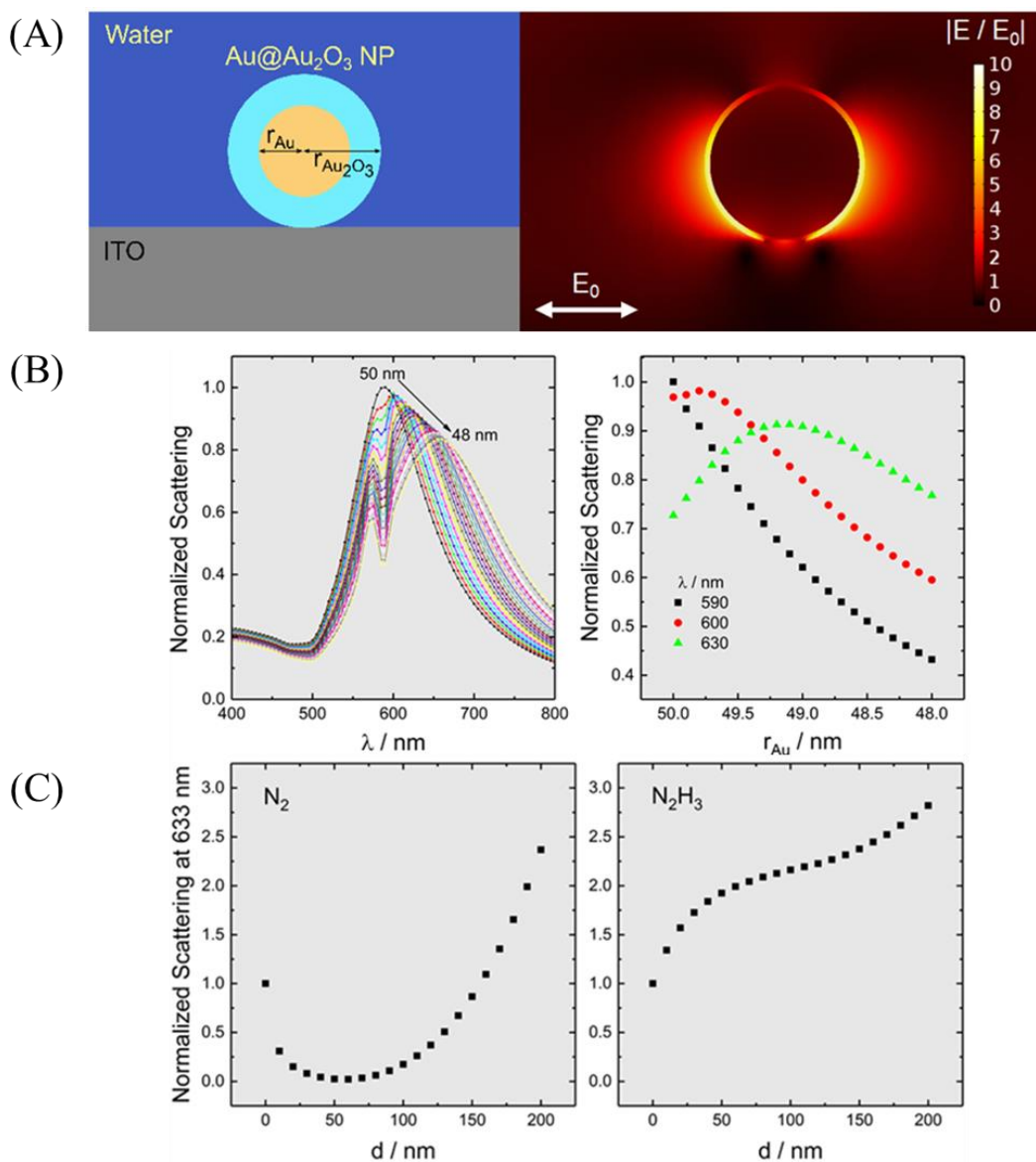


Figure 3.18: (A) Simulation geometry for scattering simulations consisting of a core-shell Au- Au_2O_3 NP at the planar interface of ITO and water (left) and example calculated field distribution, given as the ratio of the scattered to incident fields for a 48 nm core radius, 3.7 nm shell thickness, and a wavelength of 650 nm (right). (B) Calculated scattering spectra and scattering intensities at specific wavelengths for the core-shell structure during anodization as a function of inner r_{Au} . r_{Au} and $r_{Au_2O_3}$ are related as described in the text. (C) Calculated scattering intensities at 633 nm for $r = 50$ nm Au NPs with varying thicknesses of N_2 or N_2H_3 shells.

3.5 Conclusions

In summary, the kinetics of electrocatalytic oxidation of hydrazine at Au NPs were analyzed by real-time using light scattering spectroelectrochemistry methods at planar and miniaturized ITO electrodes. At low overpotential region, oxidation of hydrazine yields a decrease in DFS intensity of single Au NPs because of double layer charging and surface adsorption of N_2H_3 . A significant decrease in DFS signal of Au NPs in the high overpotential region can be obtained in the absence of hydrazine because of Au oxidation. Such oxide-induced light scattering signal decrease is dependent on the concentration of hydrazine and it can be completely eliminated in the presence of > 50 mM hydrazine. N_2 bubbles generation take places under several conditions, including high overpotential, higher Au NP coverage, and slow potential scan rate, to deactivate NPs accompanied with a decrease in oxidation current and increase in light scattering by the gas bubbles. ITO UME provides consistent results of DFS-EC activities of single Au NPs with the unique capability of resolving both current and DFS signal of a few Au NPs, correlating their particle sizes to DFS responses at the single NP level. Compared with NP detection method based on spontaneous collision events (Figure 3.19), ITO UME technique in combination with DFS provides a better understanding of catalytic reactions and reproducibility. Theoretical modeling with Mie theory and COMSOL simulation provides consistent results which support the above conclusion from our spectroelectrochemistry study. The spectroelectrochemistry study presented in this chapter sets a fundamental basis for the broad applications of plasmonic NPs in various kinds of catalytic reactions described in the following chapters.

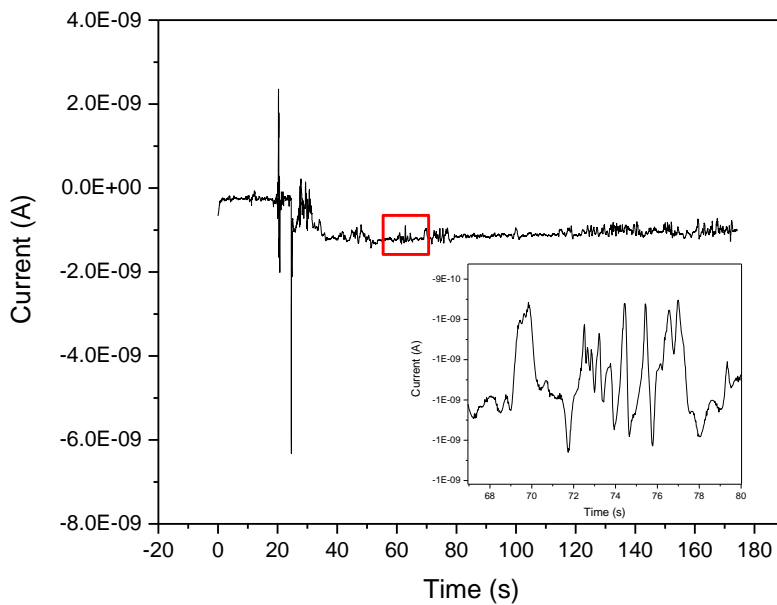


Figure 3.19: Au nanoparticle collision experiment on 10 μm ITO UME under 0.3 V vs. Ag QRE. Inset is the zoom in of the red rectangular area

3.6 References

1. Kiss, L. B.; Söderlund, J.; Niklasson, G. A.; Granqvist, C. G., New Approach to the Origin of Lognormal Size Distributions of Nanoparticles. *Nanotechnology* **1999**, *10*, 25-28.
2. Chen, A.; Holt-Hindle, P., Platinum-Based Nanostructured Materials: Synthesis, Properties, and Applications. *Chem. Rev.* **2010**, *110*, 3767-804.
3. Burch, R., Gold Catalysts for Pure Hydrogen Production in the Water-Gas Shift Reaction: Activity, Structure and Reaction Mechanism. *Phys. Chem. Chem. Phys.* **2006**, *8*, 5483-5500.
4. Thielecke, N.; Vorlop, K.-D.; Prüfe, U., Long-Term Stability of an Au/Al₂O₃ Catalyst Prepared by Incipient Wetness in Continuous-Flow Glucose Oxidation. *Catal. Today* **2007**, *122*, 266-269.
5. Zhong, C.-J.; Luo, J.; Mott, D.; Maye, M. M.; Kariuki, N.; Wang, L.; Njoki, P.; Schadt, M.; Lim, S. I. I.; Lin, Y., Gold-Based Nanoparticle Catalysts for Fuel Cell Reactions. In *Nanotechnology in Catalysis: Volume 3*, Zhou, B.; Han, S.; Raja, R.; Somorjai, G. A., Eds. Springer New York: New York, NY, 2007; pp 289-307.
6. Weng, Y. C.; Fan, F.-R. F.; Bard, A. J., Combinatorial Biomimetics. Optimization of a Composition of Copper(II) Poly-L-Histidine Complex as an Electrocatalyst for O₂ Reduction by Scanning Electrochemical Microscopy. *J. Am. Chem. Soc.* **2005**, *127*, 17576-17577.

7. Xiao, X.; Bard, A. J., Observing Single Nanoparticle Collisions at an Ultramicroelectrode by Electrocatalytic Amplification. *J. Am. Chem. Soc.* **2007**, *129*, 9610-9612.
8. Xiao, X.; Fan, F.-R. F.; Zhou, J.; Bard, A. J., Current Transients in Single Nanoparticle Collision Events. *J. Am. Chem. Soc.* **2008**, *130*, 16669-16677.
9. Jung, A. R.; Lee, S.; Joo, J. W.; Shin, C.; Bae, H.; Moon, S. G.; Kwon, S. J., Potential-Controlled Current Responses from Staircase to Blip in Single Pt Nanoparticle Collisions on a Ni Ultramicroelectrode. *J. Am. Chem. Soc.* **2015**, *137*, 1762-1765.
10. Chen, S.; Kucernak, A., Electrodeposition of Platinum on Nanometer-Sized Carbon Electrodes. *J. Phys. Chem. B* **2003**, *107*, 8392-8402.
11. Chen, S.; Kucernak, A., Electrocatalysis under Conditions of High Mass Transport: Investigation of Hydrogen Oxidation on Single Submicron Pt Particles Supported on Carbon. *J. Phys. Chem. B* **2004**, *108*, 13984-13994.
12. Lakbub, J.; Pouliwe, A.; Kamasah, A.; Yang, C.; Sun, P., Electrochemical Behaviors of Single Gold Nanoparticles. *Electroanalysis* **2011**, *23*, 2270-2274.
13. Dudin, P. V.; Unwin, P. R.; Macpherson, J. V., Electro-Oxidation of Hydrazine at Gold Nanoparticle Functionalised Single Walled Carbon Nanotube Network Ultramicroelectrodes. *Phys. Chem. Chem. Phys.* **2011**, *13*, 17146-17152.
14. Hill, C. M.; Clayton, D. A.; Pan, S., Combined Optical and Electrochemical Methods for Studying Electrochemistry at the Single Molecule and Single Particle Level: Recent Progress and Perspectives. *Phys. Chem. Chem. Phys.* **2013**, *15*, 20797-20807.
15. Shan, X., et al., Imaging the Electrocatalytic Activity of Single Nanoparticles. *Nat. Nanotechnol.* **2012**, *7*, 668.
16. Shan, X.; Wang, S.; Tao, N., Study of Single Particle Charge and Brownian Motions with Surface Plasmon Resonance. *Appl. Phys. Lett.* **2010**, *97*, 223703.
17. Hill, C. M.; Pan, S., A Dark-Field Scattering Spectroelectrochemical Technique for Tracking the Electrodeposition of Single Silver Nanoparticles. *J. Am. Chem. Soc.* **2013**, *135*, 17250-17253.
18. Hill, C. M.; Bennett, R.; Zhou, C.; Street, S.; Zheng, J.; Pan, S., Single Ag Nanoparticle Spectroelectrochemistry Via Dark-Field Scattering and Fluorescence Microscopies. *J. Phys. Chem. C* **2015**, *119*, 6760-6768.
19. Pan, S.; Liu, J.; Hill, C. M., Observation of Local Redox Events at Individual Au Nanoparticles Using Electrogenenerated Chemiluminescence Microscopy. *J. Phys. Chem. C* **2015**, *119*, 27095-27103.

20. Wusimanjiang, Y.; Ma, Y.; Lee, M.; Pan, S., Single Gold Nanoparticle Electrode for Electrogenerated Chemiluminescence and Dark Field Scattering Spectroelectrochemistry. *Electrochim. Acta* **2018**, *269*, 291-298.
21. Xu, W.; Kong, J. S.; Yeh, Y.-T. E.; Chen, P., Single-Molecule Nanocatalysis Reveals Heterogeneous Reaction Pathways and Catalytic Dynamics. *Nat. Mater.* **2008**, *7*, 992-996.
22. Brasiliense, V.; Berto, P.; Combellas, C.; Tessier, G.; Kanoufi, F., Electrochemistry of Single Nanodomains Revealed by Three-Dimensional Holographic Microscopy. *Acc. Chem. Res.* **2016**, *49*, 2049-2057.
23. Eisner, U.; Gileadi, E., Anodic Oxidation of Hydrazine and Its Derivatives: Part I. The Oxidation of Hydrazine on Gold Electrodes in Acid Solutions. *J. Electroanal. Chem. Interface. Electrochem.* **1970**, *28*, 81-92.
24. Joplin, A.; Hosseini Jebeli, S. A.; Sung, E.; Diemler, N.; Straney, P. J.; Yorulmaz, M.; Chang, W.-S.; Millstone, J. E.; Link, S., Correlated Absorption and Scattering Spectroscopy of Individual Platinum-Decorated Gold Nanorods Reveals Strong Excitation Enhancement in the Nonplasmonic Metal. *ACS Nano* **2017**, *11*, 12346-12357.
25. Novo, C.; Funston, A. M.; Gooding, A. K.; Mulvaney, P., Electrochemical Charging of Single Gold Nanorods. *J. Am. Chem. Soc.* **2009**, *131*, 14664-14666.
26. Jing, C.; Rawson, F. J.; Zhou, H.; Shi, X.; Li, W.-H.; Li, D.-W.; Long, Y.-T., New Insights into Electrocatalysis Based on Plasmon Resonance for the Real-Time Monitoring of Catalytic Events on Single Gold Nanorods. *Anal. Chem.* **2014**, *86*, 5513-5518.
27. Dondapati, S. K.; Ludemann, M.; Müller, R.; Schwieger, S.; Schwemer, A.; Händel, B.; Kwiatkowski, D.; Djiango, M.; Runge, E.; Klar, T. A., Voltage-Induced Adsorbate Damping of Single Gold Nanorod Plasmons in Aqueous Solution. *Nano Lett.* **2012**, *12*, 1247-1252.
28. Hoener, B. S.; Byers, C. P.; Heiderscheidt, T. S.; De Silva Indrasekara, A. S.; Hoggard, A.; Chang, W.-S.; Link, S.; Landes, C. F., Spectroelectrochemistry of Halide Anion Adsorption and Dissolution of Single Gold Nanorods. *J. Phys. Chem. C* **2016**, *120*, 20604-20612.
29. Sannomiya, T.; Dermutz, H.; Hafner, C.; Vörös, J.; Dahlin, A. B., Electrochemistry on a Localized Surface Plasmon Resonance Sensor. *Langmuir* **2010**, *26*, 7619-7626.
30. Byers, C. P.; Hoener, B. S.; Chang, W.-S.; Link, S.; Landes, C. F., Single-Particle Plasmon Voltammetry (Sppv) for Detecting Anion Adsorption. *Nano Lett.* **2016**, *16*, 2314-2321.
31. Chen, Q.; Wiedenroth, H. S.; German, S. R.; White, H. S., Electrochemical Nucleation of Stable N₂ Nanobubbles at Pt Nanoelectrodes. *J. Am. Chem. Soc.* **2015**, *137*, 12064-12069.
32. German, S. R.; Chen, Q.; Edwards, M. A.; White, H. S., Electrochemical Measurement of Hydrogen and Nitrogen Nanobubble Lifetimes at Pt Nanoelectrodes. *J. Electrochem. Soc.* **2016**, *163*, 3160-3166.

33. Luo, L.; White, H. S., Electrogeneration of Single Nanobubbles at Sub-50-Nm-Radius Platinum Nanodisk Electrodes. *Langmuir* **2013**, *29*, 11169-11175.
34. Tsang, L.; Kong, J. A.; Ding, K.-H., Introduction to Electromagnetic Scattering by a Single Particle. In *Scattering of Electromagnetic Waves: Theories and Applications*, John Wiley & Sons, Inc.: 2002; pp 1-52.
35. Wriedt, T., Mie Theory: A Review. In *The Mie Theory: Basics and Applications*, Hergert, W.; Wriedt, T., Eds. Springer Berlin Heidelberg: Berlin, Heidelberg, 2012; pp 53-71.
36. Fu, Q.; Sun, W., Mie Theory for Light Scattering by a Spherical Particle in an Absorbing Medium. *Appl. Opt.* **2001**, *40*, 1354-1361.
37. Derkachova, A.; Kolwas, K.; Demchenko, I., Dielectric Function for Gold in Plasmonics Applications: Size Dependence of Plasmon Resonance Frequencies and Damping Rates for Nanospheres. *Plasmonics* **2016**, *11*, 941-951.
38. Johnson, P. B.; Christy, R. W., Optical Constants of the Noble Metals. *Phys. Rev. B* **1972**, *6*, 4370-4379.
39. Cook, K. M.; Ferguson, G. S., Determination of the Wavelength-Dependent Refractive Index of a Gold-Oxide Thin Film. *J. Phys. Chem. C* **2011**, *115*, 22976-22980.

CHAPTER 4

SPECTROELECTROCHEMISTRY STUDY OF Au@Pt CORE-SHELL NANOPARTICLE ELECTRODES FOR CONTROLLED METHANOL AND FORMIC ACID OXIDATION

4.1 Abstract

Noble metallic nanoparticles (NPs) such as Au, Ag, and Pt have interesting catalytic and optical properties, which play important roles in molecular sensing and alternative energy harvesting, conversion, and storage. Pt layers-modified Au surfaces were recently found to enhance the electrocatalytic activity of methanol and formic acid oxidation. In this study, Au-coated transparent indium tin oxide (ITO) electrode was further modified by Pt for spectroelectrochemistry study of methanol and formic acid oxidation. The thickness of Pt layer was precisely controlled by electrochemical deposition cycles. The Pt deposition was performed on Au-ITO at 1, 5, 10, 20, 30 cycles to have different Pt coverage. Scanning electron microscopy (SEM) and high-resolution transmission electron microscopy (HRTEM) results confirmed the core-shell nano-architecture structure of Au-Pt NPs. Such architecture led to the enhanced catalytic activity for both methanol and formic acid oxidation. The resulting oxidation current density was more than 200 times with Au@Pt(30) NPs sample for both methanol and formic acid in comparison with Au-ITO. In-situ dark-field scattering electrochemical study of methanol oxidation in 0.1 M NaOH suggested that Au NPs undergo anodization in the potential window of methanol oxidation only for lower Pt coverage. Interestingly, Au anodization gets weaker and was terminated at higher Pt thicknesses. Lower coverage of Pt on Au surface favors the direct

oxidation of formic acid to CO₂.

4.2 Introduction

Alloyed NPs has attracted the attention of researchers owing to their vital role for fuel cells application because their electrocatalytic activities are normally higher than the monometallic NPs.¹⁻⁴ To fully realize the electrocatalytic potentials of the alloyed metallic NPs, precise structural control at the nanoscale level is essential. Pt-based nanomaterials have been well-studied and are considered as the most efficient catalysts especially for methanol and formic acid oxidation.⁵⁻⁸ However, methanol and formic acid oxidation reactions on Pt surface easily suffer from inevitable CO poisoning, which eventually limits the fuel cell efficiency and the stability.⁹⁻¹⁰ Among the various approaches developed for improving the electrocatalytic performance of Pt, Pt-based noble bimetallic nanomaterials have been extensively investigated.¹¹⁻¹⁴ The Au-Pt alloy including Au@Pt core-shell NPs is one of the most studied Pt-based bimetallic nanomaterials. Liu et al.¹⁵ successfully fabricated three-dimensional porous AuPt alloy films for methanol and formic acid oxidation reactions. The Au₁₀₀Pt₁ alloy structure exhibited superior electrocatalytic activity towards formic acid oxidation and the CO poisoning was completely removed. Su and coworkers¹⁶ prepared Au@Pt bimetallic nanodendrite-decorated molybdenum disulfide nanosheets, which delivered more than 3000 times of current for methanol oxidation than the Pt/C catalyst. Despite of such promising abilities of Au@Pt, the Au@Pt electrode materials usually faces the aggregation issue in both synthetic and catalytic reaction processes. Additionally, the electrode surface condition during the catalytic reaction remained unknown and largely unexplored.

Electrodeposition is one of ideal and simple methods to prepare NPs from precursors on conductive substrates.¹⁷⁻¹⁹ Since the NPs are electrochemically attached to the substrate,

aggregation could be completely avoided by controlling appropriate electrochemical conditions. Electrodeposited NPs on transparent electrodes such as ITO also assists the study of electrode surface state by spectroscopic techniques. Shan et al.²⁰⁻²¹ demonstrated a plasmonic-based electrochemical current imaging method to study the surface charges and the electrocatalytic properties of Pt NPs. The refractive index at the electrode surface was decreased during the proton reduction reaction, which changed the surface plasmon resonance and made it possible to detect the local redox event on single Pt NPs. In our previous study,²² Au NPs were electrodeposited onto ITO electrodes to investigate the electrochemical oxidation of hydrazine on Au surface. Dark-field light-scattering coupled with electrochemical measurements revealed that the Au oxidation, double-layer charging and surface adsorbates during the reaction could be resolved by examining the change in light scattering intensity.

In the present work, we employed the electrodeposition method to further modify the Au NPs surface by Pt for the synthesis of Au@Pt NPs core-shell architecture. The morphology and composition of the Au@Pt NPs were examined by SEM, HRTEM and energy-dispersive X-ray spectroscopy (EDS). The coverage of the Pt layer was precisely controlled by tuning the electrochemical deposition conditions. The as-prepared Au@Pt NPs served as efficient electrocatalytic substrates for methanol and formic acid oxidation reaction. The Pt-coverage-dependent electrocatalytic performance was investigated. In-situ dark-field spectroelectrochemistry measurements were performed during the electrochemical oxidation reaction and the change in electrode surface was also studied.

4.3 Experimental

4.3.1 Reagents and Materials

HAuCl₄ (30% wt. in dilute HCl) was purchased from Sigma-Aldrich. H₂PtCl₆•xH₂O and formic acid (88%+ liquid) was purchased from Alfa Aesar. Methanol was purchased from Fisher Scientific. All chemicals and solvents were used as received without any further purification. All the solutions were freshly prepared using high-purity deionized water (Resistivity >18 MΩ•cm). ITO coated glass (< 15 ohms/sq.) was purchased from Colorado Concept Coatings, LLC. The electrochemical measurements were performed by CH Instruments 760C or 1021C electrochemical analyzer.

4.3.2 Synthesis of Au@Pt NPs

Au NPs-modified ITO substrate was prepared based on a method described in a previous publication by the Pan group.²²⁻²³ In brief, the electrodeposition of Au NPs was performed in 0.5 mM HAuCl₄ solution by multistep potential technique with different nucleation and growth potentials using a three-electrode system, wherein Pt wire, ITO and Ag/AgCl (*sat'd KCl*) served as the counter, working and reference electrodes, respectively. A nucleation potential of -0.6 V (vs. Ag/AgCl) and a growth potential of -0.2 V (vs. Ag/AgCl) was chosen in this case to obtain the desired particle sizes. Pt NPs were then deposited onto Au NPs using the similar multistep potential deposition method. In this case, a 0 V vs. Ag/AgCl potential was applied to Au NPs modified ITO for 10 s, followed by 0.4 V vs. Ag/AgCl for 30 s in 3mM H₂PtCl₆ solution with 0.1 M KCl. This potential stepping was repeated for number of cycles to control the thickness or amount of Pt deposited onto the surface of Au NPs. In general, the Au@Pt NPs samples are designated as Au@Pt(n), where n represents the potential cycle number.

4.3.3 Characterization of Au@Pt NPs

The synthesized Au@Pt NPs were further characterized by scanning electron microscopy (SEM) and transmission electron microscopy (TEM) techniques. SEM images were taken from

JOEL 7000 SEM at 20 kV accelerating voltage. A focused ion beam (FIB) technique was used to prepare site-specific electron transparent lamella of Au-Pt core-shell NPs deposited on ITO substrate for TEM and HRTEM studies. TEM specimens were made using in-situ lift-out FIB method in an FEI Quanta 200 3D Dual Beam FIB microscope (FEI Company, Hillsboro, OR). The bright-field HRTEM, high-angle annular dark-field (HAADF) and TEM-EDS mapping images of the Au-Pt core-shell interface with the ITO were captured on a 200-keV FEI Tecnai F-20 scanning-transmission electron microscope (STEM). The average particle sizes and distribution were calculated by free imaging processing and analysis software ImageJ. The UV-vis spectra were obtained using an HP 8452A diode array UV-Vis spectrophotometer, recording spectra over the range 300-800 nm with a resolution of 2 nm.

4.3.4 In-Situ Dark-Field Scattering Measurements

The Au@Pt NPs sample was vertically assembled into a home-built electrochemical cell with two quartz windows for laser light excitation and scattering. A 632.8 nm laser (10 mW HRP050, Thorlabs Inc.) was used as a light source. The electrochemical cell was filled with 0.1 M NaOH electrolyte containing 0.5 M methanol. The cyclic voltammetry curves were performed from -1.0 to 0.75 V (vs. Ag/AgCl) for methanol oxidation at the scan rate of 0.1 V s⁻¹. In situ light scattering was detected by a photomultiplier tube (PMT). A 5 mm (in diameter) graphite rod was used as the counter electrode and a calibrated Ag quasi-reference electrode (QRE) was used as reference electrode. The scattered laser intensity signal from the PMT was converted to an analog current signal and recorded along with the working electrode current response with a CH Instruments 1021C multipotentiostat. For formic acid oxidation reaction, the electrolyte used was 0.1 M formic acid in 0.1 M H₂SO₄. The cyclic voltammograms (CVs) were recorded from -0.1 to 0.9 V at the scan rate of 0.05 V s⁻¹.

4.4 Results and Discussion

4.4.1 Electrochemical and Morphological Study of Au@Pt NPs

Figure 4.1A shows the CVs of ITO and Au-modified ITO substrates revealing reduction of H_2PtCl_6 . Pt^{4+} reduction appears to be sluggish on ITO compared to Au-ITO. Evidently, the Pt^{4+} is reduced at 0 V (vs. Ag/AgCl) on Au but not on ITO. Therefore, 0 V (vs. Ag/AgCl) was chosen as the deposition potential for the synthesis of Au@Pt samples to specifically avoid the deposition of Pt NPs on the ITO surface. The electrodeposition of Pt layers was performed from a solution containing a mixture of 3 mM H_2PtCl_6 and 0.5 M NaCl (pH 4.2). The deposition potential was stepped between 0 V for 10 s and 0.4 V for 30 s, which was considered as one deposition cycle. Figure 4.1B shows the chronoamperometry curve for Pt deposition for 20 cycles (Au@Pt(20) electrode). With excess deposition of Pt onto the Au NPs, the particles tend to have a higher catalytic activity, which can be seen from the higher deposition current at 0 V vs. Ag/AgCl. The coverage and thickness of Pt on Au NPs were precisely controlled by controlling the deposition cycles. 1, 5, 10, 20 and 30 cycles of deposition was performed, which provided Au@Pt(n) samples (n indicates cycle numbers).

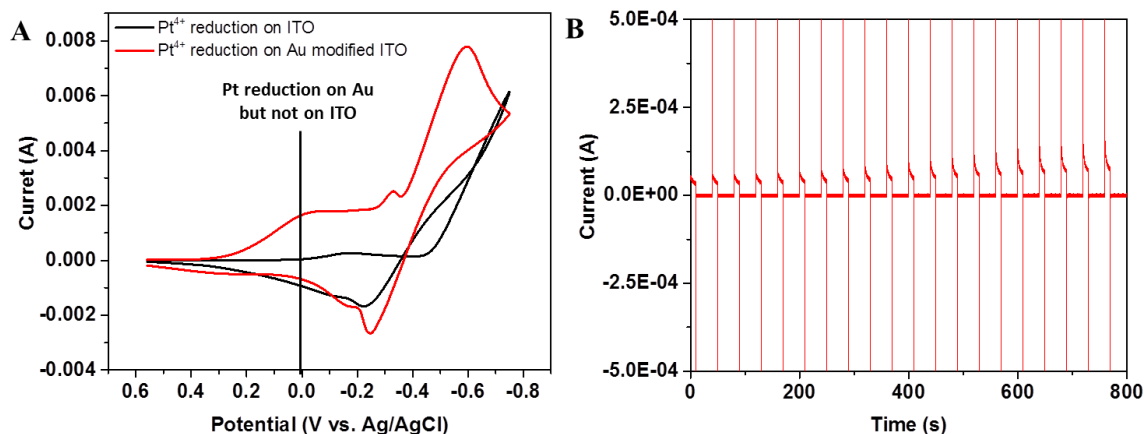


Figure 4.1: (A) Cyclic voltammograms of 3 mM H_2PtCl_6 on bare ITO and Au-modified ITO (Scan rate: 0.1 V s^{-1}). (B) Chronoamperometric deposition of Pt NPs on Au-modified ITO substrate for 20 cycles.

Figure 4.2 shows the SEM images and the particle size distribution of Au-ITO, Au@Pt(1) and Au@Pt(30) samples. The SEM images reveal that Pt is coated only onto the Au NPs and no residual Pt NPs are seen on the ITO surface. The surface roughness increases after Au-ITO sample was deposited by Pt, which indicates that Pt likely exists as agglomerated NPs on the surface of Au rather than a continuous layer. The calculated average particle sizes and the distributions are shown in the right panel of Figure 4.2. The average particle diameter for Au NPs on Au-ITO sample is 27.7 ± 4.8 nm. After one cycle of Pt deposition, the particle diameter increases to 31.9 ± 4.8 nm, which increases further to 37.8 ± 5.7 nm after 30 cycles of Pt deposition. The morphology of the Au@Pt(30) NPs was further characterized by HRTEM using electron-transparent lamellar cross-section of Au@Pt NPs/ITO sample. A single-tilt holder was used for the TEM analysis of the sample at an accelerating voltage of 200 kV. Figure 4.3A shows the lattice spacing of 2.35 Å and 2.21 Å for Au cores and Pt shells, respectively. These two lattice spacing correspond to the (111) planes of face-centered cubic Au and Pt, respectively,²⁴⁻²⁵ which suggests that the Au@Pt NPs with Au core and Pt shell were successfully prepared. From the HRTEM image, it could also be revealed that Pt exists not as continuous layer but as tiny NPs on the surface of Au, which corroborates the SEM observation. Figure 4.3B shows the HAADF-STEM image and cross-sectional EDS Mapping analysis, revealing the elemental composition and distribution of the Au@Pt structure. The analyzed area of the elemental mapping was a 50×50 square. The elemental mapping further demonstrates the core-shell feature of the nanoparticles that Pt was distributed over the entire surface of the Au NP with no obvious overlap with each other, which further supports the Au-Pt core-shell structure. It is worth mentioning here that the particle diameter of the analyzed NP is about 38, nm which agrees with the previous particle sizes and distribution investigations. Figure 4.4 shows the UV-vis

absorption study of freshly prepared Au-ITO and Au@Pt NPs. Absorbance spectrum of Au NPs reveals a plasmonic peak at 550 nm for ~28 nm Au NPs. The spectra of Au@Pt NPs keep the absorption feature of Au NPs, with the plasmonic peaks closer to 550 nm. However, the plasmonic peak gets wider with higher Pt loading. This suggests that the plasmonic feature of Au core is maintained, while Pt absorbing broader wavelength range than the Au in the UV-vis region, which results in wider peaks in the absorption spectra.

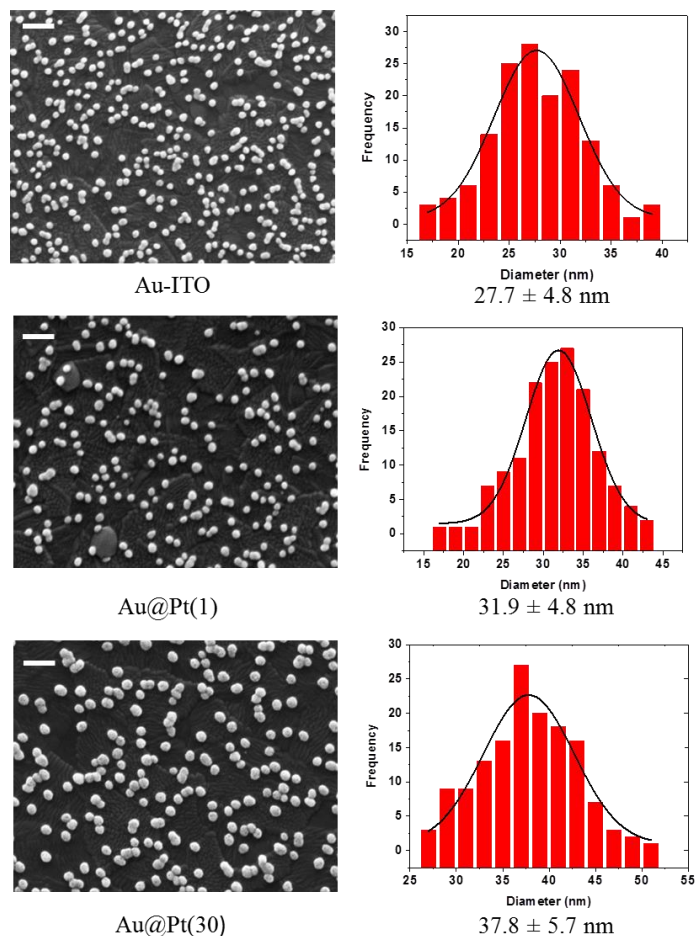


Figure 4.2: SEM images of Au-ITO, Au@Pt(1) and Au @Pt(30) and their particle sizes distribution analysis. The scale bar reads 100 nm.

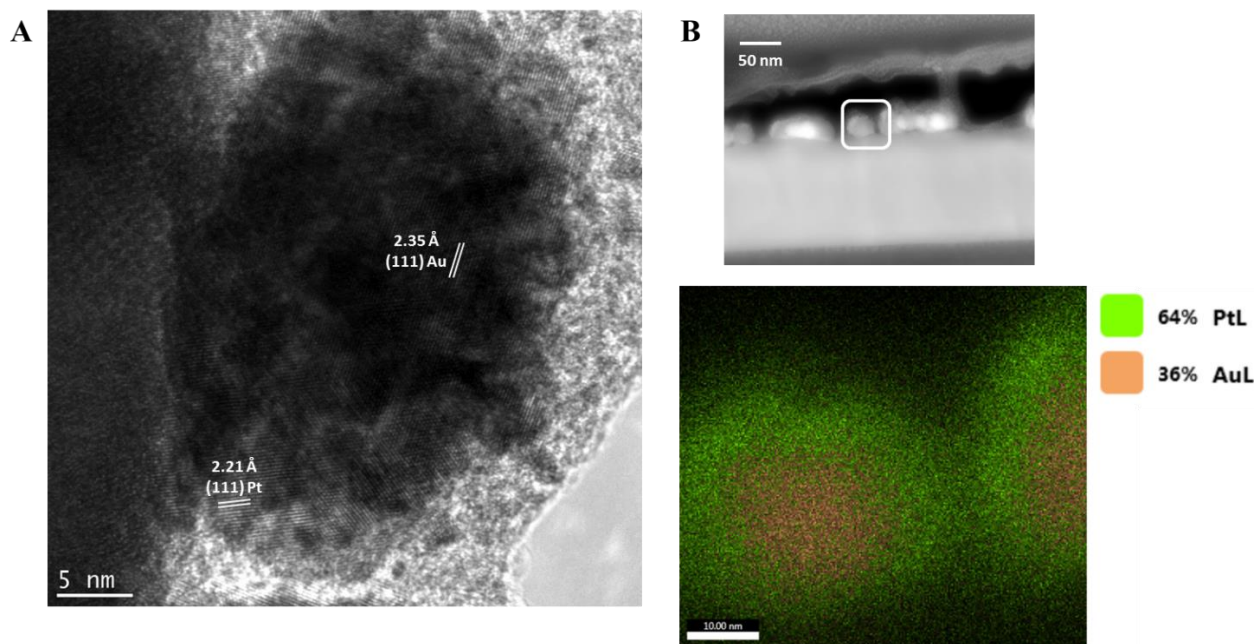


Figure 4.3: (A) HRTEM image of Au@Pt(30) sample with the Au core and Pt shell. (B) HAADF-STEM-EDS elemental mapping images of the same sample showing the Au-Pt core-shell structure.

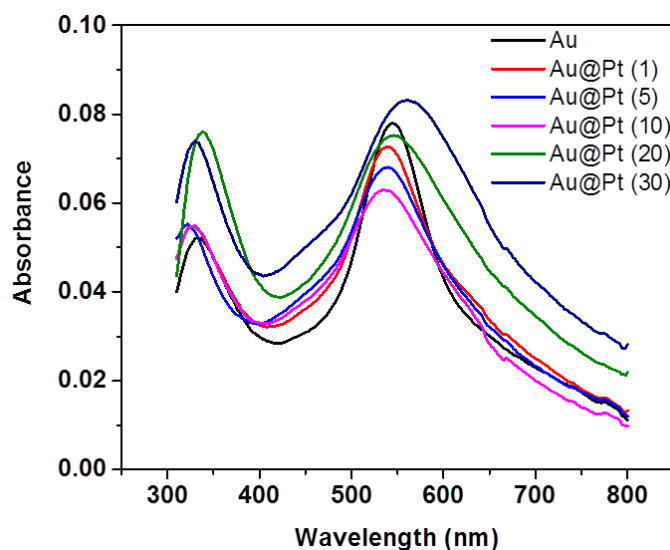


Figure 4.4: UV-vis absorption spectra of Au-ITO and Au@Pt NPs samples

4.4.2 CV and Light Scattering Spectroelectrochemistry Analysis of Methanol Oxidation

To investigate the electrocatalytic activity of the Au@Pt NPs, the electrochemical oxidation of methanol was performed on Au@Pt anode. Figure 4.5 exhibits the CVs of 0.5 M

methanol in 0.1 M NaOH solution on Au-ITO and Au@Pt NPs electrodes with different coverage of Pt at the scan rate of 0.1 V s^{-1} . Clearly, Au@Pt samples display different electrochemical performances than Au-ITO where the electrochemical oxidation of methanol is sluggish. An oxidation peak is observed at $\sim 0.1 \text{ V vs. Ag/AgCl}$ for Au@Pt NPs samples in the forward scan, which is attributed to the direct oxidation of methanol molecules on the electrode surface. The methanol oxidation peak shifts to the anodic direction with higher Pt coverage and reaches close to $0.2 \text{ V vs. Ag/AgCl}$ for Au@Pt(30) (highest studied Pt coverage). The oxidation current is also dramatically increased from Au@Pt(1) to Au@Pt(30) and reaches to a maximum current density of 4.5 mA . It is worth mentioning here that the methanol oxidation current for Au@Pt(20) and Au@Pt(30) NPs samples are equivalent, which indicates that the surface area of the two samples are close to each other. The symmetry of the oxidation peak also plays an important role. From Au@Pt(1) NPs through Au@Pt(30) NPs samples, the methanol oxidation peak transforms from symmetric to asymmetric. The sharp current drop from Au@Pt(10), Au@Pt(20) and Au@Pt(30) samples is believed to be due to the oxidation species that saturates and poisons the electrode surface. Another oxidation peak is observed at about $-0.25 \text{ V vs. Ag/AgCl}$ in the reverse scan, which could be assigned to the removal of adsorbed species that were not completely oxidized during the forward scan.²⁶⁻²⁷ The electrochemical stability of the Au@Pt (30) electrode was evaluated by a multi-cycle successive CV scan for 50 cycles, as shown in Figure 4.6. After 50 complete cycles of successive scanning, the curve shape remains unchanged, while the peak current at $\sim 0 \text{ V vs. Ag/AgCl}$ drops from -4 mA to -3 mA . In general, the 25% decrease in methanol oxidation current indicates relatively good stability of the Au@Pt samples with minimum amount of surface Pt undergoing corrosion or dissolution. Although the

successive CV test provides insight in the surface corrosion and dissolution, a long-term stability test is essential to achieve a systematic evaluation of a fuel cell.

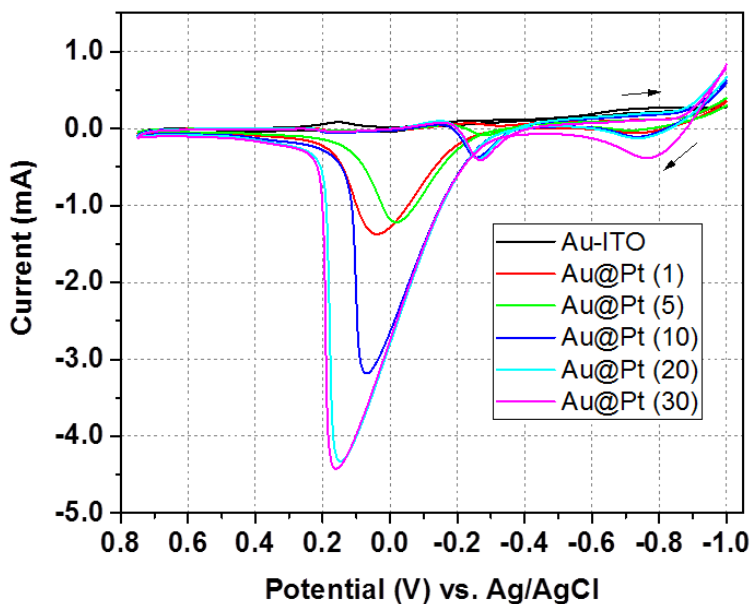


Figure 4.5: CVs of 0.5 M methanol in 0.1 M NaOH solution for Au-ITO and Au@Pt NPs samples. (Scan rate: 0.1 V s^{-1} ; Arrows indicate the scan direction.)

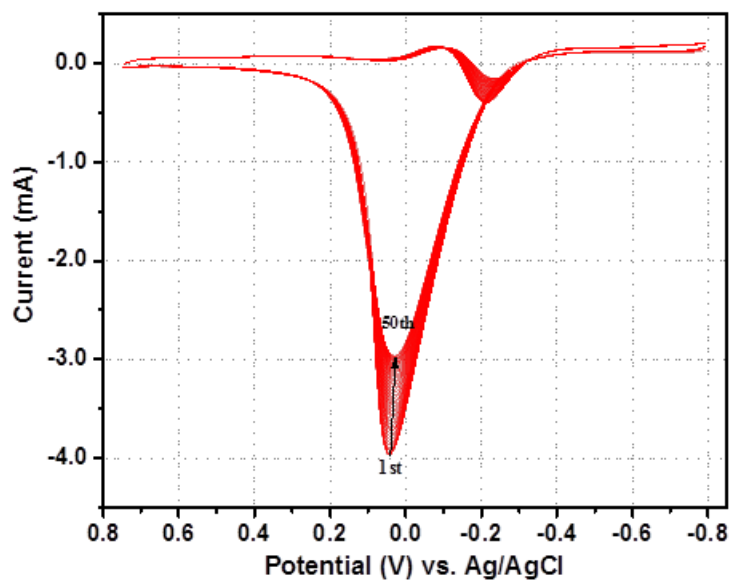


Figure 4.6: 50 successive CVs of the Au@Pt (30) sample in 0.5 M MeOH in 0.1M NaOH at a scan rate of 0.1 V s^{-1} .

Furthermore, a dark-field scattering setup was combined with the electrochemical method to reveal the surface state change during methanol oxidation (Figure 4.7A). The CVs of Au-ITO,

Au@Pt(1) and Au@Pt(30) NPs samples were obtained in 0.5 M methanol in 0.1 M NaOH electrolyte under the identical condition as previous. For Au NPs coated ITO sample (Figure 4.7B), the light scattering intensity dramatically decreases when the potential reaches 0 V vs. Ag/AgCl. This scattering intensity decrease is believed to be due to the oxidation of highly scattering Au NPs to less scattering Au-oxide as demonstrated in our previous study.^{22-23, 28} The scattering intensity was not reversely increased until the potential was scanned back to 0.3 V vs. Ag/AgCl where Au oxide was reduced back to Au. This Au oxidation behavior was minimized for Au@Pt(1) (Figure 4.7C) and Au@Pt(30) NPs (Figure 4.7D) samples. The light scattering shape for Au@Pt(1) and Au-ITO are still similar, however the intensity damping amplitude significantly decreases from 2×10^{-8} to 5×10^{-9} A. It can be explained that Au NPs were not fully covered by Pt for Au@Pt(1) sample so that the remaining surface of Au was oxidized and reduced back to Au in the potential window, but the Au oxidation was minimized as the amount of Au surface was limited. The dark-field scattering behavior for Au@Pt(30) NPs under the same condition appears differently than Au-ITO or Au@Pt(1) NPs. The drop in the scattering intensity at 0.2 V vs. Ag/AgCl is caused by methanol oxidization, indicating that the oxidized species have a lower scattering capability than Au@Pt NPs. The intensity damping at 0.2 V vs. Ag/AgCl becomes more pronounced at higher Pt coverage because of the higher concentration of oxidized species at electrode surface. In addition, the surface-bound Pt NPs clearly prevent the Au core from being oxidized. As a control experiment, the CVs and scattering intensity curves were recorded under the same potential window in 0.1 M NaOH electrolyte without methanol (Figure 4.8). In the electrolyte without methanol, Au-ITO shows Au oxidation feature for light scattering, whereas this feature is minimized on the Au@Pt(1) NPs and totally disappeared on the

Au@Pt(30) NPs sample. The control experiment further reveals that the surface-bound Pt NPs protect the Au core from oxidation.

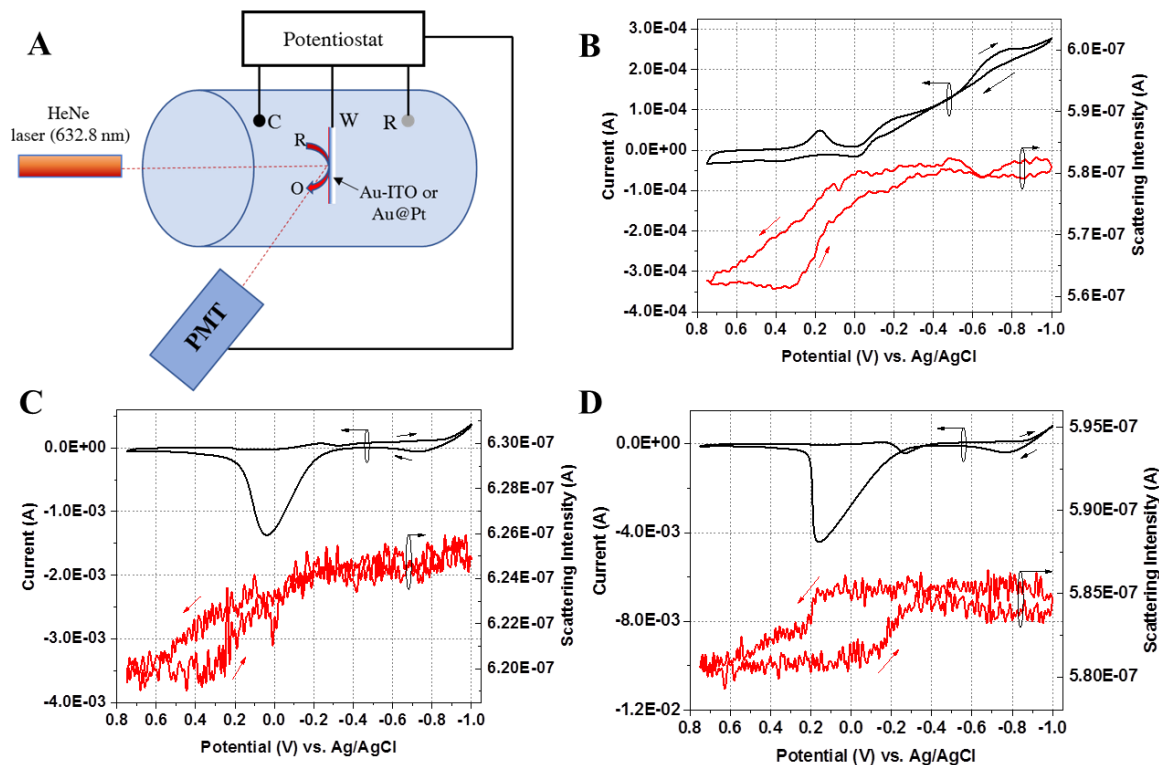


Figure 4.7: (A) Experimental setup for in-situ dark-field scattering spectroelectrochemistry study. CVs and dark-field scattering responses of methanol oxidation on Au-ITO (B), Au@Pt(1) (C) and Au@Pt(30) NPs (D) substrates.

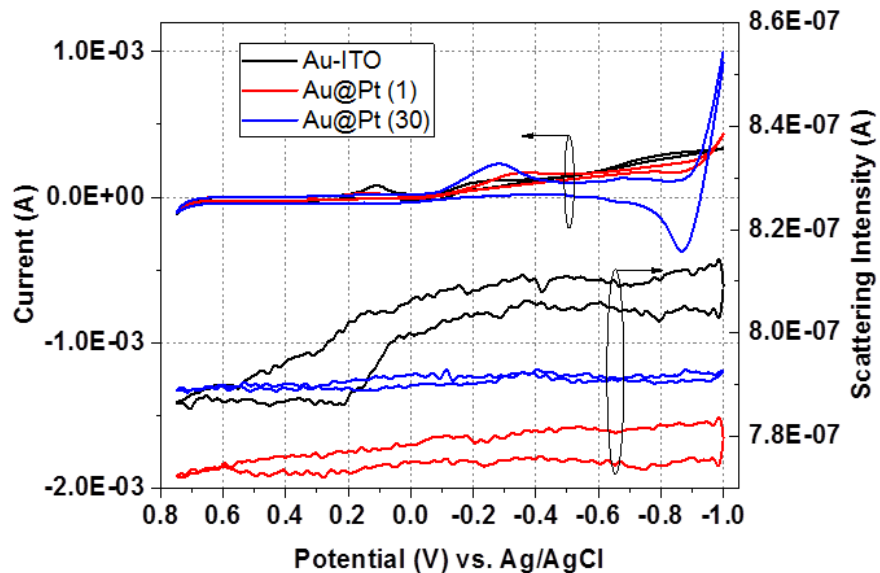


Figure 4.8: CVs and dark-field scattering responses of Au-ITO, Au@Pt(1) and Au@Pt(30) NPs in 0.1 M NaOH electrolyte without methanol recorded at the scan rate of 0.1 V s^{-1} .

4.4.3 CV and Light Scattering Spectroelectrochemistry Analysis of Formic Acid Oxidation

To further evaluate the electrocatalytic activity of Au@Pt NPs, we explored the activity towards formic acid oxidation reaction for different Pt thicknesses. Figure 4.9A shows the CVs of Au-ITO and Au@Pt NPs electrodes in 0.1 M H₂SO₄ electrolyte containing 0.1 M formic acid at a scan rate of 0.05 V s⁻¹. Formic acid oxidation is inactive on Au-ITO NPs. However, the Au@Pt NPs show dramatically enhanced electrocatalytic activity towards formic acid oxidation. This reaction occurs according to two parallel pathways: direct oxidation to CO₂ and indirect oxidation to CO_{ads}, then the CO_{ads} is further oxidized to CO₂.²⁹⁻³¹ In the study of Jeong and Kim,³² in situ SERS measurements are performed for Pt modified dendritic Au rod samples. When Pt exists as island-type layers, there is minimal CO_{ads} produced on the surface and the adsorption strength between CO_{ads} and Pt is quickly weakened as potential is scanned to positive direction, thus enables the direct oxidation of formic acid. With monolayer of Pt or above, the direct oxidation of formic acid is almost terminated by the CO_{ads} initially produced by the dehydration of formic acid at open circuit potential. During the forward scan, there are two oxidation peaks that could be resolved as the Pt coverage increases. The first peak around 0.2 V vs. Ag/AgCl is related to the oxidation of formic acid into CO₂ via direct oxidation pathway, while the second peak around 0.5 V vs. Ag/AgCl represents the indirect oxidation via CO_{ads} intermediate. CO_{ads} is produced by the dehydration of formic acid, which is the dominant reaction at higher Pt coverage [Au@Pt(20) and Au@Pt(30)]. At lower Pt coverage [Au@Pt(1), Au@Pt(5) and Au@Pt(10)], the direct oxidation to CO₂ is favored. During reverse scan, an oxidation peak appears around 0.2 V vs. Ag/AgCl for Au@Pt(30) NPs sample indicating the oxidation of CO_{ads} to CO₂, which strips off CO_{ads} species from the electrode surface. The dark-field scattering response of formic acid oxidation reaction was also recorded, as shown in Figure

4.9B. The Au oxidation feature could still be resolved for Au-ITO and Au@Pt(1) NPs samples, whereas it is terminated by higher coverage of surface-bound Pt NPs. In contrast with methanol oxidation, the light scattering response is not sensitive to the formic acid oxidation.

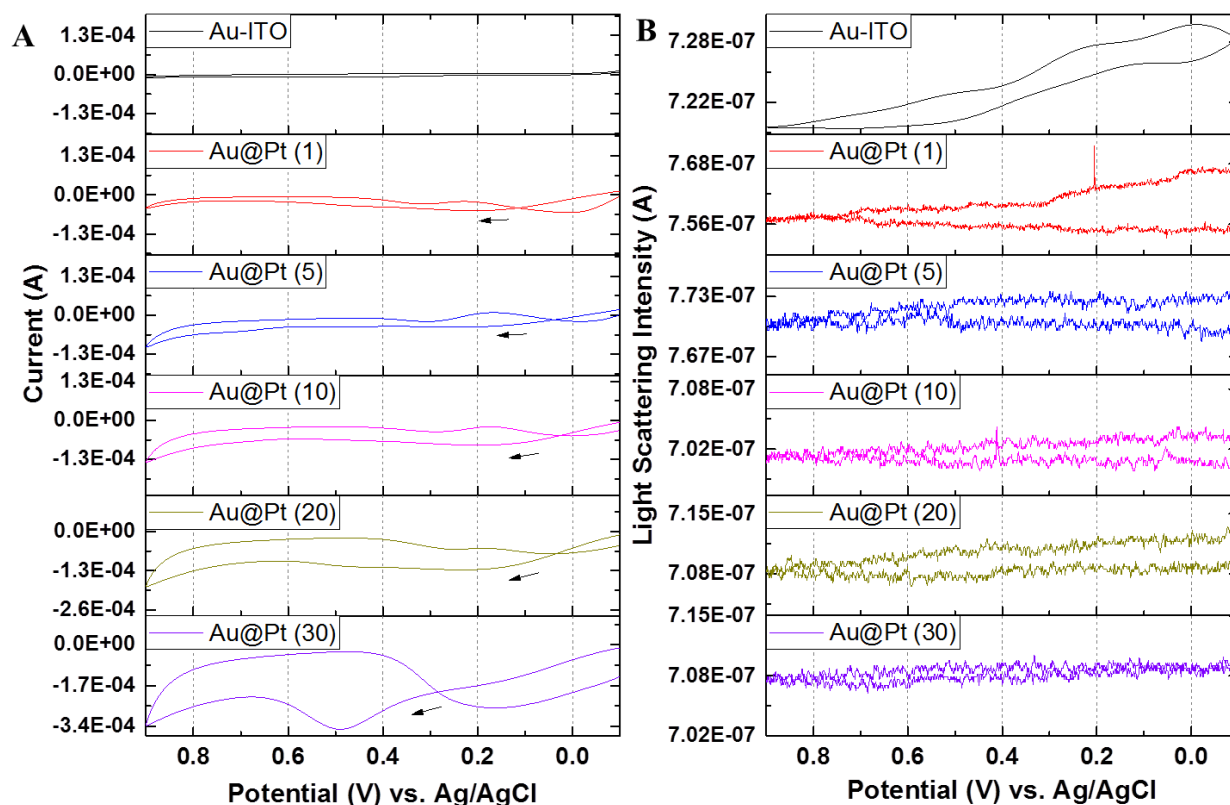


Figure 4.9: CVs (A) and dark-field scattering response (B) of Au-ITO and Au@Pt NPs in 0.1 M H_2SO_4 electrolyte containing 0.1 M formic acid at the scan rate of 0.05 V s^{-1} .

4.5 Conclusions

In conclusion, Au-ITO NPs electrode was further modified by Pt to form Au@Pt and Au-Pt core-shell structures using electrochemical deposition for methanol and formic acid oxidation reactions. The thickness of Pt layer was precisely controlled by varying the number of electrochemical deposition cycles. SEM, HRTEM and EDS mapping studies confirmed the Au-Pt core-shell structure. The Au@Pt NPs displayed desirable electrocatalytic activity for both methanol and formic acid oxidation than Au-ITO. The dark-field scattering

spectroelectrochemistry study of methanol oxidation reaction indicated that Au anodization became weaker and was terminated with increasing Pt thicknesses. The electrochemical oxidation of formic acid showed that lower coverage of surface-bound Pt NPs preferred the direct oxidation pathway to CO₂ while higher Pt coverage produced the CO_{ads} intermediate species, which eventually poisoned the electrode surface.

4.6 References

1. Jia, J.; Cao, L.; Wang, Z., Platinum-Coated Gold Nanoporous Film Surface: Electrodeposition and Enhanced Electrocatalytic Activity for Methanol Oxidation. *Langmuir* **2008**, *24*, 5932-5936.
2. Liang, D.; Gao, J.; Wang, J.; Chen, P.; Wei, Y.; Hou, Z., Bimetallic Pt—Cu Catalysts for Glycerol Oxidation with Oxygen in a Base-Free Aqueous Solution. *Catal. Commun.* **2011**, *12*, 1059-1062.
3. Suo, Y.; Hsing, I. M., Synthesis of Bimetallic PdAu Nanoparticles for Formic Acid Oxidation. *Electrochim. Acta* **2011**, *56*, 2174-2183.
4. Whittingham, M. S.; Savinell, R. F.; Zawodzinski, T., Introduction: Batteries and Fuel Cells. *Chem. Rev.* **2004**, *104*, 4243-4244.
5. Cuesta, A.; Cabello, G.; Gutiérrez, C.; Osawa, M., Adsorbed Formate: The Key Intermediate in the Oxidation of Formic Acid on Platinum Electrodes. *Phys. Chem. Chem. Phys.* **2011**, *13*, 20091-20095.
6. Grozovski, V.; Solla-Gullón, J.; Climent, V.; Herrero, E.; Feliu, J. M., Formic Acid Oxidation on Shape-Controlled Pt Nanoparticles Studied by Pulsed Voltammetry. *J. Phys. Chem. C* **2010**, *114*, 13802-13812.
7. Huang, X.; Zhao, Z.; Fan, J.; Tan, Y.; Zheng, N., Amine-Assisted Synthesis of Concave Polyhedral Platinum Nanocrystals Having {411} High-Index Facets. *J. Am. Chem. Soc.* **2011**, *133*, 4718-4721.
8. Tian, N.; Zhou, Z.-Y.; Sun, S.-G.; Ding, Y.; Wang, Z. L., Synthesis of Tetrahexahedral Platinum Nanocrystals with High-Index Facets and High Electro-Oxidation Activity. *Science* **2007**, *316*, 732.
9. Ahn, S. H.; Liu, Y.; Moffat, T. P., Ultrathin Platinum Films for Methanol and Formic Acid Oxidation: Activity as a Function of Film Thickness and Coverage. *ACS Catal.* **2015**, *5*, 2124-2136.

10. Gómez, R.; Pérez, J. M.; Solla-Gullón, J.; Montiel, V.; Aldaz, A., In Situ Surface Enhanced Raman Spectroscopy on Electrodes with Platinum and Palladium Nanoparticle Ensembles. *J. Phys. Chem. B* **2004**, *108*, 9943-9949.
11. Lin, Z.-H.; Shih, Z.-Y.; Tsai, H.-Y.; Chang, H.-T., Gold/Platinum Nanosponges for Electrocatalytic Oxidation of Methanol. *Green Chem.* **2011**, *13*, 1029-1035.
12. Stamenkovic, V. R.; Mun, B. S.; Arenz, M.; Mayrhofer, K. J. J.; Lucas, C. A.; Wang, G.; Ross, P. N.; Markovic, N. M., Trends in Electrocatalysis on Extended and Nanoscale Pt-Bimetallic Alloy Surfaces. *Nat. Mater.* **2007**, *6*, 241.
13. Sun, Y.; Hsieh, Y.-C.; Chang, L.-C.; Wu, P.-W.; Lee, J.-F., Synthesis of Pd₉Ru@Pt Nanoparticles for Oxygen Reduction Reaction in Acidic Electrolytes. *J. Power Sources* **2015**, *277*, 116-123.
14. Zhang, S.; Shao, Y.; Liao, H.-g.; Liu, J.; Aksay, I. A.; Yin, G.; Lin, Y., Graphene Decorated with Pt Alloy Nanoparticles: Facile Synthesis and Promising Application for Formic Acid Oxidation. *Green Chem.* **2011**, *23*, 1079-1081.
15. Liu, J.; Cao, L.; Huang, W.; Li, Z., Preparation of Aupt Alloy Foam Films and Their Superior Electrocatalytic Activity for the Oxidation of Formic Acid. *ACS Appl. Mater. Interfaces* **2011**, *3*, 3552-3558.
16. Su, S.; Zhang, C.; Yuwen, L.; Liu, X.; Wang, L.; Fan, C.; Wang, L., Uniform Au@Pt Core-Shell Nanodendrites Supported on Molybdenum Disulfide Nanosheets for the Methanol Oxidation Reaction. *Nanoscale* **2016**, *8*, 602-608.
17. Boxley, C. J.; White, H. S.; Lister, T. E.; Pinhero, P. J., Electrochemical Deposition and Reoxidation of Au at Highly Oriented Pyrolytic Graphite. Stabilization of Au Nanoparticles on the Upper Plane of Step Edges. *J. Phys. Chem. B* **2003**, *107*, 451-458.
18. Hezard, T.; Fajerweg, K.; Evrard, D.; Collière, V.; Behra, P.; Gros, P., Gold Nanoparticles Electrodeposited on Glassy Carbon Using Cyclic Voltammetry: Application to Hg(II) Trace Analysis. *J. Electroanal. Chem.* **2012**, *664*, 46-52.
19. Xu, C.; Geng, H.; Bennett, R.; Clayton, D. A.; Pan, S., Ti@TiO₂ Nanowire Electrode with Polydisperse Gold Nanoparticles for Electrogenenerated Chemiluminescence and Surface Enhanced Raman Spectroelectrochemistry. *J. Phys. Chem. C* **2013**, *117*, 1849-1856.
20. Shan, X., et al., Imaging the Electrocatalytic Activity of Single Nanoparticles. *Nat. Nanotechnol.* **2012**, *7*, 668.
21. Shan, X.; Wang, S.; Tao, N., Study of Single Particle Charge and Brownian Motions with Surface Plasmon Resonance. *Appl. Phys. Lett.* **2010**, *97*, 223703.
22. Ma, Y.; Highsmith, A. L.; Hill, C. M.; Pan, S., Dark-Field Scattering Spectroelectrochemistry Analysis of Hydrazine Oxidation at Au Nanoparticle-Modified Transparent Electrodes. *J. Phys. Chem. C* **2018**, *122*, 18603-18614.

23. Ma, Y.; Highsmith, A. L.; Pan, S., Dark Field Scattering Spectroelectrochemistry of Single Au Nanoparticles at Transparent Planar and Micro-Sized Electrodes. *ECS Trans.* **2018**, *85*, 1155-1162.
24. Shao, L.; Li, J.; Zhang, Y.; Gong, S.; Zhang, H.; Wang, Y., The Effect of the Reduction Extent on the Performance of Graphene/Poly(Vinyl Alcohol) Composites. *J. Mater. Chem. A* **2014**, *2*, 14173-14180.
25. Yuwen, L.; Xu, F.; Xue, B.; Luo, Z.; Zhang, Q.; Bao, B.; Su, S.; Weng, L.; Huang, W.; Wang, L., General Synthesis of Noble Metal (Au, Ag, Pd, Pt) Nanocrystal Modified Mos₂ Nanosheets and the Enhanced Catalytic Activity of Pd–Mos₂ for Methanol Oxidation. *Nanoscale* **2014**, *6*, 5762-5769.
26. Chen, Y., et al., A Facile Strategy to Synthesize Three-Dimensional Pd@Pt Core–Shell Nanoflowers Supported on Graphene Nanosheets as Enhanced Nanoelectrocatalysts for Methanol Oxidation. *Chem. Commun.* **2015**, *51*, 10490-10493.
27. Akinpelu, A.; Merzougui, B.; Bukola, S.; Azad, A.-M.; Basheer, R. A.; Swain, G. M.; Chang, Q.; Shao, M., A Pt-Free Electrocatalyst Based on Pyrolyzed Vinazene–Carbon Composite for Oxygen Reduction Reaction. *Electrochim. Acta* **2015**, *161*, 305-311.
28. Wusimanjiang, Y.; Ma, Y.; Lee, M.; Pan, S., Single Gold Nanoparticle Electrode for Electrogenerated Chemiluminescence and Dark Field Scattering Spectroelectrochemistry. *Electrochim. Acta* **2018**, *269*, 291-298.
29. Cuesta, A.; Cabello, G.; Osawa, M.; Gutiérrez, C., Mechanism of the Electrocatalytic Oxidation of Formic Acid on Metals. *ACS Catal.* **2012**, *2*, 728-738.
30. Gao, W.; Mueller, J. E.; Jiang, Q.; Jacob, T., The Role of Co-Adsorbed Co and OH in the Electrooxidation of Formic Acid on Pt(111). *Angew. Chem. Int. Ed.* **2012**, *51*, 9448-9452.
31. Joo, J.; Uchida, T.; Cuesta, A.; Koper, M. T. M.; Osawa, M., Importance of Acid–Base Equilibrium in Electrocatalytic Oxidation of Formic Acid on Platinum. *J. Am. Chem. Soc.* **2013**, *135*, 9991-9994.
32. Jeong, H.; Kim, J., Insights into the Electrooxidation Mechanism of Formic Acid on Pt Layers on Au Examined by Electrochemical Sers. *J. Phys. Chem. C* **2016**, *120*, 24271-24278.

CHAPTER 5

PHOTOELECTROCHEMICAL PERFORMANCE OF Au-INCORPORATED HEMATITE FOR SOLAR WATER SPLITTING: SECM AND BULK STUDY

5.1 Abstract

Au-incorporated hematite photoanode was screened for photoelectrochemical water oxidation by scanning electrochemical microscope (SECM) technique with a scanning probe of optical fiber for visible light irradiation of the photoanode substrate. Au-incorporated hematite exhibited an enhancement in photocurrent for up to 3% of Au and the performance drop was observed with 4-10% of Au. Subsequently, pristine and Au-incorporated hematite thin film photoanodes were fabricated by spin coating method with optimal precursor concentrations of Au and $\text{Fe}(\text{NO}_3)_3$ to confirm the results of SECM. The photoelectrochemical (PEC) response confirms that 3% Au is optimum for efficient water oxidation from Au-hematite photoanode. The pristine and Au-hematite materials were also characterized by scanning electron microscopy (SEM) and X-ray photoelectron spectroscopy (XPS) techniques. Au was found to exist in the form of embedded nanoparticles in the incorporated hematite nanostructures. Mott-Schottky analysis of the bulk samples confirms an improvement in charge carrier density for Au-doped hematite. Additionally, there was little plasmonic enhancement as evidenced by UV-vis spectroscopy, with a minimal contribution towards photoactivity. Surface generation tip collection mode of SECM was performed to quantify the generation of oxygen. Oxygen reduction current increases with the increase of photocurrent and reached at 4.75 nA for 3% Au-

hematite sample. Thus, the enhanced water splitting performance by Au is attributed to enhancing the electronic conductivity of hematite film.

5.2 Introduction

Photoelectrochemistry provides promising applications in electric power and renewable energy generation by using solar energy.¹⁻³ Solar cells are the best example for the direct production of electricity.⁴⁻⁶ Photoelectrochemical (PEC) water splitting using sunlight has been intensively studied for sustainable generation of hydrogen fuel since the discovery of electrochemical photolysis on TiO₂.⁷⁻¹¹ Many photocatalysts especially metal oxides have been focused for solar energy driven water splitting reactions because of their suitable band gap and visible light absorptivity.¹²⁻¹⁵ Negishi *et al.*¹⁶ developed BaLa₄Ti₄O₁₅ loaded by Au₁₅ for enhancing the water splitting efficiency. In their work, the photocatalytic activity was improved by 19 times under an optimized coverage of the Cr₂O₃ shell. Recently, Co-doped BiVO₄ has been developed as a promising anode material for improved water oxidation due to the great enhancement of conductivity by Co doping.¹⁷

n-Type semiconductor hematite (α -Fe₂O₃) has been considered as a prospective photocatalyst material of choice for solar water oxidation due to its good stability, absorption in the visible region, low cost, and the favorable band gap of ~ 2.2 eV.¹⁸⁻²² However, its low conductivity and short hole diffusion length are the major limiting factors that dictate the photoactivity of hematite. To overcome these demerits, several efforts have been made, including surface passivation,²³⁻²⁶ nanostructuring,²⁷⁻³⁰ heterojunction³¹⁻³² and doping with higher conductive materials.³³⁻³⁷ Different doping materials have been utilized to help enhance the photocatalytic efficiency of hematite. For example, Pt, Pd, Ta, Au, and Ag, have been incorporated into the powdered and thin film hematite to suppress the charge recombination and

to promote the charge-transfer processes of photogenerated electrons and holes at the photocatalyst/electrolyte interfaces.³⁸⁻⁴⁰ In the previous studies,⁴¹⁻⁴² Au nanoparticles (NPs) and Au nanorods (NRs) have been successfully incorporated in hematite thin films to improve the photoactivity for solar water splitting. It was discovered that Au NPs deposited underneath the hematite film increased the chances of light absorption in the visible region, thereby leading to maximizing the photogenerated charge carriers in the film for enhanced water splitting reaction. Furthermore, the decoration of Au NRs on top of hematite thin film electrode using electrostatic forces exhibited a plasmon enhancement towards water oxidation at higher bias potentials and resonance plasmon wavelengths. Recent literature on Au-decorated hematite photoanode for solar water splitting is summarized in Table 5.1. Among these representative works, the major contributions to enhance the photoactivity of hematite are efficient charge separation; improved bulk charge transport; and plasmonic enhancement. Although few studies reveal the optimum doping percentage for Au in hematite photocatalysts, it is not clear how much Au is optimum. One of the best approaches to identify the doping in photocatalysts is to utilize a rapid screening and optimizing technique called scanning photoelectrochemical microscopy (SECM) with a scanning optical fiber. In this SECM technique operation mode, the light through an optical fiber is used to illuminate individual spots on a photocatalyst array and the resulting photocurrent response is recorded from each scanned area including the photocatalyst spots that have different composition or structure.⁴³⁻⁴⁴ Jang *et al.*⁴⁵ studied the photoactivity of Ag-hematite nanocomposite by SECM for water oxidation with different compositions of Ag and Fe. Such composite hematite was further doped with Sn and found the optimum condition for water oxidation with 50%-50% Ag-Fe and 2% Sn. In the follow-up study,⁴⁰ Ta-doped hematite was investigated by SECM yielding ~32 times increment in photocurrent by 2% of Ta doping as

against pristine sample. The preferential growth of Ta along the (001) facet of hematite greatly improved the conductivity of the film thereby enhancing the photoactivity. Recently, Conzuelo and coworkers⁴⁶ utilized the SECM technique to provide information about the local photocurrent generated at photocatalysts surfaces. In their modified approach, the tip microelectrode coupled with an optical fiber was used for both irradiation and electrochemical probe. The high-resolution analysis was performed for TiO₂ and BiVO₄ photoanodes with X, Y grid increment of 20 μm.

#	Sample preparation method	PEC performance	Major contribution	Reference #
1	Nanosphere lithography (Au nanohole array pattern)	$J_{photo} = 0.92 \text{ mA cm}^{-2}$ @1.23 V vs. RHE in 1 M NaOH	The enhancement of light collection and the LSPR	<i>Nat. Commun.</i> ⁴⁷
2	Sputtered (10% Au-90% Ag) as a reflector	$J_{photo} = 1.44 \text{ mA cm}^{-2}$ @1.23 V vs. RHE in 1 M NaOH (pH = 13.6)	Maximizing the light absorption of hematite	<i>Adv. Mater.</i> ⁴⁸
3	Spin-coated (Au-Pt core-shell NPs)	$J_{photo} = 0.83 \text{ mA cm}^{-2}$ @1.23 V vs. RHE in 0.5 M Na ₂ SO ₄ (pH = 7)	Effectively promote the charge separation of hematite	<i>Dalton Trans.</i> ⁴⁹
4	Immersed in 5 mM HAuCl ₄ solution by “top-down” method	$J_{photo} = 3.2 \text{ mA cm}^{-2}$ @1.23 V vs. RHE in 1 M KOH (pH = 13.6)	Efficient electron and hole pair separation	<i>Nano Energy</i> ⁵⁰
5	Embedded Au in porous hematite by pulse reverse electrodeposition	$J_{photo} = 1.025 \text{ mA cm}^{-2}$ @1.23 V vs. RHE in 1 M NaOH	Bulk charge transport and improved surface plasmonic absorption	<i>Chem. Commun.</i> ³⁹
6	Annealing and evaporation of thin Au films which led to dewetting	$J_{photo} = 0.5 \text{ mA cm}^{-2}$ @1.23 V vs. RHE in 1 M NaOH	Enhancement in absorption in the visible range	<i>J. Phys. Chem. C</i> ⁵¹

7	Au NPs on hematite by a co-precipitation technique	$J_{photo} = 0.21 \text{ mA cm}^{-2}$ @1.23 V vs. RHE in 1 M NaOH	Fermi level equilibration and surface catalysis	<i>J. Mater. Res.</i> ⁵²
8	Solution chemistry decoration of Au NPs onto hematite nanoflake	$J_{photo} = 1.0 \text{ mA cm}^{-2}$ @1.23 V vs. RHE in 1 M KOH (pH = 13.6)	Narrow-band-absorption enhancement in the visible region	<i>ChemSusChem</i> ⁵³
9	Dropwise deposition of Au NPs on hematite NRs array	$J_{photo} = 0.13 \text{ mA cm}^{-2}$ @1.23 V vs. RHE in 0.5 M Na ₂ SO ₄	LSPR electromagnetic field enhancement	<i>Nanoscale</i> ⁵⁴
10	Sandwiched Au/Zr-Fe/Au structure by electrodeposition on ITO	$J_{photo} = 0.3 \text{ mA cm}^{-2}$ @1.23 V vs. RHE in 1 M NaOH (pH = 14)	Plasmonic layers and efficient movement of charge carriers	<i>J. Power Sources</i> ⁵⁵
11	Drop-cast loading of pre-synthesized Au NPs on Ti-Fe ₂ O ₃ NRs	$J_{photo} = 1.5 \text{ mA cm}^{-2}$ @1.23 V vs. RHE in 1 M NaOH (pH = 13.6)	Plasmonic resonance energy transfer and relaxed Fermi-level pinning by surface passivation	<i>ChemSusChem</i> ⁵⁶
12	Spin-coating (HAuCl ₄) on electron beam evaporation prepared hematite	$J_{photo} = 1.75 \text{ mA cm}^{-2}$ @1.23 V vs. RHE in 1 M NaOH (pH = 13.6)	Plasmonic and facilitating surface charge transfer	<i>ChemCatChem</i> ⁵⁷
13	Chemical spray pyrolysis (α -Fe ₂ O ₃ /Au/ZnO)	$J_{photo} = 0.05 \text{ mA cm}^{-2}$ @1.23 V vs. RHE in 0.5 M NaOH	Reduced charge transfer resistance, fast charge transfer kinetics and SPR.	<i>Sol. Energy Mater. Sol. Cells</i> ⁵⁸

* J_{photo} is the photocurrent density in mA cm^{-2} ; RHE represents reversible hydrogen electrode; LSPR is localized surface plasmon resonance.

Table 5.1: Recent literature on Au decorated hematite photoanode for solar water splitting.

Herein, we present the screening of photocatalytic Au-incorporated hematite for solar water oxidation by SECM with a scanning optical fiber. There are no prior studies pertaining to SECM study of Au-incorporated hematite, although there are reports on hematite doped with other dopants. The SECM in our work is followed by PEC performance testing on the as-prepared thin film electrodes based on the SECM results. Substrate generation tip collection

mode of SECM is used to quantitatively measure the generated oxygen from hematite surfaces. This study suggested that Au exists in the form of well distributed and embedded NPs into the hematite film. Au greatly contributed to the electronic conductivity of hematite film. These findings are supported by surface characterization techniques and capacitance measurements.

5.3 Experimental

5.3.1 Reagents and Materials

Iron (III) nitrate nonahydrate ($\text{Fe}(\text{NO}_3)_3 \cdot 9\text{H}_2\text{O}$) and ethylene glycol ($\text{HOCH}_2\text{CH}_2\text{OH}$, 99+%) were purchased from Acros Organics. Hydrogen tetrachloroaurate (III) hydrate (HAuCl_4 , 99.9%-Au) was obtained from Strem Chemicals. Sodium hydroxide (beads) was purchased from Ward's Science. All chemicals were used as received without further purification. All the solutions were freshly prepared using high-purity deionized water (Resistivity $>18 \text{ M}\Omega \cdot \text{cm}$). The commercially available conducting substrates, such as titanium (0.05 cm thick) and fluorine-doped tin oxide (FTO, $15\text{-}20 \text{ }\Omega \cdot \text{cm}^{-1}$, Pilkington, Toledo, OH) in $1 \text{ in} \times 1 \text{ in}$ dimension were used for both SECM studies and preparing thin film photoanodes for PEC measurements.

5.3.2 SPECM Screening of the 10×10 Photocatalyst Array Spots

A 10×10 array of Au-incorporated hematite photocatalysts was prepared using a method described in our previous work.¹⁷ Briefly, 0.1 M $\text{Fe}(\text{NO}_3)_3$ and 0.01 M HAuCl_4 solution was prepared in ethylene glycol (EG) and filtered using a $0.450 \text{ }\mu\text{m}$ PTFE syringe filter prior to dispensing. A picoliter (pL) dispenser (Austin, TX) was used to dispense the 10×10 array spots on a pre-cleaned Ti substrate with top and bottom three rows to be pristine $\text{Fe}(\text{NO}_3)_3$ and middle four rows to be Au mixed spots. Controlled voltage pulses were applied to the jetting device of pL dispenser for obtaining a certain number of droplets. The concentration of Au was varied

from 1 to 10 droplets in the middle four rows which provided 1 to 10% of Au (atomic ratio) in hematite. After obtaining the array, the dispensed droplets of individual components (i.e Fe, Au and EG) were allowed to mix on a shaker at 500 rpm for 30 minutes and then dried at 40°C on a hot-plate for 2 h. Then the dried array sample was subsequently annealed in air at 500°C for 2 h, which was then converted oxide. A CHI 920D scanning electrochemical microscope (CHI Instruments, Inc., Austin, TX) was used for PEC measurements of the array samples. A Teflon electrochemical cell with a standard three-electrode configuration was used for SECM measurement as shown in Figure 5.1. The photocatalyst array-coated Ti as a working electrode was assembled at the bottom of the cell. The reference (*sat.* Ag/AgCl) and counter electrodes (Pt wire/coil) were placed above the arrays to make sure they do not obstruct the X-Y movement of optical fiber over the array of spots. The photocatalytic activity of the array of spots was tested under white light illumination via an optical fiber, which moved in X-Y direction with the help of programmed piezo-positioner/controller.

A 0.1 M NaOH solution was used as an electrolyte. When the optical fiber transmitted light onto the substrate where there is no photocatalytic spot, no water oxidation occurs. As the fiber moves over to a photocatalytic spot, the photogenerated holes react with the OH⁻ group to produce oxygen gas while the photogenerated electrons move to the substrate to complete the reaction thereby yielding a water oxidation photocurrent for a specific spot position on the array. The cumulative current at every position of the array was plotted. The higher the current higher the photocatalytic activity as can be seen with bright-colored spot images or with higher current intensity.

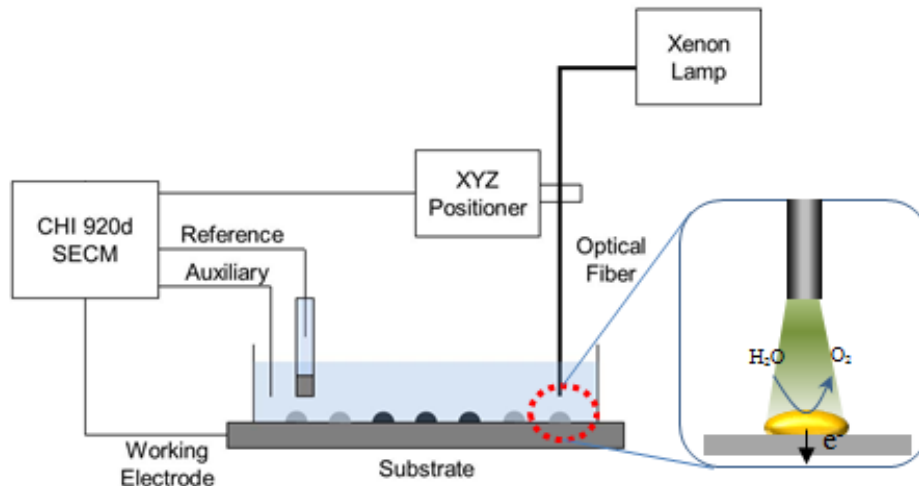


Figure 5.1: Schematic of the SECM system with synthesized array as substrate.

5.3.3 Fabrication of Bulk Au-incorporated Hematite Thin Film Photoelectrode

Once the optimum Au percentage was determined through SECM studies, pristine and Au-incorporated hematite films were prepared using the same precursors by the spin-coating method. The spin coating was conducted on a Laurell 650mz Spinner (Laurell Technologies). The spin speeds were 400 rpm for 5 s followed by 2500 rpm for 30 s for each layer. Each layer was dried at 60 °C on a hot plate before coating the next layer. 20 layers of pristine and Au-hematite films were coated onto pre-cleaned FTO substrates to obtain desired film thickness. The coated samples were then annealed at 500 °C for 2 h at the heating rate of 2 °C/min in air in a tube furnace. Hematite films incorporated with 0, 1, 3, 5 and 10% Au were prepared using the spin coating method and were tested for PEC measurement.

5.3.4 Characterization of Materials and Electrodes

The surface morphology and chemical composition of films were examined using a JEOL 700 scanning electron microscope (SEM) equipped with an energy dispersive X-ray spectrometer (EDS). The accelerating voltage for SEM was set to 20 kV. The UV-vis spectra

were obtained using an HP 8452A diode array UV-Vis spectrophotometer, recording spectra over the range 300-800 nm with a resolution of 2 nm. The chemical state and surface composition of the freshly-synthesized pristine and Au-modified iron oxide samples were examined by X-ray photoelectron spectroscopy (XPS) on a Kratos Axis Ultra DLD spectrometer equipped with a monochromatic Al K α X-ray source ($h\nu=1486.6$ eV) under ultra-high vacuum condition (at a base pressure of $< 8\times 10^{-10}$ Torr). The survey spectra were obtained in the binding energy (BE) range of 1200–0 eV at room temperature with an analyzer pass energy of 160 eV and an energy step size of 1 eV. High-resolution spectra in the region of interest were acquired with a pass energy of 20 eV and a step size of 0.1 eV. XPS data processing, including peak deconvolution, was performed using the XPS Peak-fit program with Shirley background subtraction and an iterative least-squares optimization algorithm. The adventitious hydrocarbon peak (C 1s line at 284.8 eV) was used as an internal standard to calibrate the binding energies of high resolution XPS spectra. Deconvolution of the C1s and O1s peaks was performed according to their chemical environments. The relative sensitivity factors (RSF) from Kratos library were used to obtain the relative concentration of the following elements: Sn3d (RSF = 7.875), Au4f (RSF = 6.25), Fe 3d (RSF = 2.957), O1s (RSF = 0.78), and C 1s (RSF =0.278). All PEC measurements were performed by a CHI 760C bipotentiostat (CH Instruments Inc., Austin, TX) in a three-electrode configuration. A three-neck quartz photo-reactor with a planar window was used to accommodate the thin film coated FTO working electrode, platinum wire counter electrode, and a Ag/AgCl (saturated with KCl) reference electrode. A standard simulated 1 sun (100 mW cm^{-2}) irradiation was provided by a solar simulator using a xenon lamp source (Oriel AM 1.5 filtered, Newport). The Mott-Schottky measurement was carried out in dark at an AC frequency of 1 kHz by sweeping a DC potential from -0.5 to 0.5 V vs. Ag/AgCl.

5.3.5 Substrate Generation Tip Collection SECM Measurements

The substrate generation tip collection mode of SECM measurements were conducted on a CHI 920D SECM (CH Instruments, Inc., Austin, TX). Hematite and 3% Au- incorporated hematite substrate were assembled in a home-made SECM cell with 0.59 cm² of surface area exposed to electrolyte. Pt wire and Ag/AgCl (sat. KCl) was used as counter and reference electrode, respectively. The schematic of substrate generation tip collection SECM setup is shown in Figure 5.2A. A 10 μm (in diameter) Pt disk microelectrode sealed in a glass capillary (Figure 5.2B and 5.2C) was used as the primary working electrode and the photoactive substrates as the secondary working electrodes. The Pt tip was held at a distance of 10 μm from the substrate. All electrodes were immersed in 0.1 M NaOH (pH 13.0) solution. The photoactive substrate was irradiated by a halogen fiber illuminator (Thorlabs, Inc.) at 1 sun irradiation. During the measurement, substrate potential was scanned from 0 to 0.8 V vs. Ag/AgCl at a scan rate of 0.1 V S⁻¹, while tip potential was kept at -0.4 V vs. Ag/AgCl. When the substrate generated O₂ diffused to the tip surface, it was collected and reduced to OH⁻ by the Pt tip.

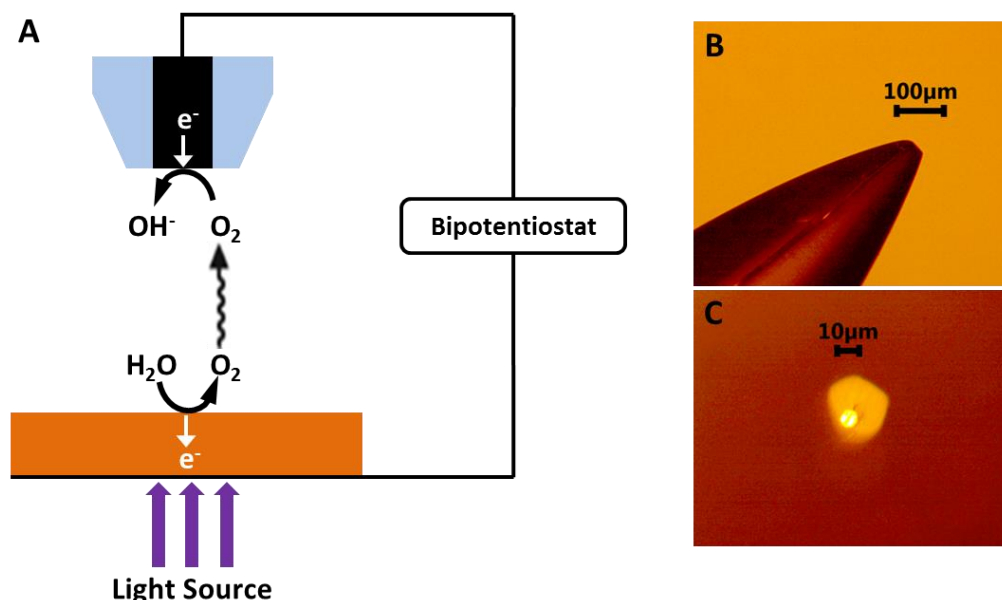


Figure 5.2: (A) Schematic of the substrate generation tip collection mode of SECM setup. Side (B) and top (C) view of the Pt disk microelectrode.

5.4 Results and Discussion

5.4.1 SECM for Searching Optimal Au Concentration of Hematite Photoanode

SECM screening technique is used to study the localized PEC activity of the photocatalyst array. Figure 5.3A shows the array design for studying the effects of Au on PEC of hematite spots produced by PL dispensing technique described in experimental. The top three rows and the bottom three rows of the ray were control spots containing only hematite in the absence of Au. This allows us to level the substrate and minimize the random errors caused by PL dispensing technique from droplet to droplet. The middle four rows are four replicates of the Au-incorporated spots with Au concentration varying from 0 to 10% from left to right in order to have average PEC response without reproducibility concerns of the dispensing technique. Figure 5.3B shows the two-dimensional SPCEM images of Au- incorporated hematite arrays prepared on Ti substrate with varying Au percentages at substrate potential equal to 0.3 V vs. Ag/AgCl. The applied potential to the sample array was varied as 0.3 and 0.5 V vs. Ag/AgCl and the raster scan of photocurrent was obtained with a scan step of 100 μm and a parking distance of 100 μm . It is clear from the SECM result that the improved photocurrent can be obtained with 1-3% of Au. The mixed Au has a negative effect on the photocurrent for 4-10% of Au. It is worth to mention that the background current is greatly eliminated with a higher potential applied (0.5 V vs. Ag/AgCl) as shown in Figure 5.3C because of more PEC current obtained than that at 0.3 V. We also obtained more pronounced Au incorporating effects at large substrate potential because of high PEC current response in the more positive potential bias. As shown in Figure 5.3D, the current from pristine and Au- incorporated hematite spots in their respective rows are averaged and plotted versus Au percentage. The plot clearly shows that the photocurrent response increases gradually with 1-3% Au and drops rapidly when the Au percentage increases to 4%.

Similarly, the array of spots of Au- incorporated hematite are prepared on FTO substrates, which shows that 1-3% of Au concentration is optimum to enhance the solar water oxidation performance for hematite photoanode. Based on the results from SECM study, 1, 3, 5, and 10% of Au were chosen to prepare the thin film photoanodes for testing the photoactivity for solar water splitting.

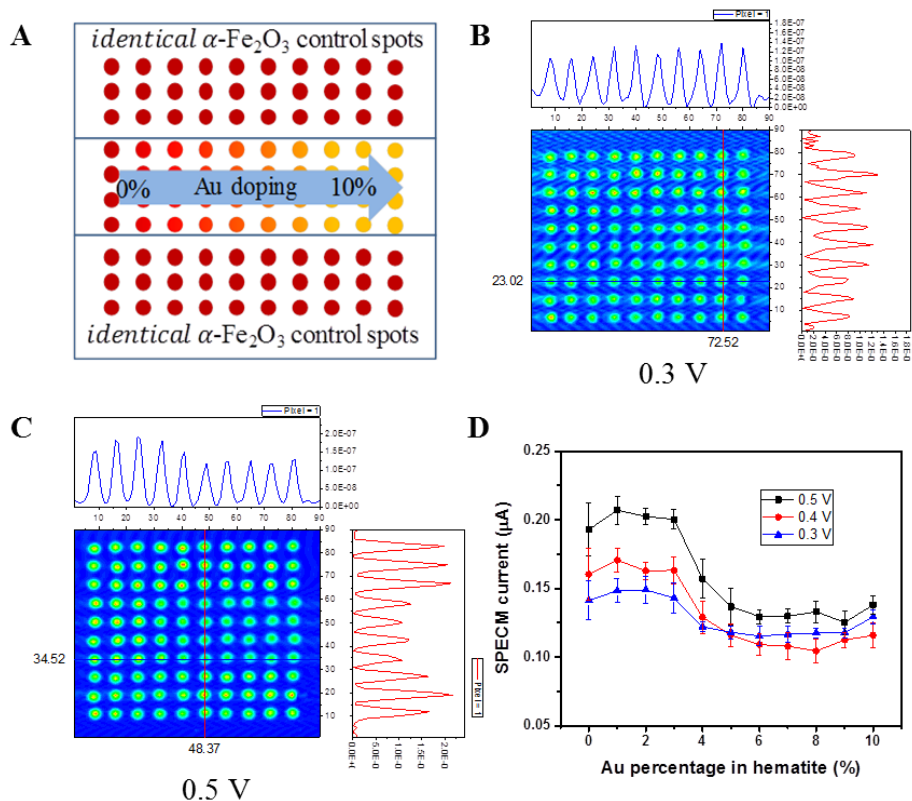


Figure 5.3: (A) The array design for studying Au effects on PEC of hematite spots produced by PL dispensing technique. SECM plots of Au- incorporated hematite array on Ti substrate obtained at substrate potentials of 0.3V (B) and 0.5 V (C) vs. Ag/AgCl. (D) Statistical averaging analysis of the PEC current dependence on Au percentage.

5.4.2 Absorption Spectra and Morphology of Au-incorporated Hematite Films

UV-vis absorption spectroscopy was performed for the spin-coated samples, as shown in Figure 5.4. The spectra were normalized to 400 nm for comparison. There is no obvious absorption improvement by Au in the wavelength region of 300 to 550 nm, where the major

contribution for absorption is hematite. From 550 to 800 nm, the absorption slightly increases with more Au percentage because of the absorption of the Au NPs. Thus, plasmonic enhancement by Au has a minimal contribution towards the photoactivity of hematite for water oxidation.

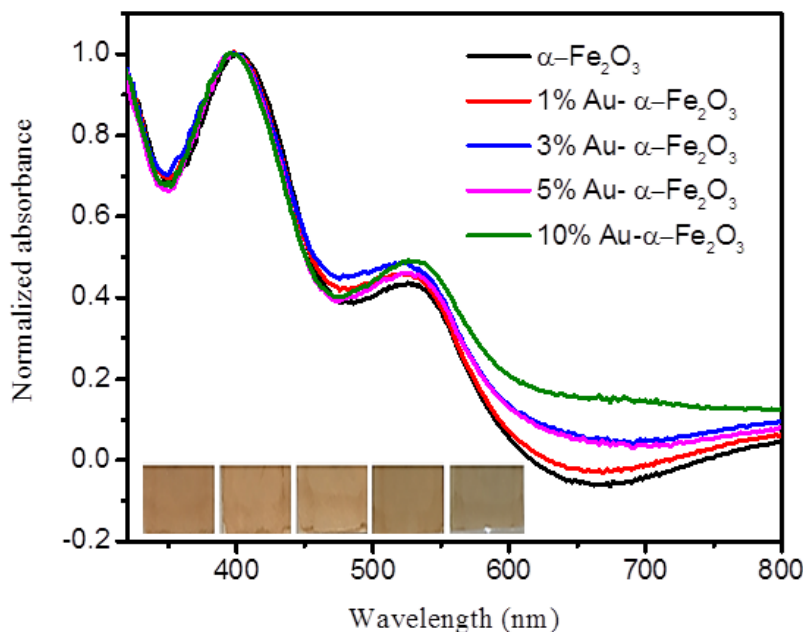


Figure 5.4: Normalized UV-vis spectra of pristine and Au-incorporated hematite photocatalysts incorporated with 1, 3, 5, and 10% of Au (atomic ratio). Inset: photographs of the listed samples.

To understand how Au modification on hematite film affect the PEC performance and its spatial distribution in a hematite film, Figure 5.5 shows the SEM analysis performed for the Au-incorporated hematite array for 1, 4, 7 and 10% of Au concentration in hematite. From the SEM images, it is evident that that Au exists as NPs and are evenly distributed in the photocatalysts with an average particle size of ~20 nm. The Au particles number increases with the increase of Au percentage and reaches a maximum at 10% Au concentration. With more Au NPs in the photocatalyst film, incident light is likely to be reflected and scattered by Au NPs and might not pass through and won't be absorbed by the hematite film. Thus, the photoactivity of 4-10% Au-

incorporated hematite samples was reduced. It could also be revealed from the SEM pictures that hematite films are continuous and homogeneous with the sample preparation method mentioned above. Figure 5.6 shows the cross-sectional SEM image of spin-coated Au-incorporated hematite thin films. The average Au-hematite film thickness is about 100 nm on a ~270 nm thickness FTO substrate, as shown in the figure.

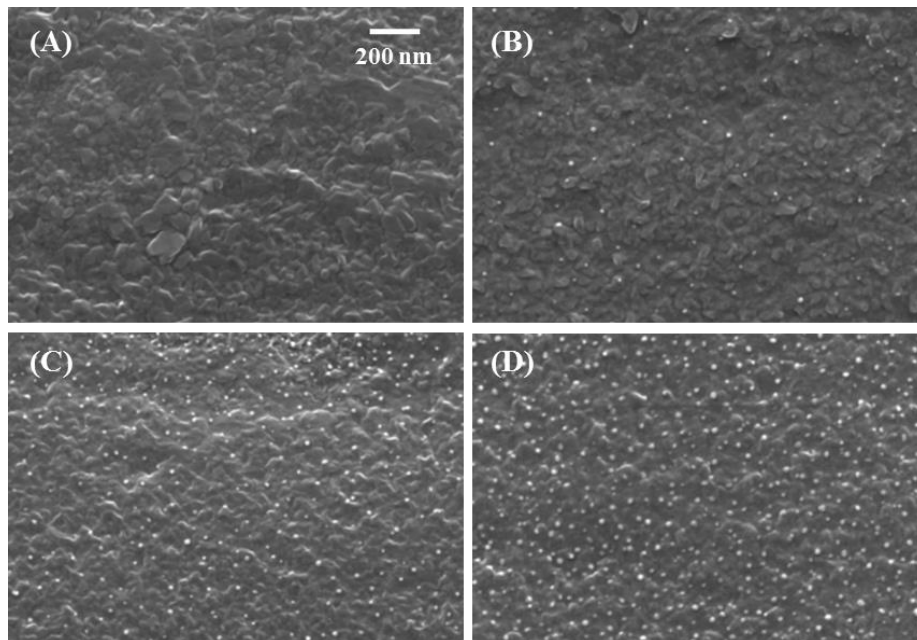


Figure 5.5: SEM images of Au-incorporated hematite thin film with 1% (A), 4% (B), 7% (C) and 10% (D) of Au in the film.

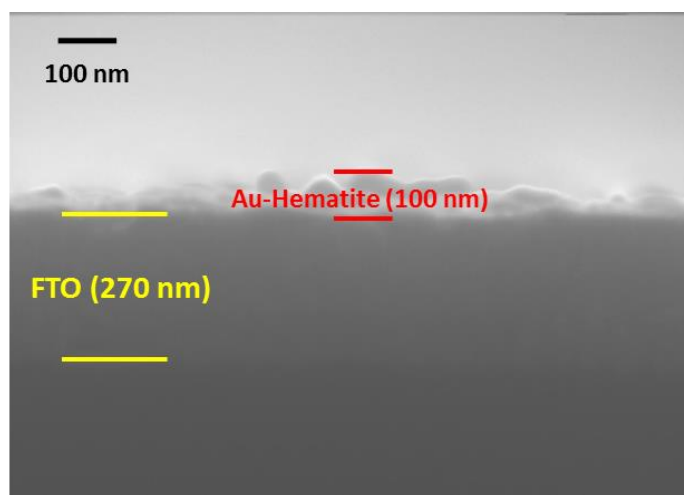


Figure 5.6: Cross-section SEM image of spin-coat Au-incorporated hematite film with an average thickness of 100 nm.

5.4.3 XPS Characterization of Au-incorporated Hematite Film

To understand the chemical identity of Au in the hematite sample, XPS analysis was performed for pristine and optimized 3% Au-modified Fe₂O₃ thin film samples prepared on FTO by spin coating method. Figure 5.7 shows the survey spectra of pristine and 3% Au-incorporated Fe₂O₃ samples. Survey spectra of both the samples reveal XPS lines of Sn, which has been reported previously by several researchers for the Fe₂O₃ films prepared on FTO (F:SnO₂). Sn diffuses from FTO substrate upon annealing the samples at temperatures $\geq 500^\circ\text{C}$.^{39, 59-61} The elemental compositions obtained for Fe2p, O1s, Sn3d and Au4f lines are listed in Table 5.2. The relative concentration of Au on the surface of hematite is only 1.3% compare to Fe, which is due to the presence of scattered Au 20-30 nm size nanoparticles as observed from SEM study previously (Figure 5.5). Figure 5.8 shows the high-resolution XPS spectra of the Fe2p, O1s, Sn3d, and Au4f lines for 3% Au-modified hematite film. As shown in Figure 5.8A, the Fe 2p_{3/2} BE peak at 709.91 ± 0.1 eV confirms the +3-oxidation state of Fe and the formation of hematite (α -Fe₂O₃) phase.⁶¹ The deconvoluted O1s peak demonstrates four types of oxygen species (Figure 5.8B). The O1s (Fe-O) peak at $\sim 529.81 \pm 0.1$ eV originates from the Fe₂O₃ moiety. The peaks O1s (O-Sn) at 531.01 eV is ascribed to Sn-oxide, which is formed due to diffusion of Sn⁴⁺ ions to the hematite surface from FTO. The O1s (O-C/O-H) peak at 531.93 eV and minor O1s (O-Si) peak at 533.04 eV are due to adsorbed carbonyl/hydroxyl groups and surface impurity, respectively. The Sn3d_{5/2} peak at 486.98 ± 0.1 eV and a spin-orbit splitting ($\Delta=8.4$ eV) of doublet lines for Sn3d spectrum confirms the presence of Sn⁴⁺ state (Figure 5.8C). The BE of Au4f_{7/2} peak at 83.97 ± 0.1 eV and spin-orbit splitting ($\Delta=3.7$ eV) of doublet lines for Au4f confirms that gold exists in metallic nanoparticles form on the surface of the hematite film (Figure 5.8D). The absence of any peak at 86 eV excludes the possibility of gold oxidation. As

seen from Table 5.2, the Sn content in pristine and Au-incorporated hematite films is almost identical (~0.2at%). Hence, the PEC performances of both pristine and Au-incorporated hematite should not be affected by Sn.

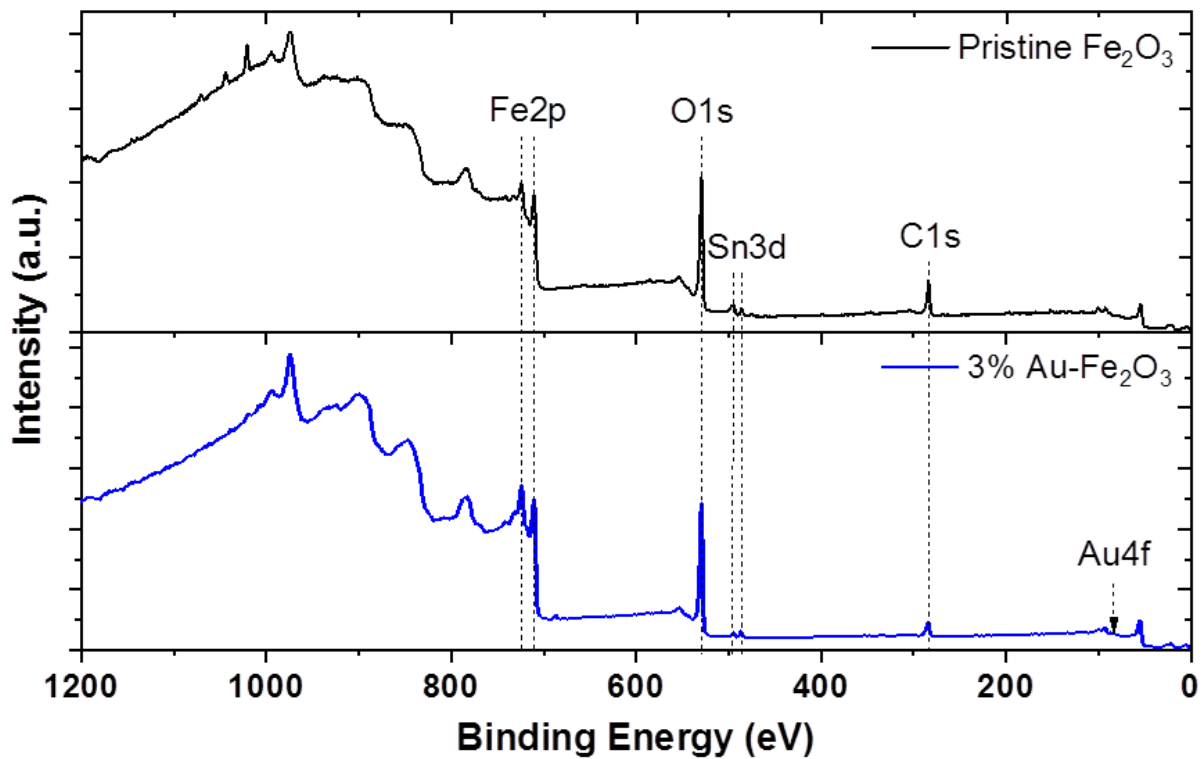


Figure 5.7: Survey XPS spectra of pristine and 3% Au-incorporated hematite samples on FTO.

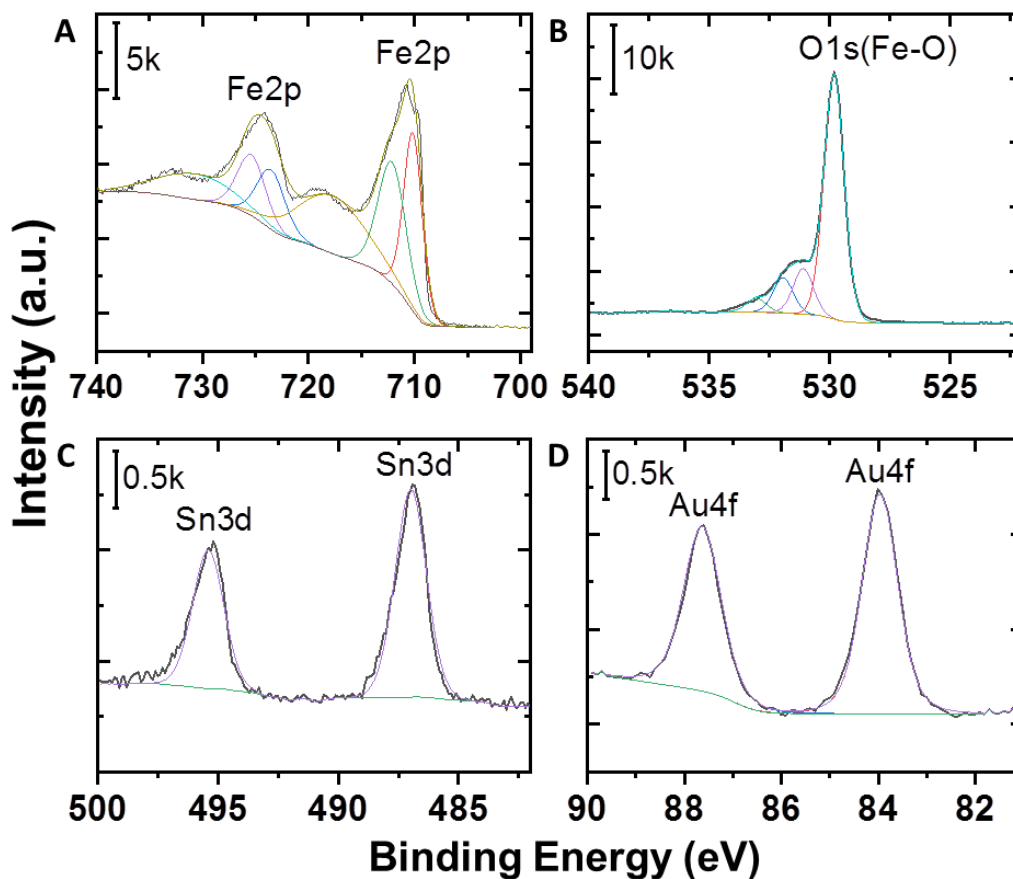


Figure 5.8: High-resolution XPS spectra of Fe2p, O1s, Sn3d and Au4f lines for 3% Au-incorporated hematite thin film.

Sample	XPS lines	B.E. (eV)	Rel. Conc. (At%)
Pristine Hematite	Fe 2p	709.91	37.35
	O 1s	529.91	62.45
	Sn 3d	486.91	0.20
	Au 4f	--	--
3% Au-Hematite	Fe 2p	709.91	38.26
	O 1s	529.91	61.03
	Sn 3d	486.91	0.22
	Au 4f	86.91	0.49

Table 5.2: Quantification of Fe, O, Sn and Au elements in pristine and 3% Au-incorporated hematite samples.

5.4.4 PEC Characterization of Au-incorporated Hematite Thin Film Photoanodes

The results of the above SPECM study suggested that both increase and decrease in hematite's PEC performance can be obtained by carrying Au percentage. In particular, PEC performance enhancement can be obtained at low Au percentage while decreases in PEC performance was obtained at >3% Au modification. To further realize such effect with an improved understanding of the Au incorporating effects, a bulk thin film with the large area was prepared using spin-coating method to obtain an improved understanding of the Au effect mechanism. Figure 5.9 shows the photocurrent-voltage (J-V) curves of pristine and Au-incorporated hematite thin film photoanodes fabricated by the spin-coating method, under standard 1 sun illumination measured in 0.1 M NaOH. The Au-incorporated hematite thin film exhibits remarkable net PEC response with ~280% increase in photocurrent density at 0 V vs. Ag/AgCl (~1.0 V vs. RHE) with respect to the pristine hematite electrode. Such improved performance can further be improved by controlling the film thickness. Furthermore, there is an oxidation peak at around 0 V vs. Ag/AgCl under dark condition for 5 and 10% of Au, which is believed due to the oxidation of Au. Therefore, another reason for the decrease in photocurrent after 3% Au is probably due to the Au oxidation. So, the holes generated by the photocatalyst are not able to oxidize water, since oxidized gold is not a good catalyst and electronic conductor. Figure 5.10 shows the bar graph plotted at different applied potentials showing the comparison of dark and light currents for pristine and Au-incorporated hematite photocatalysts. The net photocurrent (light current – dark current) of 3% Au-hematite increases from 0.05 A cm⁻² at -0.2 V vs. Ag/AgCl to 0.08 A cm⁻² at 0 V vs. Ag/AgCl and then decreases with higher potential applied. At 0.5 V vs. Ag/AgCl, dark current is dominating for all samples. From Figure 5.10, it is

apparent that the dark current increases at increased bias and higher Au percentage, which indicates the possible oxidation of Au NPs.

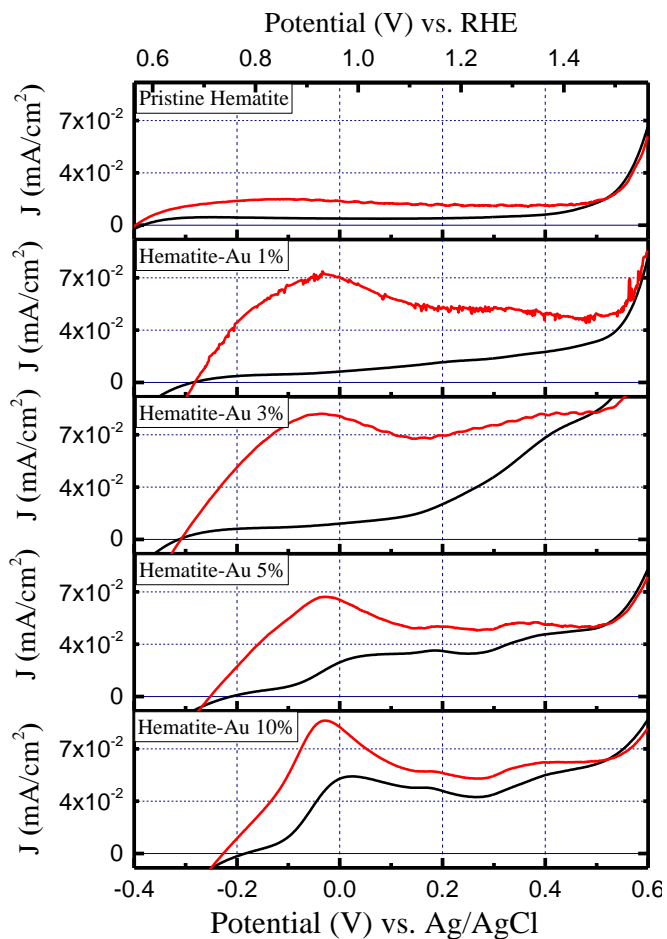


Figure 5.9: The J-V curves of pristine and 1, 3, 5, 10% Au-hematite thin film photoanodes under dark condition and 1 simulated sun light.

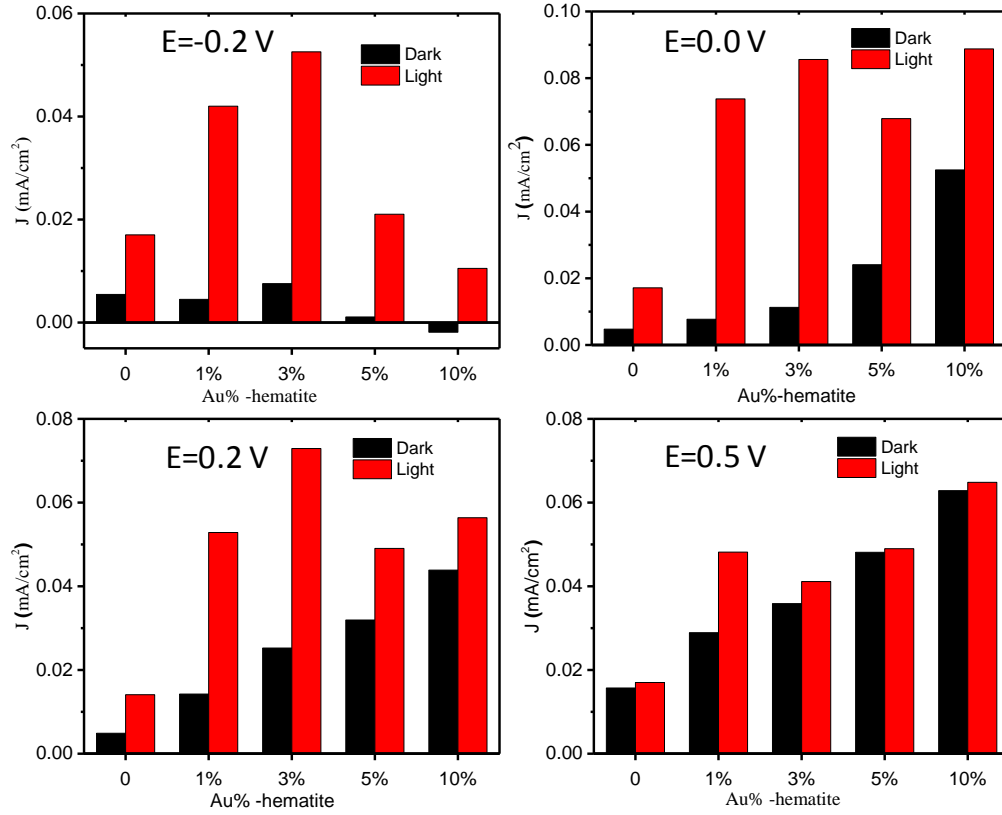


Figure 5.10: Bar graphs showing photocurrent density measured at -0.2, 0, 0.2 and 0.5 V vs. Ag/AgCl for different Au percentages.

5.4.5 Understanding the Carrier Density, Flat Band Potential, and Impedance of Au-incorporated Hematite Photoanodes

Capacitance measurements of pristine and Au-incorporated hematite thin film samples were performed and presented as Mott-Schottky (M-S) plot (Figure 5.11). The flat band potential of the semiconductor film in a liquid junction can be calculated from the Mott-Schottky equation,⁶²

$$\frac{1}{C_{SC}^2} = \frac{2}{e\epsilon_0\epsilon A^2 N_D} \left(E - E_{fb} - \frac{k_b T}{e} \right) \quad (1)$$

where C_{sc} is the space charge capacitance in $F\ cm^{-2}$; e is the electronic charge in C (1.602×10^{-19} C); ϵ is the dielectric constant of the semiconductor; ϵ_0 is the permittivity of free space ($8.854 \times$

10^{-12} Fm^{-1}); N_D is the carrier density in cm^{-3} ; E is the applied potential in V; E_{fb} is the flat band potential in V; k_b is the Boltzmann constant ($1.381 \times 10^{-23} \text{ J K}^{-1}$); and T represents the temperature in K. The temperature related term ($k_b T/e$) in eq. (1) is negligibly small (0.0257 eV) at room temperature. The flat band potential is obtained from the x-intercept of the extrapolated straight line of the M-S plot on the potential axis at $C_{\text{sc}}=0$. Table 5.3 summarizes the E_{fb} and N_D for pristine and Au-incorporated hematite under different Au percentage. The flat band potential of Au-incorporated hematite in 0.1 M NaOH solution at an AC frequency of 1 kHz increases with Au percentage and reaches $-0.751 \text{ V vs. Ag/AgCl}$, at 10% of Au, which is about 0.2 V negative compared to that of pristine hematite. The donor density estimated from the slope of the M-S plot is increased significantly after Au incorporating and reaches about 3 times at 10% Au ($1.64 \times 10^{21} \text{ cm}^{-3}$) as compared to the pristine hematite ($0.56 \times 10^{21} \text{ cm}^{-3}$). This suggests that the additional conductivity arises from Au-incorporated hematite.

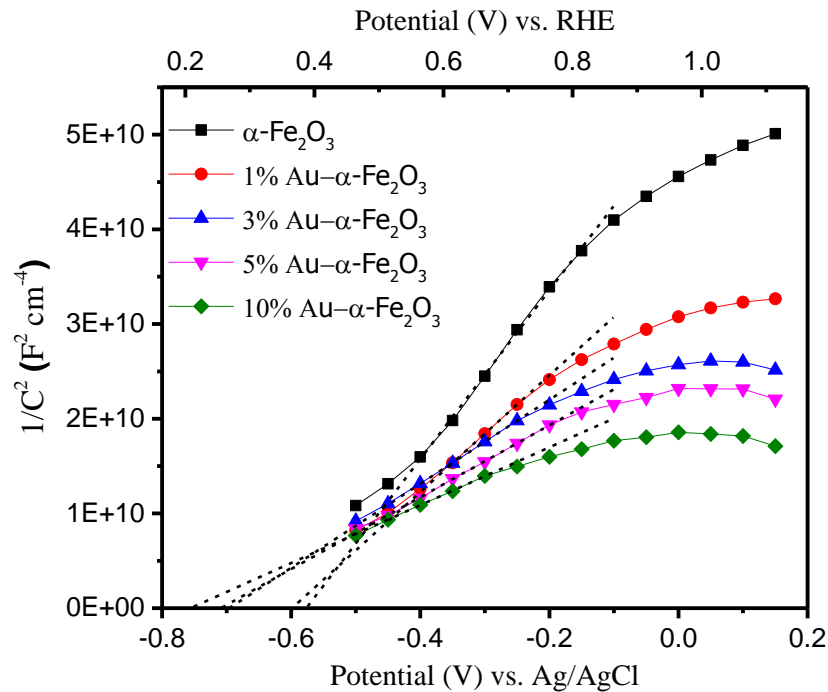


Figure 5.11: Mott-Schottky plot of pristine and Au-incorporated hematite electrodes recorded in 0.1 M NaOH electrolyte under dark condition at an AC frequency of 1 kHz.

Sample	Flat band potential $E_{fb}(V)$	Carrier density $N_D (cm^{-3})$
Pristine	-0.576	5.63×10^{20}
1% Au	-0.595	8.14×10^{20}
3% Au	-0.689	1.14×10^{21}
5% Au	-0.702	1.32×10^{21}
10% Au	-0.751	1.64×10^{21}

Table 5.3: Summary of flat band potential and charges carrier densities obtained from Mott-Schottky plot for pristine and Au-incorporated hematite thin films.

Electrochemical impedance spectroscopy (EIS) measurements were performed for pristine and Au-incorporated hematite samples under dark and standard 1 sun illumination conditions to obtain charge-transfer properties information, as shown by the Nyquist plots in Figure 5.12. An equivalent circuit, which consists of series resistance (R_S), charge transfer resistance (R_{CT}), and space charge capacitance (C_S), was used to fit the experimental EIS data.⁶³ Table 5.4 lists the EIS parameters obtained from the above fittings. The notations D and L represent dark and light condition, respectively. The resistances of the electrolyte solution from working electrode to reference electrode, which reflected as R_S , are similar for all the samples ($\sim 370\Omega$). The R_{CT} , which dictates the photocurrent response of photocatalysts, is highly dependent on the photoelectrode composition. As shown in Table 5.4, the R_{CT} values are lower under light irradiation conditions compared to the dark due to the photo-induced charge transfer. Furthermore, charge transfer resistance decreases with the increase of Au percentage, which indicates the increase of charge carriers in the film. Such phenomenon facilitates the charge transfer of holes to the donor species in the solution and suppresses the recombination of photogenerated electron-hole pairs, thus enhancing the photoactivity of hematite film for water oxidation.

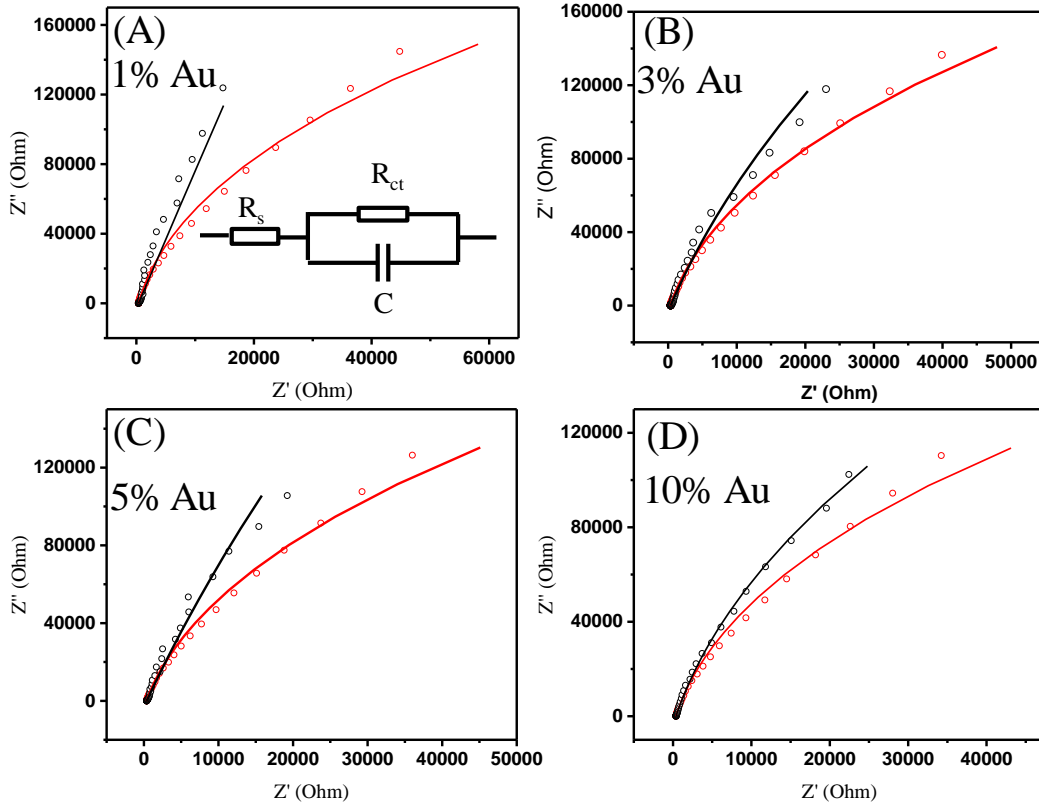


Figure 5.12: Nyquist plots of Au-incorporated hematite thin films in dark condition and standard 1 sun illumination.

Sample	R_s (Ω)	R_{CT} (Ω)	CS (μ F)
Pristine_D	370	1.0000×10^7	10
Pristine_L	377	2.4609×10^6	6.7
1%Au_D	370	2.0934×10^6	11
1%Au_L	362	6.2022×10^5	8.5
3%Au_D	370	1.4795×10^6	11
3%Au_L	362	6.2006×10^5	8.5
5%Au_D	373	4.4318×10^6	12
5%Au_L	365	5.7888×10^5	9.1
10%Au_D	378	8.6734×10^5	12
10%Au_L	374	4.5776×10^5	10

Table 5.4: Summary of experimental fit parameters from fitting Nyquist plots using the equivalent circuit shown by the inset of Figure 5.12.

5.4.6 Substrate Generation Tip Collection Mode SECM Quantification of Hematite Thin Film Photoanodes

After characterizing the photoactivity of pristine and Au-incorporated hematite samples, we correlated the photoactivity with the O₂ collection by substrate generation tip collection mode of SECM technique. A linear sweep voltammogram is presented in Figure 5.13 to illustrate the O₂ reduction current under light illumination and dark condition. During the water oxidation reaction, O₂ is generated and diffused away from the substrate. The tip potential was kept at -0.4 V vs. Ag/AgCl where O₂ can be reduced to OH⁻ in alkaline environment.⁶⁴ The reduction current at tip electrode is depended on the amount of O₂ produced from the substrate. Thus, current at Pt tip was collected as a function of both time and substrate potential. It is apparent to observe that the reduction current from Pt tip (Figure 5.13B) increases with the photocurrent (Figure 5.13A) and reaches 4.75 nA for 3% Au-incorporated hematite sample under light irradiation. In order to correlate the tip current with the amount of O₂ being collected, the tip current vs. time plot was integrated after background elimination, thus net charge transfer can be obtained. The charge transfer at Pt tip increases from 1.01 nC (dark) to 1.71 nC (light) for pristine hematite substrate. For 3% Au-incorporated hematite sample, it increases from 1.54 nC (dark) to 5.46 nC (light) under the same condition. O₂ reduction reaction is a four electron transfer process in alkaline solution,⁶⁴ so the amount of O₂ being collected by the Pt tip can be calculated. For pristine hematite, 1.58×10^9 (dark) and 2.67×10^9 (light) O₂ molecules were collected, whereas 2.40×10^9 (dark) and 8.52×10^9 (light) O₂ molecules were collected from 3% Au-incorporated hematite sample. The 3% Au-incorporated hematite exhibits ~300% enhancement in terms of O₂ collection compare to the pristine sample which agrees with the PEC measurements.

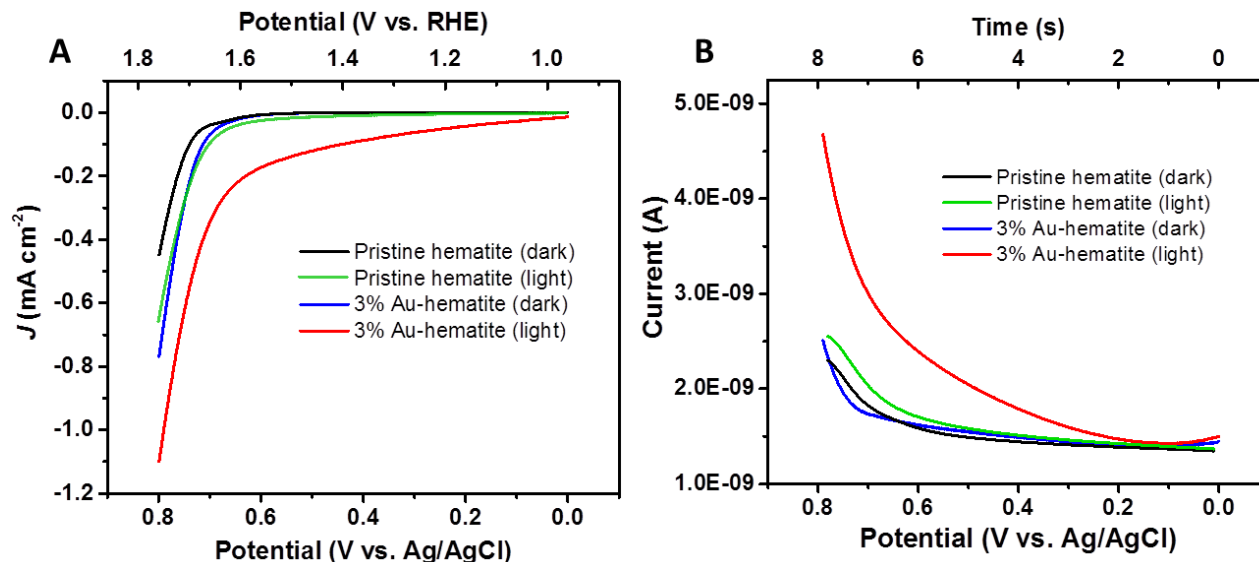


Figure 5.13: Substrate current density (A) and tip current (B) of pristine and 3% Au-incorporated hematite in 0.1 M NaOH solution under 1 sun irradiation and dark condition, respectively. Substrate potential was scanned from 0 to 0.8 V vs. Ag/AgCl at a scan rate of 0.1 V S^{-1} , while tip potential was kept at $-0.4 \text{ V vs. Ag/AgCl}$.

5.5 Conclusions

In summary, SECM technique was successfully used to efficiently screen Au-incorporated hematite photocatalyst for solar water splitting. The molar concentration of 3% Au was found to be optimum for enhancing the PEC performance of hematite thin film photocatalyst. SEM images and XPS analysis suggest that Au presents as metallic NPs and well distributed into the hematite thin film. Such 3% Au-incorporated hematite shows $\sim 280\%$ higher photocurrent improvement at 0 V vs. Ag/AgCl (1.0 V vs. RHE) with a desirable cathodic shift in the flat band potential by 200 mV . With 5% and more Au in the film, Au was oxidized at $\sim 0 \text{ V vs. Ag/AgCl}$, eventually reducing the photoactivity of the hematite film. Mott-Schottky analysis revealed that Au-incorporating contributes to the electronic conductivity of hematite film. EIS analysis obtained significant improvements on the charge transfer resistance for Au-incorporated samples. Surface generation tip collection mode of SECM quantitatively measured the generation of

oxygen with ~300% enhancement from 3% Au-incorporated hematite. Hence, the overall enhancement in water splitting performance is attributed to the electronic conductivity as a major contributing factor and improved charge separation by embedded Au NPs in the hematite. Plasmonic enhancement of Au was a minimal contribution towards improvement of water oxidation reaction, which could probably be enhanced by controlling the size of Au NPs and the hematite film thickness. More efforts will be done to improve surface plasmonic contribution for upping the photocatalytic properties of hematite.

5.6 References

1. Bornoz, P.; Abdi, F. F.; Tilley, S. D.; Dam, B.; van de Krol, R.; Graetzel, M.; Sivula, K., A Bismuth Vanadate–Cuprous Oxide Tandem Cell for Overall Solar Water Splitting. *J. Phys. Chem. C* **2014**, *118*, 16959-16966.
2. Prévot, M. S.; Sivula, K., Photoelectrochemical Tandem Cells for Solar Water Splitting. *J. Phys. Chem. C* **2013**, *117*, 17879-17893.
3. O'Regan, B.; Grätzel, M., A Low-Cost, High-Efficiency Solar Cell Based on Dye-Sensitized Colloidal TiO₂ Films. *Nature* **1991**, *353*, 737.
4. Keis, K.; Magnusson, E.; Lindström, H.; Lindquist, S.-E.; Hagfeldt, A., A 5% Efficient Photoelectrochemical Solar Cell Based on Nanostructured ZnO Electrodes. *Sol. Energy Mater. Sol. Cells* **2002**, *73*, 51-58.
5. Kongkanand, A.; Martínez Domínguez, R.; Kamat, P. V., Single Wall Carbon Nanotube Scaffolds for Photoelectrochemical Solar Cells. Capture and Transport of Photogenerated Electrons. *Nano Lett.* **2007**, *7*, 676-680.
6. Tennakone, K.; R. R. A. Kumara, G.; R. M. Kottegoda, I.; P. S. Perera, V., An Efficient Dye-Sensitized Photoelectrochemical Solar Cell Made from Oxides of Tin and Zinc. *Chem. Commun.* **1999**, 15-16.
7. Christians, J. A.; Fung, R. C.; Kamat, P. V., An Inorganic Hole Conductor for Organo-Lead Halide Perovskite Solar Cells. Improved Hole Conductivity with Copper Iodide. *J. Am. Chem. Soc.* **2013**, *136*, 758-764.
8. Kibria, M. G.; Nguyen, H. P.; Cui, K.; Zhao, S.; Liu, D.; Guo, H.; Trudeau, M. L.; Paradis, S.; Hakima, A.-R.; Mi, Z., One-Step Overall Water Splitting under Visible Light Using Multiband InGaN/GaN Nanowire Heterostructures. *ACS Nano* **2013**, *7*, 7886-7893.

9. Shan, Z.; Archana, P. S.; Shen, G.; Gupta, A.; Bakker, M. G.; Pan, S., Nanocot: Low-Cost Nanostructured Electrode Containing Carbon, Oxygen, and Titanium for Efficient Oxygen Evolution Reaction. *J. Am. Chem. Soc.* **2015**, *137*, 11996-12005.
10. Zhang, Q.; Uchaker, E.; Candelaria, S. L.; Cao, G., Nanomaterials for Energy Conversion and Storage. *Chem. Soc. Rev.* **2013**, *42*, 3127-3171.
11. Fujishima, A.; Honda, K., Electrochemical Photolysis of Water at a Semiconductor Electrode. *Nat.* **1972**, *238*, 37-38.
12. Ye, H.; Park, H. S.; Bard, A. J., Screening of Electrocatalysts for Photoelectrochemical Water Oxidation on W-Doped BiVO₄ Photocatalysts by Scanning Electrochemical Microscopy. *J. Phys. Chem. C* **2011**, *115*, 12464-12470.
13. Dozzi, M. V.; Selli, E., Doping TiO₂ with P-Block Elements: Effects on Photocatalytic Activity. *J. Photochem. Photobiol. C: Photochem. Rev.* **2013**, *14*, 13-28.
14. Maeda, K.; Takata, T.; Hara, M.; Saito, N.; Inoue, Y.; Kobayashi, H.; Domen, K., Ga:ZnO Solid Solution as a Photocatalyst for Visible-Light-Driven Overall Water Splitting. *J. Am. Chem. Soc.* **2005**, *127*, 8286-8287.
15. Zou, Z.; Ye, J.; Sayama, K.; Arakawa, H., Direct Splitting of Water under Visible Light Irradiation with an Oxide Semiconductor Photocatalyst. *Nat.* **2001**, *414*, 625-627.
16. Kurashige, W., et al., Au₂₅-Loaded Bi₄Ti₄O₁₅ Water-Splitting Photocatalyst with Enhanced Activity and Durability Produced Using New Chromium Oxide Shell Formation Method. *J. Phys. Chem. C* **2018**, *122*, 13669-13681.
17. Shinde, P. S.; Peng, X.; Wang, J.; Ma, Y.; McNamara, L. E.; Hammer, N. I.; Gupta, A.; Pan, S., Rapid Screening of Photoanode Materials Using Scanning Photoelectrochemical Microscopy Technique and Formation of Z-Scheme Solar Water Splitting System by Coupling P- and N-Type Heterojunction Photoelectrodes. *ACS Appl. Energy Mater.* **2018**, *1*, 2283-2294.
18. Barroso, M.; Pendlebury, S. R.; Cowan, A. J.; Durrant, J. R., Charge Carrier Trapping, Recombination and Transfer in Hematite (α-Fe₂O₃) Water Splitting Photoanodes. *Chem. Sci.* **2013**, *4*, 2724-2734.
19. Bora, D. K.; Braun, A.; Constable, E. C., "In Rust We Trust". Hematite – the Prospective Inorganic Backbone for Artificial Photosynthesis. *Energy Environ. Sci.* **2013**, *6*, 407-425.
20. Grätzel, M., Photoelectrochemical Cells. *Nature* **2001**, *414*, 338.
21. Sivula, K.; Le Formal, F.; Grätzel, M., Solar Water Splitting: Progress Using Hematite (α-Fe₂O₃) Photoelectrodes. *ChemSusChem* **2011**, *4*, 432-449.
22. Young, K. M. H.; Klahr, B. M.; Zandi, O.; Hamann, T. W., Photocatalytic Water Oxidation with Hematite Electrodes. *Catal. Sci. Technol.* **2013**, *3*, 1660-1671.

23. Ahn, H.-J.; Yoon, K.-Y.; Kwak, M.-J.; Jang, J.-H., A Titanium-Doped SiO_x Passivation Layer for Greatly Enhanced Performance of a Hematite-Based Photoelectrochemical System. *Angew. Chem. Int. Ed.* **2016**, *55*, 9922-9926.
24. Le Formal, F.; T éreault, N.; Cornuz, M.; Moehl, T.; Gr äzel, M.; Sivula, K., Passivating Surface States on Water Splitting Hematite Photoanodes with Alumina Overlayers. *Chem. Sci.* **2011**, *2*, 737-743.
25. Xi, L.; Bassi, P. S.; Chiam, S. Y.; Mak, W. F.; Tran, P. D.; Barber, J.; Chye Loo, J. S.; Wong, L. H., Surface Treatment of Hematite Photoanodes with Zinc Acetate for Water Oxidation. *Nanoscale* **2012**, *4*, 4430-4433.
26. Yang, X.; Liu, R.; Du, C.; Dai, P.; Zheng, Z.; Wang, D., Improving Hematite-Based Photoelectrochemical Water Splitting with Ultrathin TiO₂ by Atomic Layer Deposition. *ACS Appl. Mater. Interfaces* **2014**, *6*, 12005-12011.
27. Carneiro, L. M.; Cushing, S. K.; Liu, C.; Su, Y.; Yang, P.; Alivisatos, A. P.; Leone, S. R., Excitation-Wavelength-Dependent Small Polaron Trapping of Photoexcited Carriers in α -Fe₂O₃. *Nat. Mater.* **2017**, *16*, 819.
28. Li, C.; Li, A.; Luo, Z.; Zhang, J.; Chang, X.; Huang, Z.; Wang, T.; Gong, J., Surviving High-Temperature Calcination: ZrO₂-Induced Hematite Nanotubes for Photoelectrochemical Water Oxidation. *Angew. Chem. Int. Ed.* **2017**, *56*, 4150-4155.
29. Yoon, K.-Y.; Ahn, H.-J.; Kwak, M.-J.; Kim, S.-I.; Park, J.; Jang, J.-H., A Selectively Decorated Ti-FeOOH Co-Catalyst for a Highly Efficient Porous Hematite-Based Water Splitting System. *J. Mater. Chem. A* **2016**, *4*, 18730-18736.
30. Zhang, Z.; Gao, C.; Li, Y.; Han, W.; Fu, W.; He, Y.; Xie, E., Enhanced Charge Separation and Transfer through Fe₂O₃/ITO Nanowire Arrays Wrapped with Reduced Graphene Oxide for Water-Splitting. *Nano Energy* **2016**, *30*, 892-899.
31. Li, C.; Wang, T.; Luo, Z.; Liu, S.; Gong, J., Enhanced Charge Separation through Ald-Modified Fe₂O₃/Fe₂TiO₅ Nanorod Heterojunction for Photoelectrochemical Water Oxidation. *Small* **2016**, *12*, 3415-3422.
32. Mayer, M. T.; Du, C.; Wang, D., Hematite/Si Nanowire Dual-Absorber System for Photoelectrochemical Water Splitting at Low Applied Potentials. *J. Am. Chem. Soc.* **2012**, *134*, 12406-12409.
33. Kim, J. H.; Jang, J.-W.; Jo, Y. H.; Abdi, F. F.; Lee, Y. H.; van de Krol, R.; Lee, J. S., Hetero-Type Dual Photoanodes for Unbiased Solar Water Splitting with Extended Light Harvesting. *Nat. Commun.* **2016**, *7*, 13380.
34. Malviya, K. D.; Dotan, H.; Shlenkevich, D.; Tsyganok, A.; Mor, H.; Rothschild, A., Systematic Comparison of Different Dopants in Thin Film Hematite (α -Fe₂O₃) Photoanodes for Solar Water Splitting. *J. Mater. Chem. A* **2016**, *4*, 3091-3099.

35. Zhang, X.; Klaver, P.; van Santen, R.; van de Sanden, M. C. M.; Bieberle-Hütter, A., Oxygen Evolution at Hematite Surfaces: The Impact of Structure and Oxygen Vacancies on Lowering the Overpotential. *J. Phys. Chem. C* **2016**, *120*, 18201-18208.
36. Zhang, Y.; Jiang, S.; Song, W.; Zhou, P.; Ji, H.; Ma, W.; Hao, W.; Chen, C.; Zhao, J., Nonmetal P-Doped Hematite Photoanode with Enhanced Electron Mobility and High Water Oxidation Activity. *Energy Environ. Sci.* **2015**, *8*, 1231-1236.
37. Zhu, C.; Li, C.; Zheng, M.; Delaunay, J.-J., Plasma-Induced Oxygen Vacancies in Ultrathin Hematite Nanoflakes Promoting Photoelectrochemical Water Oxidation. *ACS Appl. Mater. Interfaces* **2015**, *7*, 22355-22363.
38. Li, C.; Luo, Z.; Wang, T.; Gong, J., Surface, Bulk, and Interface: Rational Design of Hematite Architecture toward Efficient Photo-Electrochemical Water Splitting. *Adv. Mater.* **2018**, *30*, 1707502.
39. Shinde, P. S.; Lee, S. Y.; Ryu, J.; Choi, S. H.; Jang, J. S., Enhanced Photoelectrochemical Performance of Internally Porous Au-Embedded α -Fe₂O₃ Photoanodes for Water Oxidation. *Chem. Commun.* **2017**, *53*, 4278-4281.
40. Zhang, X.; Li, H.; Wang, S.; Fan, F.-R. F.; Bard, A. J., Improvement of Hematite as Photocatalyst by Doping with Tantalum. *J. Phys. Chem. C* **2014**, *118*, 16842-16850.
41. Archana, P. S.; Pachauri, N.; Shan, Z.; Pan, S.; Gupta, A., Plasmonic Enhancement of Photoactivity by Gold Nanoparticles Embedded in Hematite Films. *J. Phys. Chem. C* **2015**, *119*, 15506-15516.
42. Wang, J.; Pan, S.; Chen, M.; Dixon, D. A., Gold Nanorod-Enhanced Light Absorption and Photoelectrochemical Performance of α -Fe₂O₃ Thin-Film Electrode for Solar Water Splitting. *J. Phys. Chem. C* **2013**, *117*, 22060-22068.
43. Bard, A. J.; Fan, F. R. F.; Kwak, J.; Lev, O., Scanning Electrochemical Microscopy. Introduction and Principles. *Anal. Chem.* **1989**, *61*, 132-138.
44. Lee, J.; Ye, H.; Pan, S.; Bard, A. J., Screening of Photocatalysts by Scanning Electrochemical Microscopy. *Anal. Chem.* **2008**, *80*, 7445-7450.
45. Jang, J. S.; Yoon, K. Y.; Xiao, X.; Fan, F.-R. F.; Bard, A. J., Development of a Potential Fe₂O₃-Based Photocatalyst Thin Film for Water Oxidation by Scanning Electrochemical Microscopy: Effects of Ag-Fe₂O₃ Nanocomposite and Sn Doping. *Chem. Mater.* **2009**, *21*, 4803-4810.
46. Conzuelo, F.; Sliozberg, K.; Gutkowski, R.; Grützke, S.; Nebel, M.; Schuhmann, W., High-Resolution Analysis of Photoanodes for Water Splitting by Means of Scanning Photoelectrochemical Microscopy. *Anal. Chem.* **2017**, *89*, 1222-1228.

47. Li, J.; Cushing, S. K.; Zheng, P.; Meng, F.; Chu, D.; Wu, N., Plasmon-Induced Photonic and Energy-Transfer Enhancement of Solar Water Splitting by a Hematite Nanorod Array. *Nat. Commun.* **2013**, *4*, 2651.
48. Kay, A.; Scherrer, B.; Piekner, Y.; Malviya, K. D.; Grave, D. A.; Dotan, H.; Rothschild, A., Film Flip and Transfer Process to Enhance Light Harvesting in Ultrathin Absorber Films on Specular Back-Reflectors. *Adv. Mater.* **2018**, *30*, 1802781.
49. Chen, B.; Fan, W.; Mao, B.; Shen, H.; Shi, W., Enhanced Photoelectrochemical Water Oxidation Performance of a Hematite Photoanode by Decorating with Au–Pt Core–Shell Nanoparticles. *Dalton Trans.* **2017**, *46*, 16050-16057.
50. Wang, L.; Hu, H.; Nguyen, N. T.; Zhang, Y.; Schmuki, P.; Bi, Y., Plasmon-Induced Hole-Depletion Layer on Hematite Nanoflake Photoanodes for Highly Efficient Solar Water Splitting. *Nano Energy* **2017**, *35*, 171-178.
51. Gross Koren, M.; Dotan, H.; Rothschild, A., Nano Gold Rush: On the Origin of the Photocurrent Enhancement in Hematite Photoanodes Decorated with Gold Nanoparticles. *J. Phys. Chem. C* **2016**, *120*, 15042-15051.
52. Li, J.; Cushing, S. K.; Chu, D.; Zheng, P.; Bright, J.; Castle, C.; Manivannan, A.; Wu, N., Distinguishing Surface Effects of Gold Nanoparticles from Plasmonic Effect on Photoelectrochemical Water Splitting by Hematite. *J. Mater. Res.* **2016**, *31*, 1608-1615.
53. Wang, L.; Zhou, X.; Nguyen, N. T.; Schmuki, P., Plasmon-Enhanced Photoelectrochemical Water Splitting Using Au Nanoparticles Decorated on Hematite Nanoflake Arrays. *ChemSusChem* **2015**, *8*, 618-622.
54. Li, C.; Wang, P.; Li, H.; Wang, M.; Zhang, J.; Qi, G.; Jin, Y., Plasmon-Driven Water Splitting Enhancement on Plasmonic Metal–Insulator–Semiconductor Hetero-Nanostructures: Unraveling the Crucial Role of Interfacial Engineering. *Nanoscale* **2018**, *10*, 14290-14297.
55. Verma, A.; Srivastav, A.; Banerjee, A.; Sharma, D.; Sharma, S.; Singh, U. B.; Satsangi, V. R.; Shrivastav, R.; Avasthi, D. K.; Dass, S., Plasmonic Layer Enhanced Photoelectrochemical Response of Fe₂O₃ Photoanodes. *J. Power Sources* **2016**, *315*, 152-160.
56. Xu, Z., et al., Interface Manipulation to Improve Plasmon-Coupled Photoelectrochemical Water Splitting on A-Fe₂O₃ Photoanodes. *ChemSusChem* **2017**, *11*, 237-244.
57. Eftekharinia, B.; Moshaii, A.; Sobhkhiz Vayghan, N.; Dabirian, A., Efficient Nanoporous Hematite Photoanodes Prepared by Electron Beam Evaporation and Au Modification. *ChemCatChem* **2018**, *10*, 4665-4675.
58. Kant, R.; Pathak, S.; Dutta, V., Design and Fabrication of Sandwich-Structured A-Fe₂O₃/Au/ZnO Photoanode for Photoelectrochemical Water Splitting. *Sol. Energy Mater. Sol. Cells* **2018**, *178*, 38-45.

59. Dunn, H. K.; Feckl, J. M.; Müller, A.; Fattakhova-Rohlfing, D.; Morehead, S. G.; Roos, J.; Peter, L. M.; Scheu, C.; Bein, T., Tin Doping Speeds up Hole Transfer During Light-Driven Water Oxidation at Hematite Photoanodes. *Phys. Chem. Chem. Phys.* **2014**, *16*, 24610-24620.
60. Ling, Y.; Wang, G.; Wheeler, D. A.; Zhang, J. Z.; Li, Y., Sn-Doped Hematite Nanostructures for Photoelectrochemical Water Splitting. *Nano Lett.* **2011**, *11*, 2119-2125.
61. Shinde, P. S.; Choi, S. H.; Kim, Y.; Ryu, J.; Jang, J. S., Onset Potential Behavior in A-Fe₂O₃ Photoanodes: The Influence of Surface and Diffusion Sn Doping on the Surface States. *Phys. Chem. Chem. Phys.* **2016**, *18*, 2495-2509.
62. Bard, A. J.; Faulkner, L. R.; Leddy, J.; Zoski, C. G., *Electrochemical Methods: Fundamentals and Applications*; Wiley New York, 1980; Vol. 2.
63. Shan, Z.; Clayton, D.; Pan, S.; Archana, P. S.; Gupta, A., Visible Light Driven Photoelectrochemical Properties of Ti@TiO₂ Nanowire Electrodes Sensitized with Core-Shell Ag@Ag₂S Nanoparticles. *J. Phys. Chem. B* **2014**, *118*, 14037-14046.
64. Song, C.; Zhang, J., Electrocatalytic Oxygen Reduction Reaction. In *Pem Fuel Cell Electrocatalysts and Catalyst Layers: Fundamentals and Applications*, Zhang, J., Ed. Springer London: London, 2008; pp 89-134.

CHAPTER 6

CONCLUSIONS AND PERSPECTIVES

The plasmonic Au NPs have been successfully applied to two major aspects: 1) light scattering spectroelectrochemistry detection of catalyzed redox reactions on transparent electrodes comprised of plasmonic nanoparticles; and 2) an improved understanding of the optical and electronic effects of plasmonic nanoparticles on photoelectrochemical reaction at a metal oxide photoanode for solar water splitting. The light scattering spectroelectrochemistry methodology has been applied to hydrazine oxidation, methanol oxidation and formic acid oxidation reactions at plasmonic surfaces. Au anodization, double layer charging effect, surface adsorbates and surface coating layer have been successfully resolved by the developed method and experimental design. Furthermore, Au has been successfully incorporated with hematite thin film photoanode for enhanced solar water splitting. The optical and electronic effects on the enhancement have been quantitatively revealed.

Dark-field scattering has been combined with electrochemical methods as well as ultramicroelectrode fabrication in Chapter 3 to study the kinetics of electrocatalytic oxidation of hydrazine at Au NPs in real time. At low overpotential region, double-layer charging and surface adsorption of N_2H_3 contributes to a decrease in DFS intensity of single Au NPs while hydrazine is being oxidized. A significant decrease in the DFS signal of Au NPs in the high overpotential region can be obtained in the absence of hydrazine because of Au oxidation. This Au oxidation process is reversible based on the DFS intensity. Such Au oxidation is weakened with the presence of hydrazine in the solution and can be completely eliminated with >50 mM of

hydrazine. At high overpotential and low scan rates, N₂ bubbles generation takes place to deactivate the Au NPs accompanied with a decrease in oxidation current and spike shaped increase in light scattering by the gas bubbles. ITO UME has the capability to correlate NPs sizes to DFS responses which further confirms the bulk study. The ITO UME combined with DFS spectroelectrochemistry methodology provides a better understanding of catalytic reactions and could be potentially used for biological sensing.¹⁻² Since Au is able to bind with various kinds of aptamers for biomolecules, the Au modified UME could recognize and bind with proteins and DNAs at single molecule level.³⁻⁵ The electronic and local optical responses will vary when the binding event occurs, thus interaction between biomolecules could be monitored. Different laser sources can be applied to the Au modified ITO UME system for chemical and biological sensing applications. For example, 405 nm GaN laser is able to cause fluorescence in some chemical and biological molecules. Moreover, the 405 nm laser has the ability to kill various kinds of bacteria.⁶ With the help of Au NPs and UME, single particle/molecule fluorescence can be achieved and the bactericidal mechanism can be studied. Au NPs with diameter around 50 nm strongly absorbs and scatters around 532 nm based on Mie theory simulation, so laser with wavelength at 532 nm can be used to study the light absorption and scattering effect on smaller Au NPs with high sensitivity. In terms of Raman spectroscopy, 532-nm excitation can cause sample fluorescence, which may swamp the faint Raman signal. Therefore, the use of a near infrared excitation source can eliminate the fluorescence from most molecules. The 785 nm laser has been found to be optimum for these applications, as it avoids fluorescence but still returns a Raman signal sufficient to be detected with a reasonable signal-to-noise ratio.

In order to extend above spectroelectrochemistry study to other redox reactions relevant to energy transformation such as fuel cell based reactions, in Chapter 4, Au-ITO NPs electrode is

further modified by Pt to form Au@Pt and Au-Pt core-shell structures using electrochemical deposition method for methanol and formic acid oxidation reaction. The reported controlled electrodeposition sample preparation technique is simple and highly reproducible. The Au-Pt core-shell structure is confirmed by SEM, HRTEM and EDS mapping. The Au@Pt NPs display desirable electrocatalytic activity for both methanol and formic acid oxidation. Au oxidation becomes weaker and is terminated with increasing Pt thicknesses. The electrochemical oxidation of formic acid showed that higher coverage of surface-bound Pt NPs prefers the direct oxidation pathway while lower Pt coverage produced the CO_{ads} intermediate species, which eventually poisoned the electrode surface.

One drawback of the electrochemical deposition technique is that it is extremely hard to control the surface morphology and reproducibility precisely. Although the multistep potential technique allows us to narrow the particle size distribution to a low level, the shape of the particle is still estimated. The perspective of the electrochemical detection and imaging project would focus on how to fabricate small electrodes with well-defined sizes and shapes with high reproducibility. Electron beam lithography is an ideal solution for making highly reproducible and well-defined structures⁷, for example Au disc nanoarrays. The Au disc nanoarrays would be much more sensitive to the surface redox reactions than Au NPs prepared by electrodeposition. Furthermore, the diffusion profile at a nanodisc is much simpler than that on a nanoparticle; this is because the surface of a nanoparticle is not fully in contact with the electrolyte. The surface area needs to be estimated when performing digital simulation for the nanoparticle structures. In contrast, the surface area and diffusion behavior are more straightforward to be calculated for the nanodisc structures.

Chapter 5 describes the role of plasmonic Au NPs in photoactive materials. Au is doped into hematite thin film materials for solar water splitting. SPECM is used to determine that 3% of Au doping is the optimum condition for enhancing the PEC performance of hematite thin film photocatalyst. This is the first study on Au-doped hematite by SPECM technique. SEM and EDS analysis show that Au NPs are well distributed into the hematite film. The 3% Au-doped hematite shows ~280% higher photocurrent improvement at 0 V vs. Ag/AgCl (1.0 V vs. RHE) with a desirable cathodic shift in the flat band potential by 200 mV. With more than 5% of Au doping, Au oxidation takes places at ~0 V vs. Ag/AgCl, which contributes highly to the dark current and reduces the photoactivity of the hematite film. Mott-Schottky analysis reveals that Au-doping contributes to the electronic conductivity of hematite film. EIS analysis obtains significant improvements on the charge transfer resistance for Au-doped samples. Plasmonic enhancement of Au NPs has minimal effect on the improvement of photoactivity, which could probably be enhanced by controlling the size of Au NPs and the hematite film thickness.

The future work of the plasmonic enhancement of photoactive materials project lies in controlling the sizes and positions of Au NPs in hematite thin films. The size of the particles could be controlled by using pre-synthesized Au NPs. The position of plasmonic NPs in hematite films is an important aspect on the photoactivity. It is reported that bottom layer of Au could reflect light back into hematite film which further improves the light absorption of the material, thus enhances the photoactivity.⁸ Au nanostructure modification by nanolithography on top of hematite film is also found to improve the photocurrent of solar water splitting.⁹ The positions of the Au nanostructures could be adjusted to bottom, middle and top of the hematite film to further optimize incorporating conditions. It is achievable to combine the nanofabrication technique described in Chapter 3 with the PEC measurements in Chapter 5 for a better hematite film

modification. Moreover, the efficient SPECM technique could be utilized to investigate more low-cost, transition metal doping materials such as Ti, Co, Ni and Nb for hematite photocatalyst. The Pan group has successfully developed sample arrays of Co and Nb doped hematite for SPECM study. Such experiments are in progress.

References

1. Alligrant, T. M.; Dasari, R.; Stevenson, K. J.; Crooks, R. M., Electrocatalytic Amplification of Single Nanoparticle Collisions Using DNA-Modified Surfaces. *Langmuir* **2015**, *31*, 11724-11733.
2. Saha, K.; Agasti, S. S.; Kim, C.; Li, X.; Rotello, V. M., Gold Nanoparticles in Chemical and Biological Sensing. *Chem. Rev.* **2012**, *112*, 2739-2779.
3. Fixe, F.; Branz, H. M.; Louro, N.; Chu, V.; Prazeres, D. M.; Conde, J. P., Immobilization and Hybridization by Single Sub-Millisecond Electric Field Pulses, for Pixel-Addressed DNA Microarrays. *Biosensors & bioelectronics* **2004**, *19*, 1591-1597.
4. Fixe, F.; Branz, H. M.; Louro, N.; Chu, V.; Prazeres, D. M. F.; Conde, J. P., Electric-Field Assisted Immobilization and Hybridization of DNA Oligomers on Thin-Film Microchips. *Nanotechnology* **2005**, *16*, 2061.
5. Aćimović, S. S.; Kreuzer, M. P.; González, M. U.; Quidant, R., Plasmon near-Field Coupling in Metal Dimers as a Step toward Single-Molecule Sensing. *ACS Nano* **2009**, *3*, 1231-1237.
6. Guffey, J. S.; Wilborn, J., In Vitro Bactericidal Effects of 405-Nm and 470-Nm Blue Light. *Photomed. Laser Surg.* **2006**, *24*, 684-688.
7. Constancias, C.; Landis, S.; Manakli, S.; Martin, L.; Pain, L.; Rio, D., Electron Beam Lithography. In *Lithography*, S. Landis: 2013.
8. Archana, P. S.; Pachauri, N.; Shan, Z.; Pan, S.; Gupta, A., Plasmonic Enhancement of Photoactivity by Gold Nanoparticles Embedded in Hematite Films. *J. Phys. Chem. C* **2015**, *119*, 15506-15516.
9. Iandolo, B.; Zäch, M., Enhanced Water Splitting on Thin-Film Hematite Photoanodes Functionalized with Lithographically Fabricated Au Nanoparticles. *Aust. J. Chem.* **2012**, *65*, 633-637.